Laser Doppler Anemometry and Acoustic Measurements of an S822 Airfoil at Low Reynolds Numbers

by

Stephen M. Orlando

A thesis
presented to the University of Waterloo
in fulfillment of the
thesis requirement for the degree of
Master of Applied Science
in
Mechanical Engineering

Waterloo, Ontario, Canada, 2011

Abstract

Experimental aeroacoustic research was conducted on a wind turbine specific airfoil at low Reynolds numbers. The goal of this thesis was to study trailing edge noise generation from the airfoil and investigate correlations between the noise and the flow field. Before experiments were performed the current wind tunnel had to be modified in order to make it more suitable for aeroacoustic tests. Sound absorbing foam was added to the inside of the tunnel to lower the background noise levels and turbulence reduction screens were added which lowered the turbulence. An S822 airfoil was chosen because it is designed for low Reynolds flows attainable in the wind tunnel which are on the order of 10^4.

Smoke wire flow visualization was used to gain insight into the airfoil wake development and oil film flow visualization was used to qualitatively assess the boundary layer development. Laser Doppler anemometry (LDA) was used to measure two components of velocity at high data rates in the airfoil wake. Wake profiles were measured in addition to single point measurements to determine the velocity spectrum. A microphone was mounted inside the test section in order to measure the trailing edge noise. Initial plans included measuring the trailing edge noise with a microphone array capable of quantifying and locating noise sources. Although an array was built and beamforming code was written it was only used in preliminary monopole source tests.

Oil film results showed the behaviour of the boundary layer to be consistent with previous low Reynolds number experiments. LDA results revealed sharp peaks in the velocity spectra at 1100 Hz from $U_0 = 15$–24 m/s, and 3100 and 3800 Hz, from $U_0 = 25$–35 m/s, which were inconsistent with vortex shedding results of previous researchers. Also present were a series of broad peaks in the spectra that increase from 1200–1700 Hz in the $U_0 = 25$–35 m/s range. The shedding frequency from the smoke wire flow visualization was calculated to be 1250 Hz at $U_0 = 26$ m/s. These sharp peaks were also present in the acoustic spectrum. It was reasoned that these peaks are due to wind tunnel resonance which is a common occurrence in hard wall wind tunnels. In particular the tone at 1100 Hz is due to a standing wave with a wavelength equal to half the tunnel width. The shedding frequency from the smoke wire flow visualization was calculated to be 1100 Hz at $U_0 = 20$ m/s. These tones exhibited a "ladder-like" relationship with freestream velocity, another aspect indicative of wind tunnel resonance. It was reasoned that the wind tunnel resonance was forcing the shedding frequency of the airfoil in the $U_0 = 15$–24 m/s range, and in the $U_0 = 25$–35 m/s range, the shedding frequency corresponded to the broad peaks in the LDA spectra.

Acknowledgments

Many people have aided me throughout my master's degree and without their help this would have been possible. I would like to thank the following people who helped me get to where I am today.

Firstly I would like to thank Professor David Johnson, who provided technical guidance throughout my master's degree. Under his supervision I was given the freedom to undertake a completely independent research project. I had the opportunity to participate in many unique research projects and industry projects that gave me a very good practical understanding of the wind industry. Finally I would like to thank him for sending me to CanWEA twice and to Berlin.

To the staff at the University of Waterloo who provided much technical advice. Professor Serhiy Yarusevych who assisted in interpreting results, John Potzold and Kwai Chan in the student shop who taught me everything I know about metal fabrication, Andy Barber and Jim Merli who provided assistance with the many electrical projects, and Gord Hitchman who assisted me with the LDA system.

I would like to thank my fellow graduates, Drew Gertz, Brian Gaunt, Erik Skensved, Vivian Lam, Mike Bishop, Ryan Gerakopulos, Chris Morton, and Michael Boutillier, who were always ready to help me throughout my master's degree. A special thanks to Adam Bale and Adam McPhee who I worked with on several projects and taught me a great deal about electronics and acoustics. Attending the conference in Berlin would not have been possible without these two.

To my two good friends John Crowley and Dustin Wall who provided motivation as they were also doing graduate work. To my friends in Waterloo, Mike Pieterse, Guy Porlier, and Neil Cavan who made my life outside of school during my master's enjoyable.

Finally I would like to thank my parents Al and Diane Orlando, and my sister Christine Orlando. They have always supported me in everything that I have done and I cannot thank them enough.

Dedication

This work is dedicated to my parents Al and Diane Orlando.

Table of Contents

List of Tables

List of Figures

Nomenclature

Roman Symbols

A_{gain}	Array gain [dB]
b_w	Beamwidth [m]
C	Test section area [mm^2]
c	Airfoil chord length [mm]
c_0	Speed of sound [m/s]
c_d	Airfoil section drag coefficient [-]
c_{du}	Uncorrected drag coefficient [-]
C_f	Skin friction coefficient [-]
c_l	Airfoil section lift coefficient [-]
D	Airfoil section drag force [N/m]
d	Projected frontal area of airfoil [mm]
D_a	Array aperture [m]
D_h	High frequency directivity function [-]
d_p	Particle diameter [μm]
d^*	Separation between the two peaks in the freestream velocity RMS wake profile [mm]
d_{wire}	Diameter of smoke wire [mm]
dx	First short axis dimension of measurement volume [mm]
dy	Second short axis dimension of measurement volume [mm]

dz	Long axis dimension of measurement volume [mm]
$\hat{e}$	Steering vector [-]
E_v	Energy of transverse velocity component [(m^2/s^2)/Hz]
f	Frequency [Hz]
f_0	LDA frequency shift [Hz]
f_c	Center frequency [Hz]
f_{camera}	Camera frame rate [fps]
f_D	Doppler frequency [Hz]
Δf	Frequency bandwidth [Hz]
f_l	Lower frequency in band [Hz]
f_r	Resonant frequency [Hz]
f_{r,β_P}	Beta mode resonant frequency [Hz]
f_s	Shedding frequency [Hz]
f_u	Upper frequency in band [Hz]
$f_{VFD,h}$	High speed VFD setting [Hz]
$f_{VFD,l}$	Low speed VFD setting [Hz]
$\hat{G}$	Cross-spectral matrix [Pa^2]
$\hat{G}_{diag=0}$	Cross-spectral matrix with autocorrelation terms equal to zero [Pa^2]
h	Test section height [mm]
I	Turbulence intensity [-]
K_1	Constant used to calculate solid blockage correction factor [-]
L	Airfoil section lift force [N/m]
l	Generic length scale [m]
L_p	Sound pressure level [dB]

m_0	Number of microphones
M_c	Convection Mach number
N	Number of FFT blocks
N_{band}	Number of narrowband levels in the proportional band
p_{band}	Pressure level for a proportional band [Pa]
p_i	Narrowband pressure level [Pa]
P_{ik}, P_{jk}	Single-sided complex pressure spectrum for microphone pairs [i,j] for block k [Pa]
p_k	Pressure signal from k$^{\mathrm{th}}$ microphone [Pa]
p_{ref}	Reference pressure [Pa]
p_{rms}	Root mean square of the pressure [Pa]
r	Array-to-source distance [m]
$r_{1 \ldots m_0}$	Distances between the microphones and the scanning point [m]
r_c	Distance between the array center and the scanning point [m]
Re_c	Reynolds number based on chord length [-]
$Re_{d_{wire}}$	Reynolds number based on smoke wire diameter [-]
r_k	Distance from k$^{\mathrm{th}}$ microphone to scan point [m]
St	Strouhal number [-]
St_{d*}	Strouhal number based on d* [-]
s_v	Vortex separation [mm]
t	Time [s]
t_a	Airfoil thickness [mm]
T_b	Number of data points in the acoustic signal
Δt	Sampling interval in the time signal [s]
U_0	Mean freestream velocity [m/s]

U_{blue}	Velocity component from blue laser beams [m/s]
u_{fringe}	Fringe velocity [m/s]
U_{green}	Velocity component from green laser beams [m/s]
$u_{\perp}$	Particle velocity component perpendicular to the fringes [m/s]
U_x	Velocity component in x-direction [m/s]
U_y	Velocity component in y-direction [m/s]
w_s	Windowing constant [-]
Δx_v	Average vortex movement distance between image frames [mm]
Y	Beamforming output [Pa^2]
$y(t)$	Reconstructed source signal [Pa]

Abbreviations

AWEA	American Wind Energy Association
BTE	Blunt Trailing Edge
CanWEA	Canadian Wind Energy Association
CNC	Computer Numerically Controlled
CSM	Cross-Spectral Matrix
FFT	Fast Fourier Transform
HAWT	Horizontal Axis Wind Turbine
LBL	Laminar Boundary Layer
LDA	Laser Doppler Anemometry
LDV	Laser Doppler Velocimetry
NREL	National Renewable Energy Laboratory
PIV	Particle Image Velocimetry
RMS	Root-Mean-Square

RSS	Root-sum-square
SIROCCO	SIlent ROtors by aCoustiC Optimization
TBL	Turbulent Boundary Layer
TE	Trailing Edge
VFD	Variable Frequency Drive
VTSWT	Virgina Tech Stability Wind Tunnel

Greek Symbols

α	Angle of attack [°]
α_{eff}	Effective angle of attack for open jet wind tunnels [°]
α_P	Parker alpha resonant mode
β_P	Parker beta resonant mode
γ_P	Parker gamma resonant mode
δ_f	Fringe spacing [mm]
δ_P	Parker delta resonant mode
ε_{sb}	Solid blockage correction factor [-]
ε_{wb}	Wake blockage correction factor [-]
θ	Intersection angle between LDA beams [°]
λ_b	Laser wavelength [nm]
λ_{β_P}	Standing wave wavelength of β_P mode resonance [m]
λ_r	Resonant standing wave wavelength [m]
μ	Dynamic viscosity [Pa·s]
ρ	Fluid density [kg/m^3]
σ	Standard deviation of freestream velocity component [m/s]
$\tau_{1 \ldots m_0}$	Sound propagation times from the scanning point to each microphone [s]

ϕ	Angular position around the trailing edge
Ω	Reference resonant angular frequency [rad/s]
ω	Resonant angular frequency [rad/s]

Mathematical Symbols

$\dagger$	Complex conjugate transpose
$*$	Complex conjugate

Chapter 1

Introduction

1.1 Problem Statement and Goals

With the ever increasing cost of energy from fossil fuels and growing concerns about climate change, methods to capture renewable energy are becoming more and more prevalent as well as financially viable. In particular the prevalence of wind turbines has grown significantly in recent years. However wind turbines are not without financial and operational problems that hinder their widespread use. They are only financially feasible in geographic locations with consistently high wind speeds and in close proximity to existing electricity distribution infrastructure. There is a certain amount of risk involved in financing a wind farm due to the variability of the wind which leads to an uncertainty in the estimate of power production. In recent years, broken gearboxes have become an operational problem due to the fluctuating loads caused by the wind's inconsistency. Another operational problem of wind turbines is their noise output. Wind turbine noise is problematic because it can be intrusive to people that are nearby. Any residence, place of work, road, park, or similar place is known as a "receptor". Many governments around the world have specified wind turbine noise setback limits which are minimum distances between receptors and wind turbines at which noise levels must be below a certain level [1, 2]. Noise levels at these receptors are predicted before the wind turbines are installed using complex calculations involving many variables such as wind direction, wind speed, wind shear, vegetation, temperature, and humidity. Sometimes the calculations can be incorrect and the actual noise at a receptor is not below the required limit. When this happens, the residents can be compensated financially or a curtailment program is applied to limit the wind turbine noise. In some cases residents have complained of health problems associated with wind turbine noise including infrasound which is very low frequency noise. A medical and engineering study funded by the American Wind Energy Association (AWEA) and the Canadian Wind Energy Association (CanWEA) [3] found that wind turbine noise (including infrasound) does not pose a risk to humans at reasonable setback distances. At the date of this thesis, there have not been any conclusive medical studies suggesting that humans can be harmed from wind turbine noise. However there have been numerous case studies suggesting otherwise as documented by Colby et al. [3]. Some have found that by properly informing the public about wind turbine noise and implementing a strong public relations campaign, many complaints can be avoided [1]. The root cause of this problem is however the turbines themselves. Many researchers and wind turbine companies are studying wind turbine noise and methods of noise reduction. The adverse effects of wind turbine noise (whether perceived or real) are the motivation for this thesis.

Although many types of wind turbines exist, this thesis is only concerned with three-blade horizontal axis wind turbines (HAWTs). Further mention of wind turbines will refer exclusively to HAWTs. For residential use, wind turbine rotors can be as small as 1 m in diameter whereas wind turbines for commercial electricity production can have very large 100 m diameter rotors. Despite this difference in size, all wind turbines have the same main components as shown in Figure 1.1.

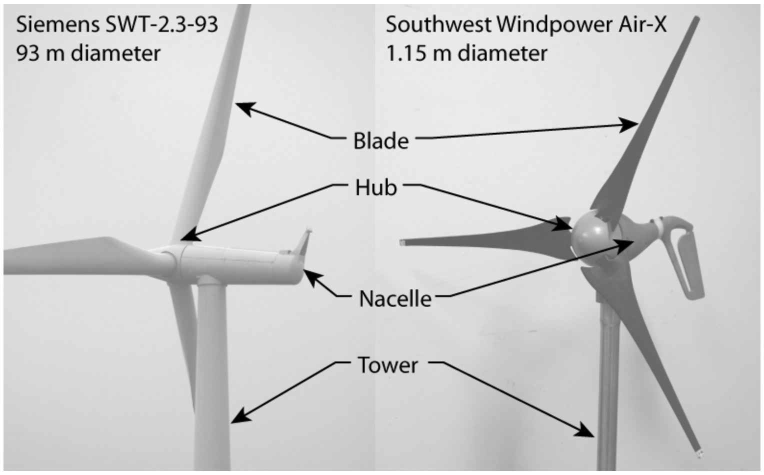

Figure 1.1: Main wind turbine components (not to scale)

Wind turbine blade geometry is based primarily on airfoil shapes. The airfoil is central to the operation of most devices that require a fluid environment for their operation. This includes airplane wings, helicopter rotors, and fan and turbine blades. Airfoils are primarily used to convert fluid forces into a lifting force normal to the flow direction. In the case of wind turbines, this lift force creates a torque which drives the wind turbine's generator. Important parts of an airfoil and terminology are shown in Figure 1.2.

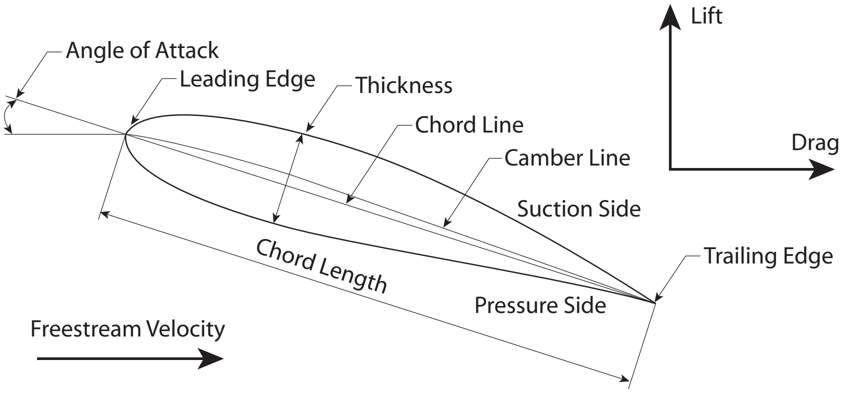

Figure 1.2: Airfoil overview

The angle of attack is the angle between the freestream velocity and the chord line. A blade for a small wind turbine can simply be a single airfoil extruded along the length of the blade. A blade for a large commercial wind turbine is tapered towards the tip and twisted. The twist is to ensure the angle of attack is relatively constant over the whole blade at the design point, since the relative velocity vector changes with radial position. Additionally, these large wind turbines will employ several different airfoil types along the length of the blade.

Wind turbine noise sources can be divided into two main categories: mechanical noise and aeroacoustic noise [4]. Mechanical noise is generated from the various moving components inside the nacelle, including the gearbox, generator, electrical transformer, and cooling systems. An increase in generator or gearbox noise often indicates a malfunction such as bearing wear or misaligned gear meshing [5]. Because these systems are housed inside the nacelle, sound-proofing, proper maintenance and careful design can mitigate mechanical noise. Aeroacoustic noise is generated by fluid structures such as vortices including the interaction of these structures with the tower and blades. Although mechanical noise can still be audible, aeroacoustic noise is the dominant noise source for most wind turbines. Oerlemans et al. [6] found the mechanical noise to be 10 dBA lower than the aeroacoustic noise for the majority of the audible frequency range. This measurement was performed with a microphone phased array (explained in Section 2.6) which allows noise sources to be localized and quantified. A number of aeroacoustic sources associated with wind turbines have been identified including: trailing edge noise, tip noise, stall noise, leading edge noise due to inflow turbulence, and blade-tower interaction noise [5]. These noise sources are shown schematically in Figure 1.3. Although all of these sources have been observed, trailing edge noise and tip noise have been identified as the dominant noise source in measurements of commercial size wind turbines [6, 7].

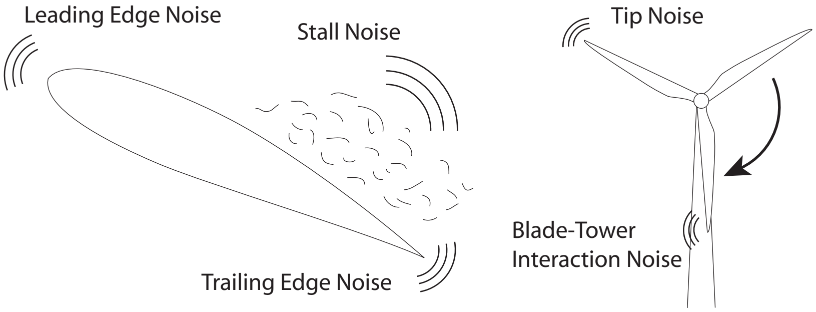

Figure 1.3: Aerodynamic noise sources from a wind turbine

Studying trailing edge and tip noise from a wind turbine in the field is a very difficult task since there is very little control over operating conditions such as wind speed, wind direction and background noise levels. This type of measurement was successfully completed by Oerlemans et al. [6, 7] however it required extensive planning, expertise and financial resources. A similar experiment was well beyond the scope of this thesis. A wind turbine blade is often modeled as a conventional airfoil moving through a non-rotating flow field. Although many wind turbine blades have varying airfoil shapes along the length of the blade and are twisted, individual spanwise blade elements can be analyzed as a two-dimensional (2D) airfoil. Aerodynamic experiments on airfoils are often performed in wind tunnels so there is complete control over parameters such as wind speed, angle of attack, and background noise levels. This is shown schematically in Figure 1.4.

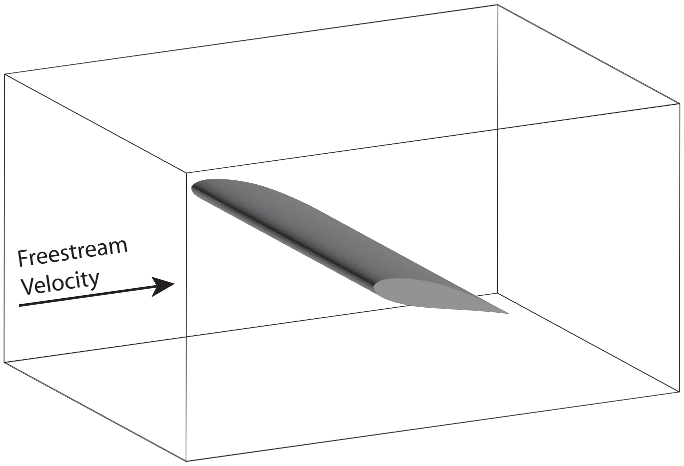

Figure 1.4: Schematic of a 2D airfoil in a closed test section wind tunnel

Tip noise can also be studied in a wind tunnel (as reported in Migliore [8]) however this cannot be done with a 2D airfoil. Tip noise was not investigated in this thesis because the facility to do so was not available. The goal of this thesis is to study trailing edge noise generation from a wind turbine specific 2D airfoil using a wind tunnel. Acoustic measurements and flow field measurements were made to assess the trailing edge noise and to find out how the flow field relates to the noise generation.

1.2 Outline

A literature review of low speed airfoil aerodynamics and wind tunnel testing is provided in Chapter 2. An overview of the flow field measurement tools used in this thesis such as the laser Doppler anemometer, smoke wire flow visualization and surface flow visualization are also provided. Lastly, background information is provided for airfoil trailing edge noise generation, and microphone and microphone phased array measurement techniques. Chapter 3 is a discussion of the experimental setup and measurement procedures used to collect data. This includes details on how the wind tunnel was modified to make it more efficient and quieter. Rationale is given for the choice of the 2D airfoil used in the tests. Specific details about the experimental setups for the flow visualization, laser Doppler anemometer, microphone and microphone phased array measurements are also given. The results from the wind tunnel and preliminary microphone phased array tests are presented in Chapter 4. Smoke wire flow visualization and surface flow visualization images are shown and compared to known low speed airfoil characteristics. The velocity and acoustic spectra of the airfoil wake is presented and compared. Additionally, the preliminary microphone phased array results are shown. Conclusions about the results from each type of measurement are presented in Chapter 5. Recommendations about how to improve the measurements are discussed in Chapter 6.

Chapter 2

Literature Review

This chapter provides a background for the aerodynamic theory and experimental techniques discussed in subsequent chapters. Wind tunnel testing of airfoils and low speed airfoil aerodynamics are reviewed. The theories behind flow visualization and laser based velocity measurements are presented. Basic acoustic theory is reviewed as well as trailing edge noise generation from an airfoil. Finally the microphone phased array acoustic measurement theory is presented.

2.1 Wind Tunnel Testing

2.1.1 Overview of Wind Tunnels

Wind tunnels are the primary tool for aeroacoustic and aerodynamic testing [9]. Two types of wind tunnels are used for aeroacoustic testing each with their advantages and disadvantages. They are the open jet/anechoic wind tunnel and closed test section wind tunnel.

Open jet/anechoic wind tunnel

An open jet anechoic wind tunnel has a test section where the jet is not bounded by walls but is surrounded by a larger anechoic enclosure [10]. This provides low background noise because there are no test section walls to cause sound reflections and the anechoic enclosure will absorb sound. However since the flow is unbounded, care must be taken when testing high lift devices which may deflect the jet away from the jet collector. This is shown schematically in Figure 2.1.

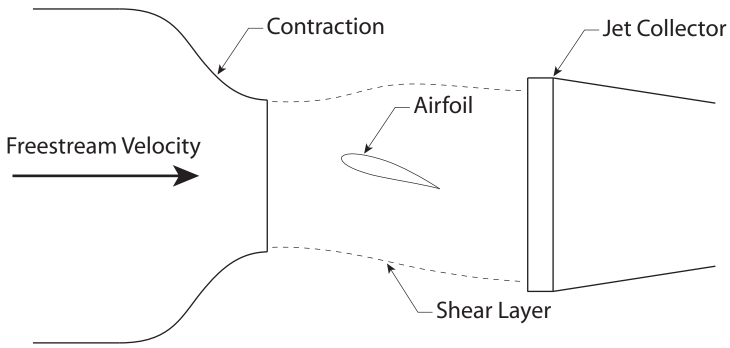

Figure 2.1: Side view schematic of open jet wind tunnel

Closed test section wind tunnel

The closed test section wind tunnel has higher background noise levels due to reflections off tunnel walls compared with the anechoic wind tunnel. A schematic of a closed test section wind tunnel is shown in Figure 1.4. Resonance can interfere with the results depending on test section and airfoil geometry. Despite this fact aeroacoustic tests can still be performed. The use of a microphone phased array can attenuate some of the background noise in the tunnel and the constrained flow allows for more predictable aerodynamic tests.

An interesting hybrid of these two aforementioned tunnel designs is the Virginia Tech Stability Wind Tunnel (VTSWT) [11] which uses stretched Kevlar® membranes to create test section walls inside an anechoic chamber. The Kevlar® is acoustically permeable allowing sound to travel through it and be absorbed in the anechoic chamber. The membranes are strong enough to mimic solid test section walls. Although it was not feasible to replicate the VTSWT design for this thesis, a number of modifications were made to the wind tunnel used to make it quieter and more efficient. These modifications are discussed in Section 3.1.

2.1.2 Wind Tunnel Resonance

Many researchers have found difficulties in performing aeroacoustic measurements in hard wall wind tunnels. Depending on test section geometry, airfoil size, and velocity, standing waves can develop in the test section which can have an amplitude the same order of magnitude as the airfoil acoustic emissions. This standing wave phenomenon was first investigated by Parker [12, 13], and Parker and Griffiths [14] who analyzed audible tones generated by various cascades of flat plates in a wind tunnel. Parker postulated that four primary resonant modes occur called α_P, β_P, γ_P, and δ_P which are shown below in Figure 2.2. The subscript P refers to Parker. The different modes are characterized

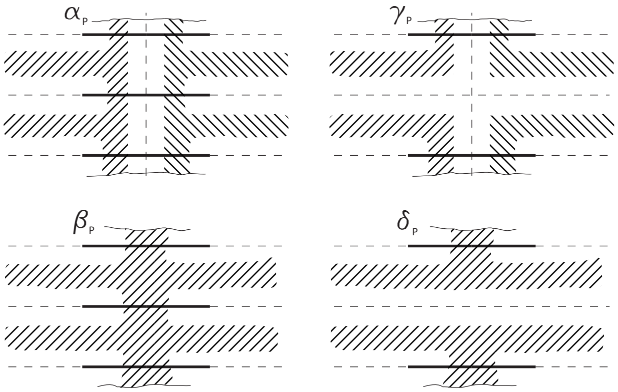

Figure 2.2: Parker [13] resonant modes, ///\\\ regions of high sound pressure level; - - - node; ——— plate

by the locations of nodes and antinodes along the standing wave. Antinodes are the high amplitude points along a standing wave and nodes are zero amplitude points. The distance between a node and a successive antinode is equal to one quarter wavelength. The β_P mode appears to be the most prevalent resonant mode in hard wall, closed test section wind tunnels since it was the only mode common in tests by Nash et al. [15], Nakano et al. [16, 17], Zaman et al. [18], and Wood [19] during airfoil experiments. Nash et al. [15] successfully mitigated the resonance by replacing the test section ceiling and floor with sound absorbing foam. Nakano et al. [16, 17] also attempted this, but were not able to completely remove the noise. An analytical method [13] was used to solve for the resonant frequency of each mode for a given chord length to tunnel size ratio. This model postulates that antinodes occur at the test section walls and a node occurs at the airfoil. The β_P mode resonant frequency can be calculated with Parker's [13] resonance model shown in Figure 2.3. The dimensionless frequency ratio ω/Ω is plotted against the geometry ratio c/h, where h is the test section height, and c is the airfoil chord. Here the angular frequency ω is defined as:

$$\omega = 2\pi f_r \tag{2.1}$$

where f_r is the resonant frequency. This is normalized by the reference frequency given by:

$$\Omega = 2\pi \frac{c_0}{\lambda_r} \tag{2.2}$$

where c_0 is the speed of sound and λ_r is the wavelength of the resonant standing wave. Rearranging Equations 2.1 and 2.2, the β_P mode resonant frequency f_{r,β_P} is calculated with:

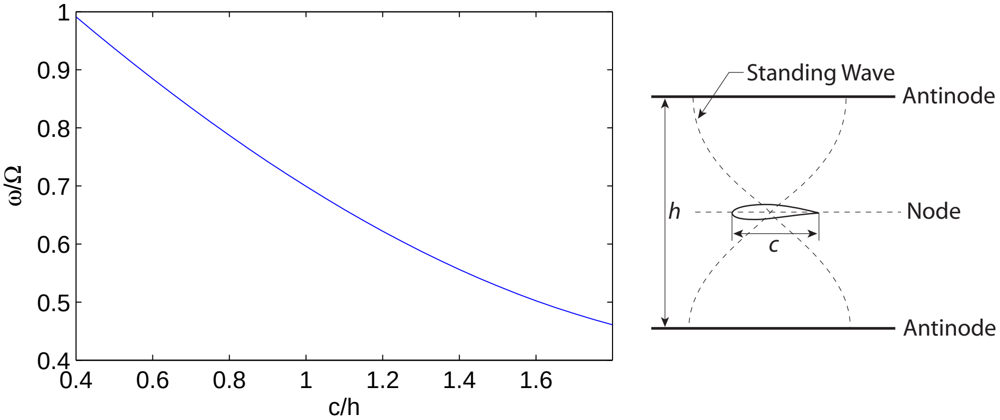

Figure 2.3: ω/Ω vs c/h from Parker [13] and standing wave schematic for β_P mode

$$f_{r,\beta_P} = \left({}^{\omega}\!/_{\Omega}\right) \frac{c_0}{\lambda_{\beta_P}} \tag{2.3}$$

where λ_{β_P} is the β_P mode wavelength equal to twice the test section height. The α_P, γ_P, and δ_P resonant modes are calculated in a similar manner but are not discussed here because they are less common in wind tunnel tests. According to the model, resonance only occurs when $\omega \lesssim \Omega$ and in the case of the β_P mode this occurs when ${}^{c}\!/_{h} \gtrsim 0.4$. Parker [13] hypothesized that additional resonant frequencies are possible caused by the superposition of standing waves or complex three-dimensional standing waves. It was also shown by Parker and Griffiths [14] that the generated standing wave frequencies produced an overlapping “ladder-like” relationship with freestream velocity as shown in Figure 2.4. Horizontal lines are added to the plot only to emphasize the "ladder-like" nature of the data.

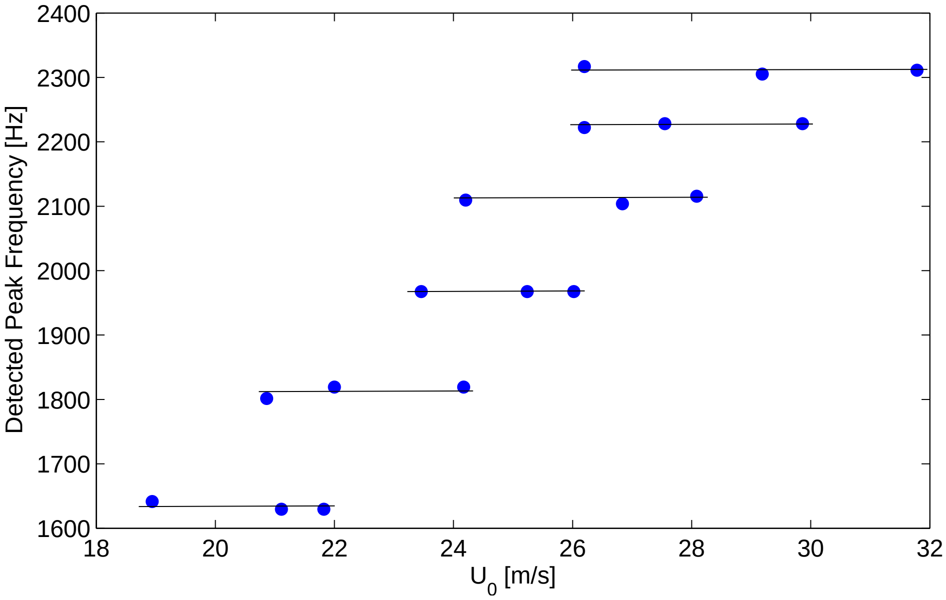

Figure 2.4: Detected peak frequency vs U_0 from Figure 5. b) in Parker and Griffiths [14]

2.2 Review of Low Reynolds Number Airfoils

When a wind tunnel test of an airfoil is performed, an important aspect to consider is the dimensionless Reynolds number based on chord length, Re_c, defined by:

$$Re_c = \frac{\rho U_0 c}{\mu} \tag{2.4}$$

where ρ is the fluid density, U_0 is the mean freestream velocity, c is the airfoil chord length and μ is the dynamic viscosity. Subsequent reference to “Reynolds number” shall refer to Re_c unless stated otherwise. The aerodynamic properties of an airfoil are primarily described by the Reynolds number. Two important properties are the section lift coefficient, c_l, defined by:

$$c_l = \frac{L}{\frac{1}{2}\rho U_0^2 c} \tag{2.5}$$

where L is the lift force per unit length and the section drag coefficient, c_d, defined by:

$$c_d = \frac{D}{\frac{1}{2}\rho U_0^2 c} \tag{2.6}$$

where D is the drag force per unit length.

The airfoil's Reynolds number attainable in the wind tunnel must be matched to the Reynolds number at which the airfoil operates since there are several airfoil Reynolds number regimes ranging from 10^3–10^9 each with their own flow characteristics [20, 21]. Two Reynolds number regions are of interest for this study which are: 3×10^4–7×10^4, and 7×10^4–20×10^4. These are the Reynolds numbers attainable in the wind tunnel used for this study which are discussed further in Section 3.1.

As fluid flows over the rearward portion of an airfoil an adverse pressure gradient can be encountered on both the suction side and pressure side if the fluid decelerates to fill a larger volume. For the Reynolds number regime of 3×10^4–20×10^4 the boundary layer is still laminar where the adverse pressure gradient is encountered. If the pressure gradient is too large, the laminar boundary layer does not have sufficient energy to remain attached to the airfoil and can separate forming a bluff body like wake. The adverse pressure gradient is affected by the airfoil's shape, thickness to chord ratio, (t_a/c), and angle of attack, α. Flow separation (which can occur on both the suction and pressure side) is more likely to occur for thicker airfoils and at higher angles of attack [20]. The adverse pressure gradient on the suction side increases with angle of attack thus increasing the chance of separation. Downstream of the separation point the flow becomes turbulent and can reattach to the airfoil because of the entrained energy in the turbulent boundary layer [20], as shown in Figure 2.5. When this occurs a "laminar separation bubble" forms between the separation point and reattachment point. The length of the separation bubble is the chordwise distance along the airfoil's surface between the separation and reattachment points. This length is used as the measure for separation bubble size. Carmichael [21] reports that for reattachment to occur, the Reynolds number based on separation bubble length must be at least 5×10^4. Therefore reattachment is not likely in the 3×10^4–7×10^4

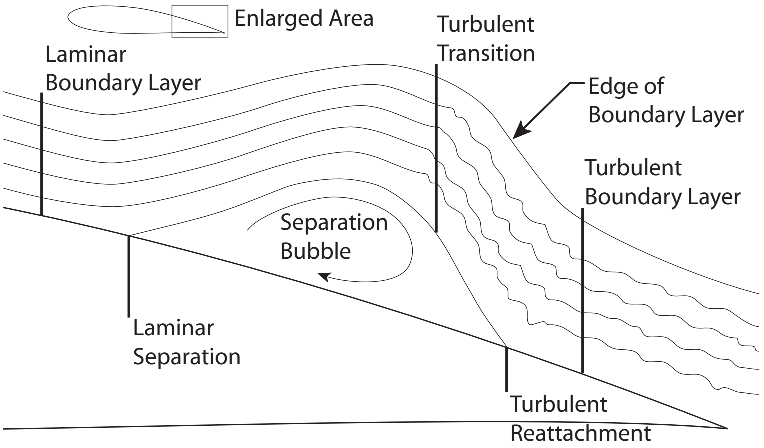

Figure 2.5: Laminar separation bubble evolution, adapted from Lissaman [20] (not to scale)

Reynolds number regime. Nakano et al. [16, 17] investigated the effect of separation bubble size and position on a NACA 0018 airfoil at $Re_c = 1.6 \times 10^5$ using surface flow visualization. As the angle of attack increased the separation bubble on the suction side decreased in size and moved upstream. The separation bubble on the pressure side also decreased in size but moved downstream. A similar but more extensive experiment on a NACA 0018 airfoil was performed by Gerakopulos et al. [22]. The size and position of the separation bubble on the suction side was measured with surface pressure measurements for angles of attack of 0°–10° and Reynolds numbers of 8×10^4–2×10^5. Gerakopulos et al. [22] measured the separation bubble to decrease in size and move upstream as the angle of attack increased. This phenomenon also occurred as the Reynolds number increased, although to a lesser extent. Hu and Yang [23] used surface pressure measurements to study the separation bubble on a cambered, 15% thickness, GA (W)-1 airfoil at $Re_c = 7 \times 10^4$. Their results also showed that the separation bubble on the suction side moved upstream as the angle of attack increased, however the separation bubble size did not change. The airfoil lift decreases and airfoil drag increases with the presence of a separation bubble, however the boundary layer near the leading edge can be tripped to induce turbulence thus eliminating the separation bubble and keeping the flow attached to the airfoil [20]. As the Reynolds number increases into the 7×10^4–20×10^4 regime, the size of the separation bubble decreases and its effect on lift decreases as well [21]. However the bubble is highly unstable and as the angle of attack increases the bubble can burst and not reattach to the airfoil [20]. Mueller et al. [24] investigated the hysteresis effect of the separation bubble size (and thus the lift and drag) caused by changing the angle of attack. The effect of turbulence intensity I was also investigated, which is defined as:

$$I = \frac{\sigma}{U_0} \tag{2.7}$$

where σ is the standard deviation of the freestream velocity component. It was found that above a turbulence intensity of 0.3% hysteresis was not present [24]. This result is important for very low turbulence wind tunnels where the lift and drag versus angle of attack curves are different depending on whether the angle of attack is increasing or decreasing.

2.3 Flow Visualization

Two methods are used in this thesis to qualitatively measure the flow around an airfoil including the laminar separation bubble. These methods are: smoke wire flow visualization and oil film visualization, which are discussed in this section.

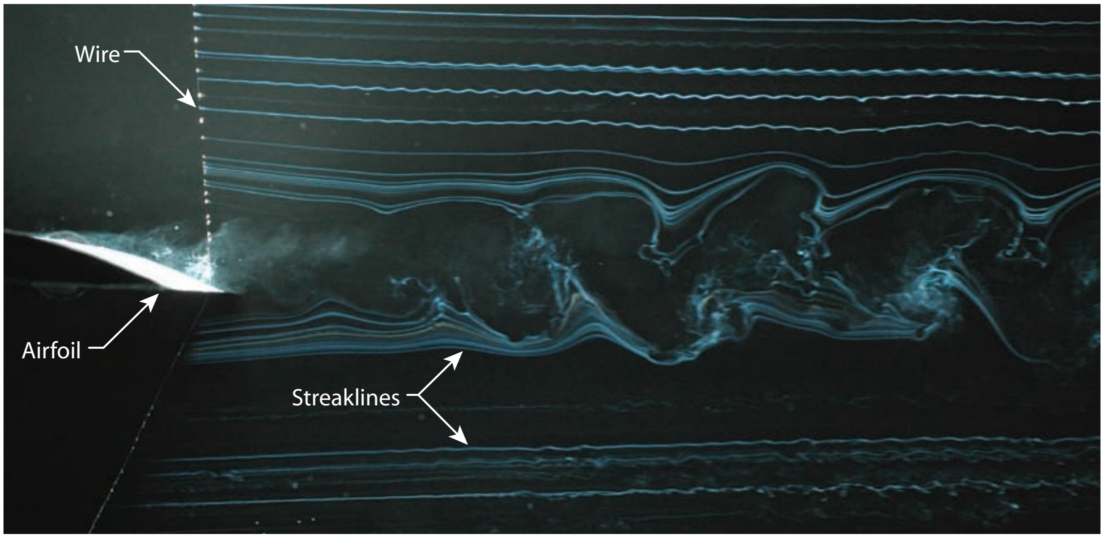

Figure 2.6: Smoke wire flow visualization $Re_c = 3.6 \times 10^4$ ($U_\infty = 10$ m/s), $\alpha = 8°$

2.3.1 Smoke Wire Flow Visualization

The smoke wire technique is used in air flows to visualize the streaklines around an object such as an airfoil [25]. This is achieved by stretching a small diameter wire through the flow near an object and applying an oil to the wire. AC electricity is sent through the wire, heating it and causing the oil to evaporate which creates the streaklines. Stainless steel wires with a diameter on the order of tens of microns are used in order to minimize vortices shed from the wire [25]. Typically this technique works best for air speeds slower than 10 m/s. Above this, the streaklines become too diffuse, the droplets of oil are blown off the wire, the smoke lasts only a fraction of a second and vortices from the wire can interfere with the flow. To properly photograph smoke wire streaklines, the camera's shutter speed must be fast enough in order to avoid blurring of the smoke. As the flow gets faster, a faster shutter speed is needed and a larger amount of light is needed to have properly exposed photographs. A light source such as a flash or high power spot light is used to provide the required lighting. Additionally a large aperture lens can be used to increase the amount light for exposure. An example of smoke wire flow visualization from this thesis is shown in Figure 2.6.

2.3.2 Oil Film Visualization

Surface flow visualization is a technique used to assess how fluid is moving over a solid body. Typically a pigment or tracer particle such as: dye, titanium dioxide, soot, or graphite powder, is mixed with a volatile fluid such as kerosene or silicone oil [26, 27]. The mixture is spread thinly over the model surface and then the wind tunnel is turned on.

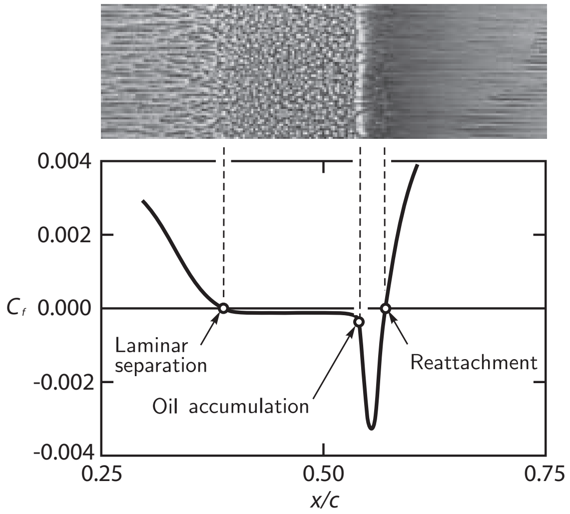

Figure 2.7: Surface flow visualization and skin friction coefficient from Selig and McGranahan [28]

Through a shearing effect, flow in the boundary layer will cause the mixture to move. The particles can create patterns and streaklines on the surface which will remain in place once the volatile fluid has evaporated. If the flow is primarily 2D, information about the flow above the surface can be gathered based on the surface pattern of the particles. A similar technique involves spraying on a less volatile fluid with tracer particles and observing how the flow affects the fluid surface. The tracer particles create streaklines on the surface. Selig and McGranahan [28] used this technique to locate the laminar separation on low Reynolds number airfoils. With this technique the laminar region, separation bubble region and reattachment region are easily visible through the appearance of the fluid surface as shown in Figure 2.7. Also shown is the corresponding estimate of skin friction coefficient, C_f, as a function of chordwise position along the airfoil (x/c) defined by:

$$C_f = \frac{\tau}{\frac{1}{2}\rho U_0^2} \tag{2.8}$$

where τ is the shear force of the fluid at the surface. Selig and McGranahan [28], also note that the oil mixture gathers at the downstream side of the separation bubble but the actual reattachment point is slightly downstream of this location.

2.4 Principles of Laser Doppler Anemometry

2.4.1 Theory

Laser Doppler Anemometry (LDA), also called Laser Doppler Velocimetry (LDV), is a non-intrusive, laser based, flow velocity measurement technique often used to study airfoils in wind tunnels [29, 30]. LDA was chosen for this study because it is capable of data rates on the order of tens of kilohertz allowing for spectral analysis at frequencies of a few kilohertz. Additionally since LDA is non-intrusive, measurements can be made without any apparatus affecting the flow inside the wind tunnel. Unlike many flow measurement devices, LDA measures the velocity of the particles in the flow rather than the flow itself. If a particle passes through a laser beam it will scatter light with a Doppler shifted frequency that is linearly proportional to the particle's velocity [31]. LDA systems use two laser beams where scattering from both beams is measured and the difference in frequencies yields the beat frequency. This frequency difference is on the order of megahertz to hundreds of megahertz which can be easily measured. Once the beat frequency is acquired the particle velocity can be calculated. The most common LDA setup is the dual beam configuration shown below in Figure 2.8 with the intersection angle θ. The following model is used to describe how the particle velocity is measured with Doppler shifted light. At the point where the beams cross there is an ellipsoid intersection volume which is the measurement volume. Where two laser beams cross, a time-averaged fringe pattern is created in the intersection region. This fringe pattern contains regularly spaced alternating bands of high and low intensity which is shown below in Figure 2.9.

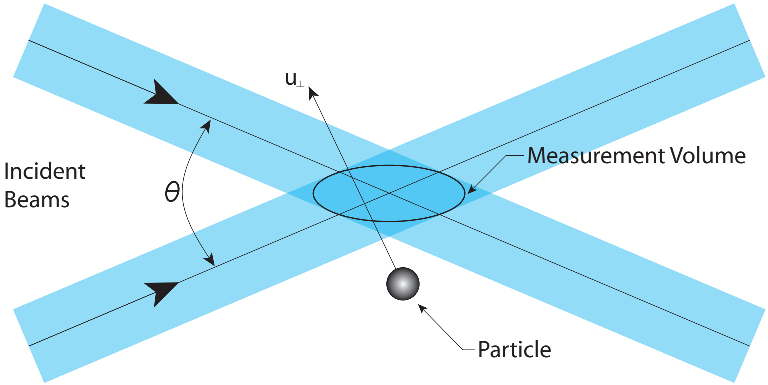

Figure 2.8: Dual beam LDA configuration schematic adapted from Albrecht et al. [31]

The fringe spacing δ_f given by:

$$\delta_f = \frac{\lambda_b}{2\sin\left({}^{\theta}\!/_{2}\right)} \tag{2.9}$$

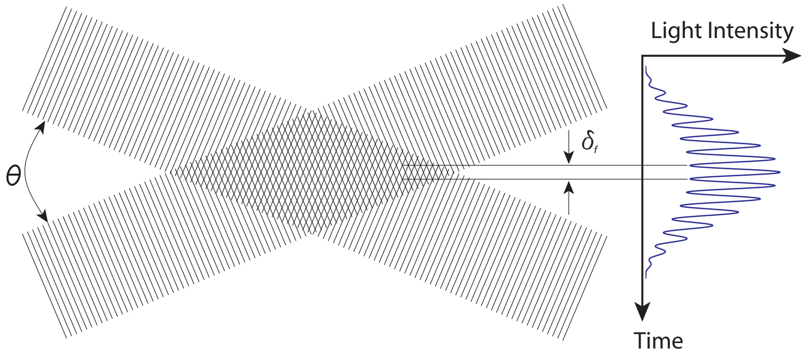

Figure 2.9: Dual beam LDA configuration schematic adapted from BSA Flow Software manual [32]

and is simply a function of the laser wavelength λ_b and the intersection angle θ [31]. When a particle moves through the fringes it scatters light at the beat frequency, also known as the Doppler frequency f_D given by:

$$f_D = \frac{2\sin\left(\theta/2\right)}{\lambda_b} u_\perp \tag{2.10}$$

where $u_\perp$ is the particle velocity component perpendicular to the fringes [31]. However the particle diameter, d_p, must be sufficiently small ($d_p \ll \delta_f$) for this to occur [31]. Rearranging Equation 2.10 the velocity is explicitly given by:

$$u_\perp = \frac{\lambda_b}{2\sin\left(\theta/2\right)} f_D = \delta_f f_D \tag{2.11}$$

2.4.2 Practical Considerations

A modification to this configuration is needed since the Doppler burst does not yield any information about particle direction. Only particles with non-zero velocities can be measured since stationary particles will not generate a Doppler burst [32]. By shifting the frequency of one beam by a small amount, f_0, the fringe pattern is modelled to move in the direction perpendicular to the fringes at a constant velocity u_{fringe} defined as:

$$u_{fringe} = \frac{f_0 \lambda_b}{2\sin\left(\theta/2\right)} \tag{2.12}$$

A Bragg cell can be used to shift the wavelength of one of the beams. Typically the frequency is shifted by 40 MHz [32]. This allows for stationary particles to scatter light as

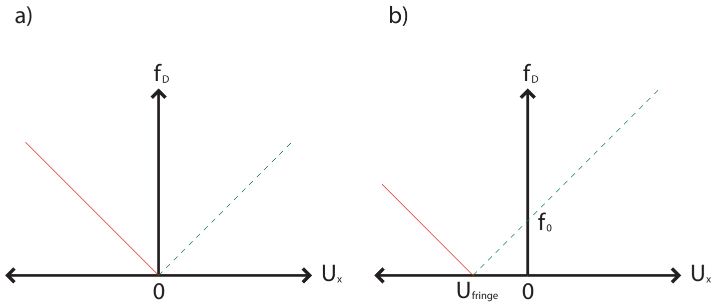

Figure 2.10: Relationship between Doppler shift and particle velocity, a) without frequency shift; b) with frequency shift. — ambiguous velocities; - - - measurable velocities (adapted from BSA Flow Software manual [32]).

well as directionality to be measured. A stationary particle will produce a Doppler burst equal to the shift frequency. Particles travelling against the fringes will produce a Doppler burst with a frequency higher than f_0, and particles travelling with the fringes will produce a Doppler burst lower than f_0. Therefore the lowest measurable velocity in the fringe propagation direction is u_{fringe}. There is no upper limit on measurable velocities in the direction opposite the fringe propagation. This is shown graphically in Figure 2.10 where the measurable velocities correspond to the dashed lines and unmeasurable (directionally ambiguous) velocities correspond to the solid lines. LDA systems can operate either in back scatter or forward scatter. In back scatter, the receiver is placed between the two incident beams so it receives scattered light. In forward scatter, the receiver is placed behind the particles. A much higher data rate is achievable with forward scatter because more light is scattered in the direction of the incident beam. With the backscatter setup the transmitting and receiving optics can be combined in one unit thus saving space and allowing for factory alignment.

2.5 Noise Overview

2.5.1 Noise Spectra

LDA is used in this thesis to measure the flow velocity around an airfoil and microphones are used to measure the noise generation. Prior to discussing acoustic measurement techniques a brief review of noise generation is required. Sound pressure levels, L_p, are quantified in units of decibels, dB given by:

$$L_p = 20 \log_{10} \left(\frac{p_{rms}}{p_{ref}} \right) \; [dB] \tag{2.13}$$

where p_{rms} is the root-mean-square (RMS) of the pressure signal in Pa and p_{ref} is the reference pressure of 20×10^{-6} Pa. Sound pressure levels are sometimes given in units of dBA, or A-weighted decibel levels. This weighting mimics the human ear's response to sound pressure levels at different frequencies [33]. It is common for sound to exist at more than one frequency, therefore it is useful to show this graphically as an acoustic spectrum where the decibel level for each frequency is visible as shown in Figure 2.11. The spectrum shows both tonal noise, characterized by a sharp peak and broadband noise, characterized by relatively flat energy levels over a range of frequencies.

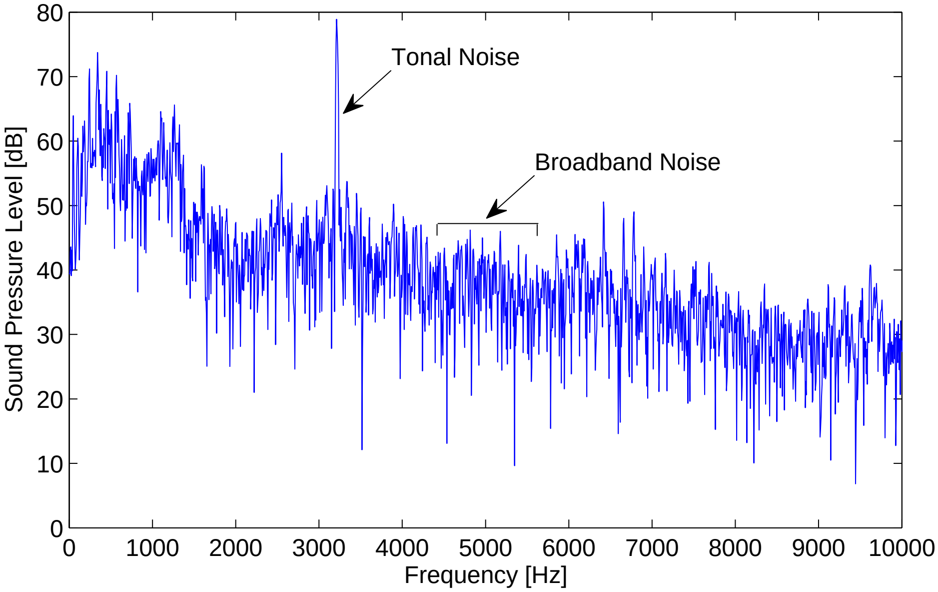

Figure 2.11: Example of a narrowband acoustic spectrum from a microphone measurement of the S822 airfoil

A Fast Fourier Transform (FFT) transforms the time domain acoustic signal (sampled at a constant time interval) into the frequency domain acoustic spectrum [34]. The FFT is used to convert a pressure versus time signal into a pressure versus frequency spectrum. Pressure values are at regularly spaced frequency bands $\triangle f$, given by: $\triangle f = {}^{1}\!/_{\triangle t T_b}$ where $\triangle t$ is the sampling interval in the time signal and T_b is the number of data points in the acoustic signal. This regularly spaced pressure versus frequency signal is known as a narrowband spectrum. In the acoustic spectrum, pure tones appear as narrow spikes and broadband noise appears as a relatively flat decibel level over a range of frequencies. Narrowband spectra are often converted to spectra where the band width is proportional to the frequency rather than being constant. The band is characterized by a center frequency f_c, an upper frequency f_u, and a lower frequency f_l which are related by: $f_c = \sqrt{f_u f_l}$ [33]. A typical band is the 1/3-octave-band where $f_u = 2^{1/3} f_l$, however other bands are used and in general for a $1/x$-octave-band, $f_u = 2^{1/x} f_l$. Using the root-sum-square (RSS) method, the pressure level for a proportional band p_{band}, is calculated given by:

$$p_{band} = \sqrt{\sum_{i=1}^{N_{band}} p_i^2} \tag{2.14}$$

where p_i is the i^{th} narrowband pressure level within the proportional band and N_{band} is the number of narrowband levels in the proportional band [34].

2.5.2 Noise Sources

Three common types of acoustic sources are: monopole, dipole, or quadrupole. Each source has a specific radiation pattern also called a directivity pattern. A monopole will radiate sound equally in all directions, an example being an open-ended resonator. Finch [35] defines a monopole pole as: "...any situation in which there is a fluctuation of density or pressure at a point.". Finch [35] also defines a dipole as: "...two monopoles of opposite strength-in other words, out of phase-are situated close to one another.". It has been shown experimentally that trailing edge noise is a dipole source [36]. The directivity function, D_h [36], for a high frequency trailing edge dipole source is given by:

$$D_h = \frac{2\sin^2\left(\phi/2\right)}{\left(1 + M\cos\phi\right)\left(1 + \left(M - M_c\right)\cos\phi\right)^2} \tag{2.15}$$

where ϕ is the angular position around the trailing edge, M is the Mach number given by:

$$M = \frac{U_0}{c_0} \tag{2.16}$$

and M_c is the convection Mach number where $M_c \approx 0.6M$ according to Hutcheson and Brooks [37]. This directivity function is for a stationary observer located in the plane normal to the trailing edge with the airfoil moving relative to the observer. A low frequency directivity function exists and is used when the wavelength is much larger than the airfoil chord [36]. The directivity function is shown in decibels for $M = 0.09$ in Figure 2.12.

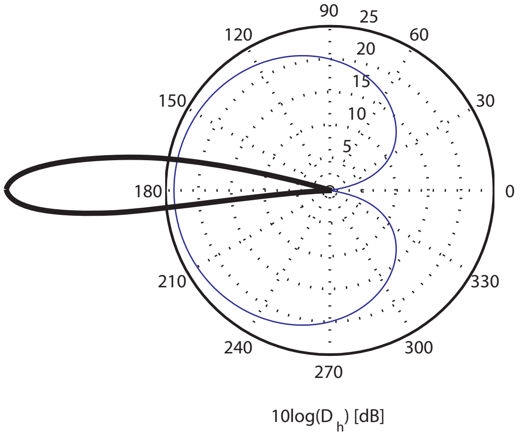

Figure 2.12: Directivity pattern (D_h) from a trailing edge dipole source with the airfoil moving $M = 0.09$ as measured by a stationary observer [36]

The majority of the energy from the trailing edge dipole source is radiated upstream and little is radiated downstream. It is clear from the directivity pattern that the location at which the source is measured will have a significant effect on the results. A quadrupole source is composed of a pair of dipole sources. Sound due to turbulence is regarded as a quadrupole source [38].

2.6 Microphone Phased Arrays

2.6.1 Overview

In aeroacoustics it is often useful to quantify acoustic sources as well as locate them spatially. Early sound localization methods involved aiming an elliptic dish, with a microphone at the focal point, at a sound source and moving the dish in order to scan a region. By measuring an acoustic source with an array of microphones sound can be localized without physically moving the array. This is done by shifting the microphone signals in time, effectively focusing the array on a specific point in space. The microphone phased array signal processing technique for sound localization is called beamforming. The beamforming process was first used in radio astronomy, seismic and sonar applications [39, 40]. A specific field of research has developed around optimizing the beamforming process and array design for aeroacoustic research. In addition to locating acoustic sources when multiple microphones are used, uncorrelated noise, ie: electrical noise or turbulence near the microphone, will be attenuated thus improving the signal-to-noise ratio of the reconstructed signal. The signal-to-noise ratio improvement in decibels, also called array gain, A_{gain}, is

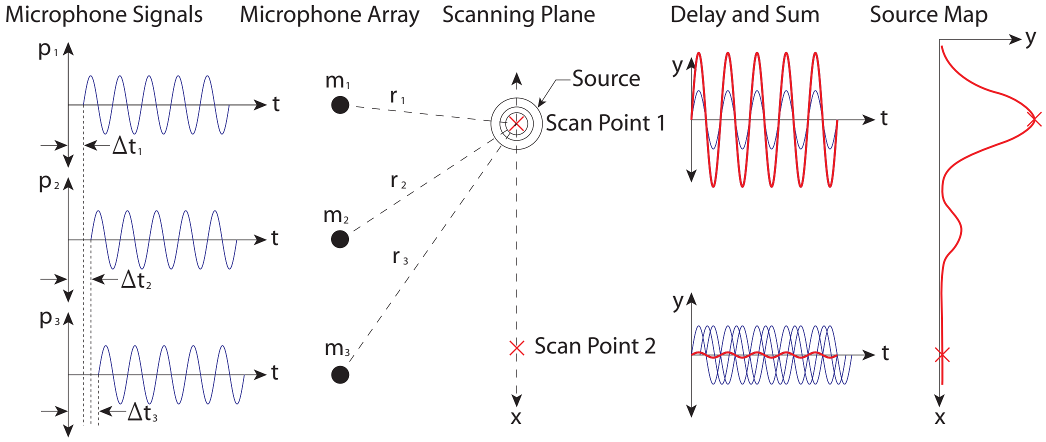

Figure 2.13: Delay and sum beamforming adapted from Oerlemans [41]

given below:

$$A_{gain} = 10\log\left(m_0\right) \tag{2.17}$$

where m_0 is the number of microphones [40]. The beamforming process will first be explained with the simplified delay-and-sum method in the time domain and then the widely used conventional beamforming method in the frequency domain will be outlined.

2.6.2 Delay-and-Sum Beamforming Theory

The beamforming theory can most easily be explained with the delay and sum method in the time domain. This is shown schematically in Figure 2.13 which was adapted from Oerlemans [41]. A single source emitting a constant amplitude pure tone and three microphones. All three microphones will measure a signal from the source, but each measured signal will have a modulated amplitude and phase shift based on distance from the source. A scanning plane comprised of grid points is defined where the acoustic source is thought to be located. For every grid point each microphone signal is phase shifted and the amplitude is scaled according to the distance between the grid point and the microphone. For the grid points where there is no source, the signal will add destructively, however for the grid point corresponding to the acoustic source, the signals will add constructively. The reconstructed signal at the source, y, at time, t, normalized by the number of microphones is given by:

$$y(t) = \frac{1}{m_0}\sum_{k=1}^{m_0} 4\pi r_k p_k \left(t + \frac{r_k}{c_0}\right) \tag{2.18}$$

where p_k is the signal measured from the k^{th} microphone, m_0 is the number of microphones, and r_k is the distance from the k^{th} microphone to the scan point [41].

2.6.3 Conventional Beamforming Theory

The most widely used beamforming method is known as “conventional beamforming” which is done in the frequency domain [42]. Conventional beamforming is similar to delay-and-sum beamforming except the microphone signals are weighted based on their proximity to the scan point and to the physical center of the array [41]. The following beamforming algorithm equations are adapted from the work of Humphreys and Brooks [42, 43, 44, 45]. Each microphone signal is divided into N blocks of equal length to which a windowing function is applied to reduce spectral leakage. Typical block lengths are powers of 2 from 1024–16384. A Fast Fourier Transform (FFT) is then performed on each block of data for each microphone signal. The cross-spectral matrix (CSM), $\hat{G}$ is then calculated for a single frequency by correlating all the FFT microphone signals as shown:

$$G_{ij}\left(f\right) = \frac{1}{m_0 w_s} \sum_{k=1}^{N} \left[P_{ik}^{*}\left(f\right) P_{jk}\left(f\right)\right] \; ; \; i, j = 1 \ldots m_0 \tag{2.19}$$

Here, P_{ik} and P_{jk} are the single-sided complex pressure spectrum for microphone pairs $[i, j]$, block k, where * denotes the complex conjugate, and w_s is the windowing weighting constant. The CSM is a $m_0 \times m_0$ matrix as shown:

$$\hat{G} = \begin{bmatrix} G_{11} & G_{12} & \ldots & G_{1m_0} \\ G_{21} & G_{22} & \ldots & \vdots \\ \vdots & \vdots & \ddots & \vdots \\ G_{m_0 1} & G_{m_0 2} & \ldots & G_{m_0 m_0} \end{bmatrix} \tag{2.20}$$

where the diagonal elements are the autocorrelation terms. The CSM improves the signal-to-noise ratio by attenuating uncorrelated signal noise. It is common practice to simply set the diagonal elements to zero [46] since the autocorrelation terms will amplify signal noise as given by:

$$\hat{G}_{diag=0} = \begin{bmatrix} 0 & G_{12} & \ldots & G_{1m_0} \\ G_{21} & 0 & \ldots & \vdots \\ \vdots & \vdots & \ddots & \vdots \\ G_{m_0 1} & G_{m_0 2} & \ldots & 0 \end{bmatrix} \tag{2.21}$$

The “steering vector”, $\hat{e}$ corresponds to the point in space where the beamforming algorithm is to be calculated and is given by:

$$\hat{e} = \begin{bmatrix} \frac{r_1}{r_c} \exp\left\{j 2\pi f \tau_1\right\} \\ \vdots \\ \frac{r_{m_0}}{r_c} \exp\left\{j 2\pi f \tau_{m_0}\right\} \end{bmatrix} \tag{2.22}$$

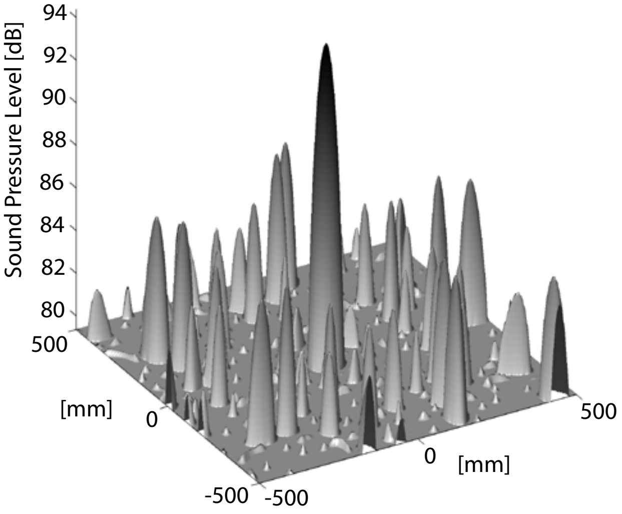

Figure 2.14: Source map of 8 kHz source located at (0,0)

In this, $r_{1 \ldots m_0}$ are the distances between the microphones and the scanning point, r_c is the distance between the array center and the scanning point, and $\tau_{1 \ldots m_0}$ are sound propagation times from the scanning point to each microphone. The distances $r_{1 \ldots m_0}$, and r_c are used as weighting factors for each microphone signal. The beamforming output, Y is calculated with matrix multiplication using the following:

$$Y\left(\hat{e}\right) = \frac{\hat{e}^{\dagger}\hat{G}_{diag=0}\hat{e}}{m_0^2 - m_0} \tag{2.23}$$

where † is the complex conjugate transpose. This output has units of pressure squared calculated for a specific scanning point $\hat{e}$ at a specific frequency. A plot of Y is called a beamform map or source map. Source maps are often presented for 1/3-octave-band levels for a center frequency. Using this algorithm, beamforming code written in MATlab was created, which could process simulated signals as well as experimentally acquired signals. The code is shown in Appendix D.

An example source map for a single 8 kHz source is shown in Figure 2.14. The largest lobe, indicating the source location, is called the main lobe and the other peaks representing erroneous sources are called side lobes. Array resolution is measured by a quantity called the beamwidth which is the diameter of the main lobe measured 3 dB below the peak [47]. The beamwidth b_w, overall diameter of the array (array aperture) D_a, frequency f, and array-to-source separation distance r are related with Equation 2.24, [41].

$$b_w \propto \frac{r}{D_a f} \tag{2.24}$$

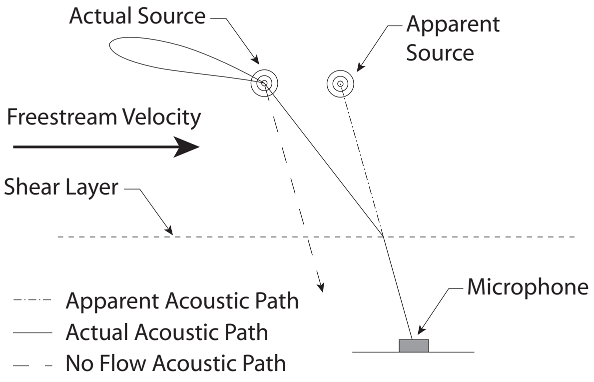

Figure 2.15: Refraction of sound through the shear layer in an open jet wind tunnel

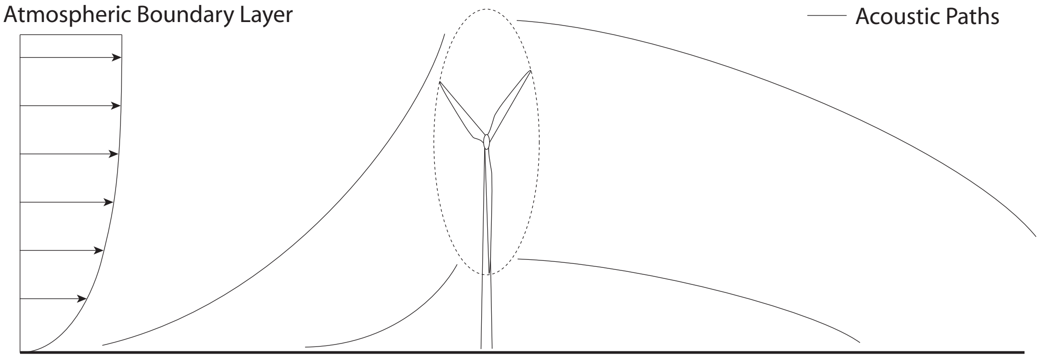

Figure 2.16: Refraction of wind turbine noise through an atmospheric boundary layer

If a non-stationary flow field is present between the array and the source plane, additional calculations must be performed to account for the convection of sound. In many aeroacoustic experiments a shear layer is present between the array and the source. This would be the case for an array outside the jet of an anechoic wind tunnel [43], or an array on the ground measuring a wind turbine [48, 49, 41]. As the acoustic rays travel through the shear layer refraction will occur, similar to refraction of light rays through a change in refractive index. This is shown schematically in Figure 2.15 for an airfoil in an open jet wind tunnel and in Figure 2.16 for wind turbine noise refraction through an atmospheric boundary layer. A loss in amplitude accompanies this sound refraction. Using Amiet's Method [50, 51], the change in sound direction and amplitude through a shear layer can be accounted for by modifying the steering vector in Equation 2.22. An example time-averaged source map where a shear layer was accounted for is shown in Figure 2.17. This

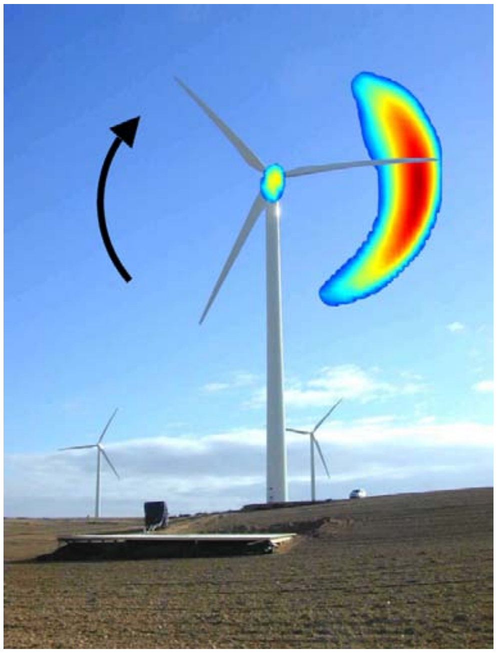

Figure 2.17: Beam map of a 58 m diameter turbine shown with a 12 dB range from Oerlemans [41]

result by Oerlemans [41] shows the noise from a 58 m diameter wind turbine measured with a 152 microphone array. The noise source is concentrated in the downswing area of the rotor plane due to the directivity pattern of trailing edge noise (shown in Figure 2.12).

2.7 Trailing Edge Noise Mechanisms

Numerous studies (including ones using microphone phased arrays) have been conducted to measure and understand how 2D airfoils generate noise [36, 17, 52, 53, 54, 15, 37, 45]. The majority of these findings are directly applicable to wind turbine noise. Trailing edge noise mechanisms associated with wind turbines are turbulent boundary layer trailing edge (TBL-TE) noise, laminar boundary layer trailing edge (LBL-TE) noise, and blunt trailing edge (BTE) noise [36]. Although the airfoil experiments in this thesis are only for low Reynolds numbers, noise associated with airfoils at high Reynolds are discussed for completeness.

Large commercial wind turbines have a Reynolds number based on chord greater than 10^6. At this Reynolds number the boundary layer has transitioned to become turbulent before the trailing edge as shown in Figure 2.18.

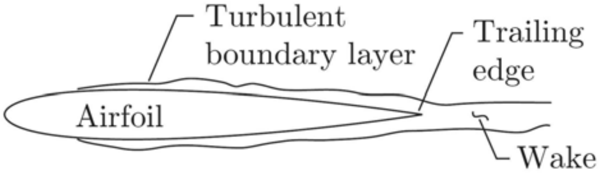

Figure 2.18: TBL-TE noise from McPhee [55]

Therefore the majority of commercial wind turbine aeroacoustic noise is due to TBL-TE noise which is broadband in nature. Trailing edge noise has been found to scale with the fifth power of the freestream velocity relative to the airfoil and linearly with the boundary layer thickness of the suction side [36]. It is common for the leading edge of wind turbine blades to develop pitting caused by erosion from precipitation, insects and dirt. This pitting can increase the boundary layer thickness thus causing an increase in TBL-TE noise. This phenomenon has been measured by Oerlemans and Lopez [6] when a grit strip, which simulated aggressive pitting, was applied to a wind turbine blade.

In some cases, laminar boundary layer vortex shedding can occur if $Re_c < 10^6$ [52]. A Kármán vortex street will develop at the trailing edge which will generate an audible pure tone. This is shown schematically in Figure 2.19.

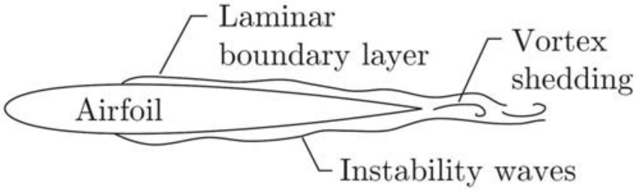

Figure 2.19: LBL-TE noise from McPhee [55]

The shedding frequency is often represented by the dimensionless Strouhal number, St given by:

$$St = \frac{f_s l}{U_0} \tag{2.25}$$

where f_s is the shedding frequency, l is a length scale (usually the chord length, boundary layer thickness, or projected frontal height). This phenomenon seldom occurs for commercial size wind turbines because the Reynolds number is sufficiently high such that the boundary layer becomes turbulent well before the trailing edge. However for smaller turbines (on the order of less than five kilowatts) that operate at lower Reynolds numbers this phenomenon can occur. Similar to TBL-TE noise, LBL-TE noise scales with the fifth power of the freestream velocity relative to the airfoil. However the LBL-TE noise scales linearly with the boundary layer thickness of the pressure side [36]. Previous researchers have found the shedding frequency to increase monotonically with flow velocity in the Reynolds number range of 3×10^4–20×10^4 [56, 36]. Yarusevych and Boutillier [56] attribute the distinct change in relationship between shedding frequency and Reynolds number to flow reattachment on the suction side of the airfoil as the Reynolds number increases. This is shown in Figure 2.20 where the Strouhal number is based on the projected frontal height of the airfoil, d. Flow reattachment on the suction side occurs at approximately the $\boxed{1}$ vertical line for the NACA 0018 airfoil and at the $\boxed{2}$ vertical line for the NACA 0025 airfoil. By using a length scale based on the wake geometry, Yarusevych et al. [57] and Yarusevych and Boutillier [56] were able to approximately collapse the Strouhal vs Reynolds number data for $\alpha = 0°$, $5°$, and $10°$. This lengthscale, denoted d^* is the separation between the freestream velocity RMS peaks measured at a distance of $x/c = 1.25$ from the trailing edge. This lengthscale is shown graphically in Figure 2.21. The separation without reattachment data collapses onto $St_{d^*} \approx 0.2$, and the separation with reattachment data collapses onto $St_{d^*} \approx 0.16$.

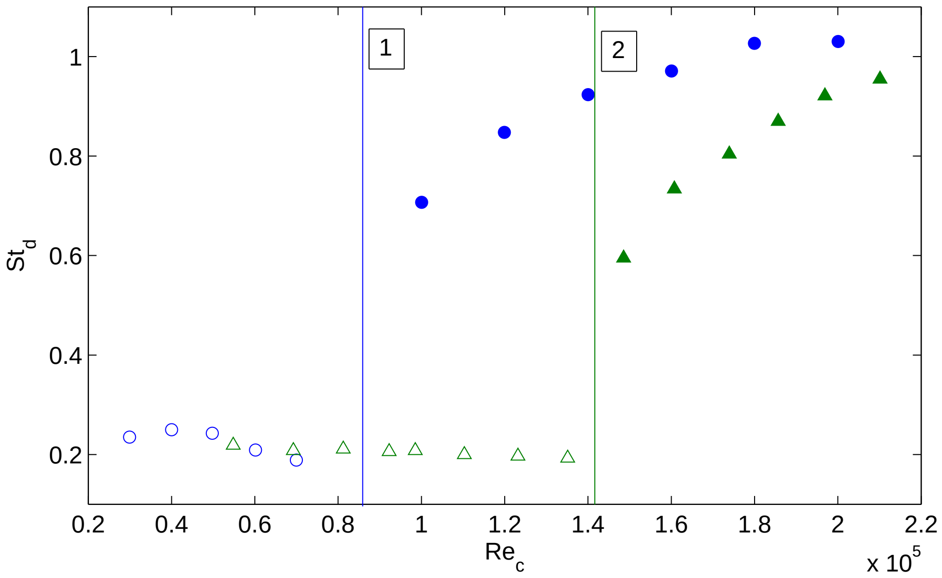

Figure 2.20: Strouhal vs Reynolds number plot for $\alpha = 10°$, ○ no flow reattachment, ● flow reattachment, NACA 0018 airfoil Yarusevych and Boutillier [56]; △ no flow reattachment, ▲ flow reattachment, NACA 0025 airfoil Yarusevych et al. [57]

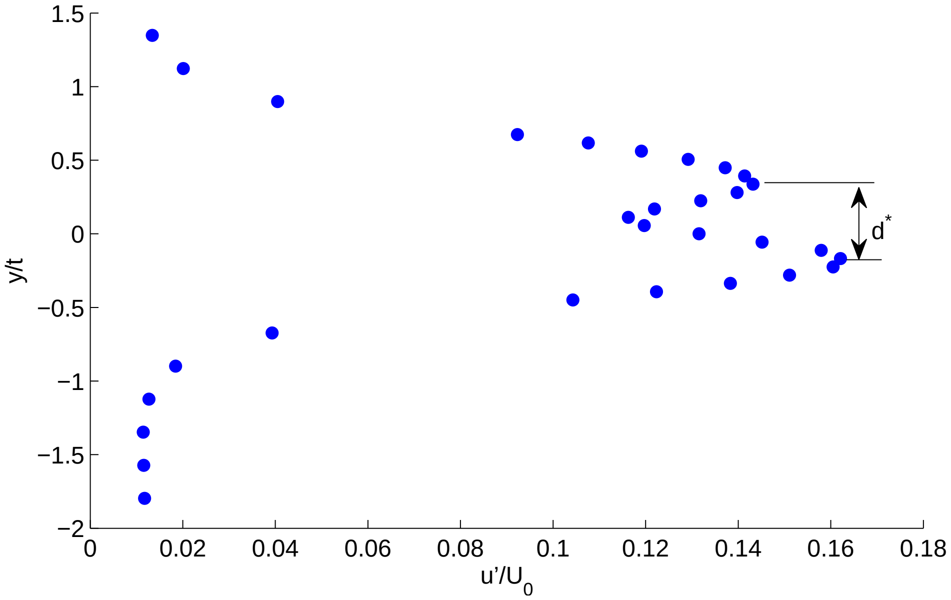

Figure 2.21: Example of normalized RMS freestream velocity wake profile from the S822 airfoil shown with d^* dimension

A pure tone can also be generated at the trailing edge in the event that the trailing edge thickness is 20% or greater than the boundary layer displacement thickness [36]. As flow passes over the blunt trailing edge a vortex is generated as shown in Figure 2.22. For the majority of wind turbines, blunt trailing edge noise is a minor concern since trailing edge thicknesses are sufficiently thin [6].

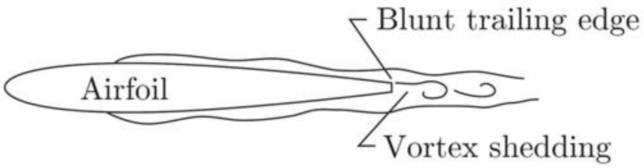

Figure 2.22: BTE noise from McPhee [55]

2.8 Reduction of Trailing Edge Noise

A number of research efforts have focused on modifying the airfoil shape as a means to control acoustic emissions. This includes the SIROCCO (SIlent ROtors by aCoustiC Optimization) project [58]. The SIROCCO airfoil was successful in lowering the acoustic emissions by 0.5 dBA. In a study by Oerlemans et al. [7], the addition of trailing edge serrations to a wind turbine blade was investigated. Results showed that these serrations lowered the trailing edge noise by 3.2 dBA. For high Reynolds number airfoils, leading edge pitting due to erosion can increase the turbulent boundary layer thickness thus increasing acoustic emissions. One of the current methods under investigation to prevent this is the use of leading edge tape which protects the blades. Conversely, Oerlemans [52] discovered that tripping the boundary layer on an airfoil for $Re_c < 10^6$ prevented the Kármán vortex shedding thus eliminating the pure tones. The boundary layer trip also reduced the broadband airfoil noise by up to 3 dBA. Therefore tripping the boundary layer reduces airfoil noise for low Reynolds numbers and increases noise for high Reynolds numbers. Additional research efforts by Moriarty and Migliore [59], and Oerlemans [41] have worked on developing semi-empirical wind turbine noise prediction algorithms based on the experimental work of Brooks et al. [36].

2.9 Correlating Velocity and Acoustic Measurements

In addition to studies focusing on acoustic measurements of trailing edge noise, some researchers have focused on the simultaneous measurement of the flow field around an airfoil and its acoustic emissions. The primary reason for the combined measurements is to understand the fluid structures that are responsible for the sound generation. Nash et al. [15] used a LDA and microphone to measure the flow and trailing edge noise of a NACA 0012 airfoil at $Re_c = 6.1 \times 10^5$ and angle of attack of 4°. A LDA was used because initial tests with a hot-wire anemometer revealed that the hot-wire support structure interfered with the flow. The fluctuating flow field in the boundary layer near the trailing edge was found to be coherent with the tonal noise measured with the microphone. Nash et al. [15] attributed the tonal noise to the amplification of Tollmien-Schlicting waves by the separation region found on the pressure side of the airfoil near the trailing edge. Tollmien-Schlicting waves are periodic instabilities found in the transition region between the laminar and turbulent boundary layer. These amplified instabilities are convected toward the trailing edge where they form the Kármán vortex street. The oscillating velocity field at the trailing edge convects upstream and it is hypothesized that this provides a feedback loop further amplifying the tonal noise [15]. This is shown schematically in Figure 2.23.

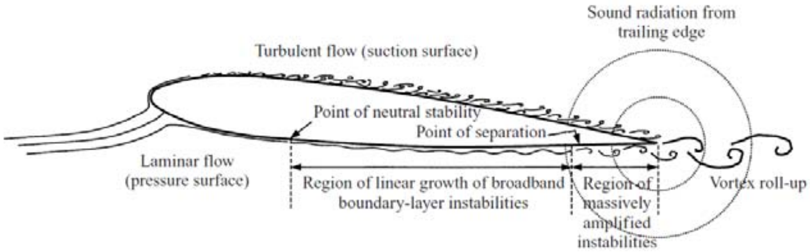

Figure 2.23: Schematic of airfoil instabilities from Nash et al. [15]

Nakano et al. [16, 17] used Particle Image Velocimetry (PIV), surface flow visualization, and a microphone to perform measurements on a NACA 0018 airfoil at $Re_c = 1.6 \times 10^5$. PIV is a laser and camera based fluid velocity measurement technique capable of acquiring two velocity components at multiple points simultaneously on a two-dimensional grid [60]. Tonal noise was measured with the microphone at angles of attack of 0°, 3°, and 6° and at higher angles there was no tonal noise. At angles of attack of 9° and greater flow separation without reattachment occurred on the pressure side of the airfoil. Nakano et al. [16, 17] report that the tonal noise is caused by fluctuations in the separation region near the trailing edge on the pressure side of the airfoil which create the observed Kármán vortex street. Similar to Nash et al. [15], Nakano et al. [16, 17] report that the tonal noise is amplified due to feedback between the vortices at the trailing edge convecting upstream and the separation region.

Other combined velocity and acoustic measurements studies are Schröder et al. [61], and Shannon et al. [62]. Both studies combine PIV and microphone measurements however the flow field, as is relates to the trailing edge noise production is not described in great detail.

Chapter 3

Experimental Setup

A detailed overview of the experimental setup and measurement tools are given in this chapter. This includes a description of the wind tunnel used for the experiments and the modifications undertaken to improve its quality. The size of the wind tunnel dictated the type of airfoil that could be properly tested. Rationale for choosing the S822 wind turbine airfoil is provided. Descriptions of the experimental setups for the smoke wire flow visualization and oil film visualization are given. The method used to measure the velocity field with the LDA is provided along with the microphone method to measure the acoustic field. Finally the experimental setup for the preliminary testing of the microphone phased array is discussed.

3.1 Wind Tunnel Modifications

The wind tunnel designed and built by Sperandei [63] suffered from high turbulence intensity and high background noise levels. The cause of the high turbulence intensity was found to be flow separation in the diffuser. This separation was mitigated by adding vanes in the diffuser. The turbulence intensity was further reduced with the addition of a modified turbulence reduction screen section. The background noise level was reduced with the addition of sound absorbing foam to the inside of the wind tunnel walls. These modifications are described further in the following sections.

3.1.1 Diffuser Modification

The closed test section recirculating wind tunnel used in this thesis was designed and constructed by Sperandei in 2002 [63]. The test section has a square cross-section of 152.4 mm × 152.4 mm that is 450 mm long. Flow is driven by an axial fan controlled by a Variable Frequency Drive (VFD) allowing for precise control of freestream velocity. A schematic of the wind tunnel from Sperandei [63] is shown in Figure 3.1.

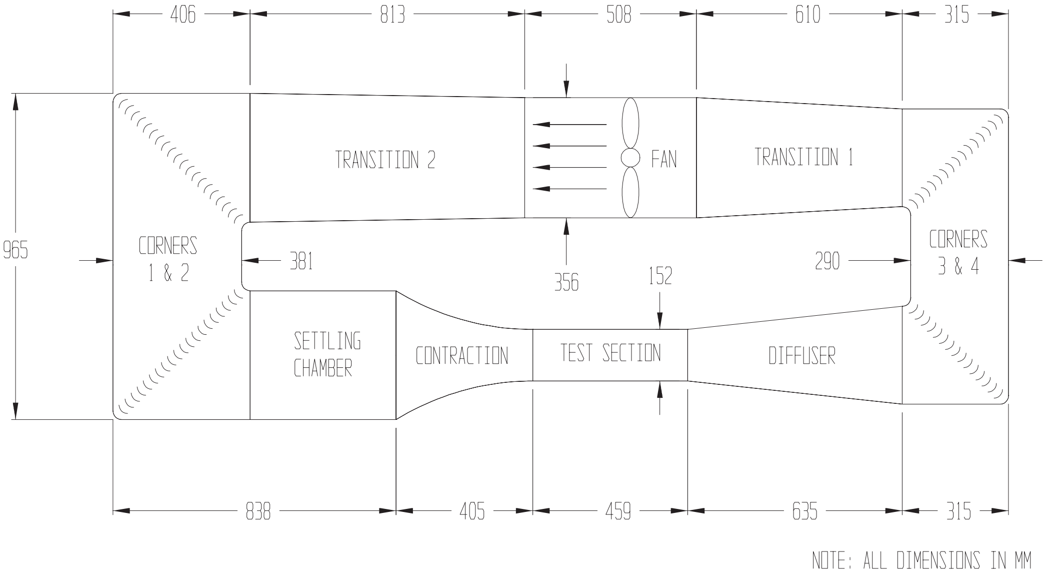

Figure 3.1: Schematic of the wind tunnel from Sperandei [63]

The design included a wide angle diffuser which was used to reduce the overall length of the wind tunnel. Although the wide angle diffuser could potentially cause flow separation a review of wind tunnels with wide angle diffusers by Mehta [64] suggested that separation was unlikely with this diffuser geometry. McPhee [55] later discovered a surging phenomenon in the flow which was postulated to be attributed to either flow separation in the diffuser or the stalling of the fan blades. A method to reduce diffuser separation is to install a wire screen at the inlet of the diffuser to break up the boundary layer. Although this method works, it significantly increases the head loss in the wind tunnel thus lowering the maximum attainable test section velocity. McPhee [55] used this wire screen method which eliminated the surging phenomenon and lowered the turbulence intensity, however the maximum test section velocity was reduced from 35 m/s to 26 m/s. At this point it was not perfectly clear whether or not the screen prevented separation in the diffuser or increased the head loss such that the fan was operating more efficiently and not stalling.

In order to confirm if the surging phenomenon was a result of separation in the diffuser or the fan stalling, the LDA was used to measure the effects of various wire screens installed throughout the tunnel in order to replicate the head loss of the diffuser inlet screen. The freestream velocity and turbulence intensity were measured at the center of the tunnel at a location 150 mm downstream of the test section entrance. These experiments were performed by Bale [65]. If the surging phenomenon still occurred the flow separating in the diffuser would be the probable cause. If the surging disappeared the probable cause would be the fan operating inefficiently. The results showed that only a screen at the inlet to the diffuser prevented the surging, thus the cause was the flow separation in the diffuser.

Smoke wire flow visualization tests were used to confirm that the flow was separating in the diffuser. The smoke wire was placed at the center of the tunnel at downstream locations of 100 mm and 500 mm from the diffuser inlet. Holes were drilled in the side of the diffuser in order to hold the smoke wire in place. Tests were conducted with a test section velocity of 5 m/s with and without the diffuser inlet screen. This was the highest velocity at which the smoke could most easily be photographed. It was found that the smoke wire closest to the inlet of the diffuser did not clearly reveal any details about the possible flow separation. However the downstream smoke wire clearly showed the existence of flow separation. Shown in Figure 3.2 is a comparison of the flow with and without the diffuser inlet screen. The screen creates a coherent core flow which reduces separation, whereas with no screen the flow was highly chaotic.

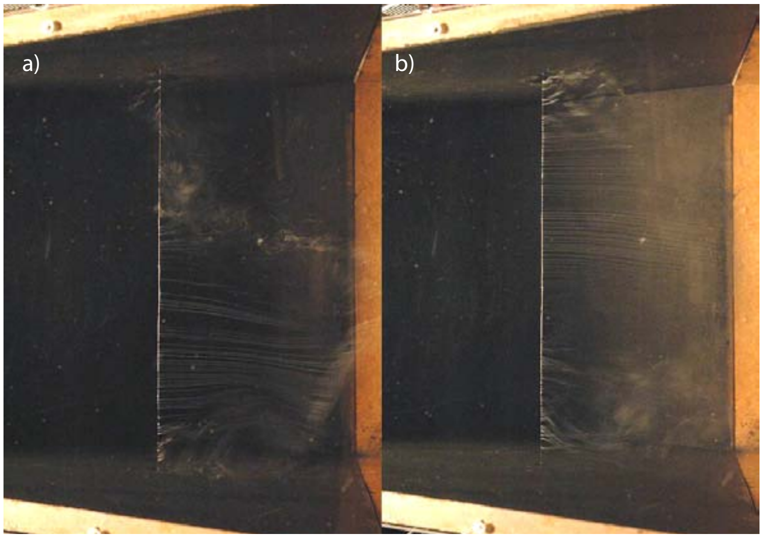

Figure 3.2: Comparison of diffuser flow a) without screen; b) with screen. Flow is from left to right.

Barlow et al. [9] recommends using diffuser vanes to prevent separation and does not recommend using a diffuser inlet screen. This method was chosen because of its reported effectiveness and ease of installation. The diffuser vanes were constructed from 4 pieces of slotted 18 gauge steel which were tack welded together at either end. Steel was chosen over aluminum because of its strength so it would not vibrate or flex due to the wind. A 3×3 cell vane arrangement was chosen to achieve a full angle of 4.1° per cell, ensuring the flow will not separate [66]. A larger number of cells would only increase the head loss of the wind tunnel. The LDA system was used to assess the effectiveness of the diffuser vanes. Results showed that the maximum freestream velocity (at a VFD setting of 60 Hz) increased from 39.3 m/s to 40.2 m/s. This means that the wind tunnel is more efficient with the diffuser vanes in place. The turbulence intensity decreased with the addition of the diffuser vanes as shown in Figure 3.3. By preventing flow separation, the diffuser vanes effectively reduced the turbulence intensity from approximately 1.5% to 0.8%. All subsequent tests are with the diffuser vanes in place.

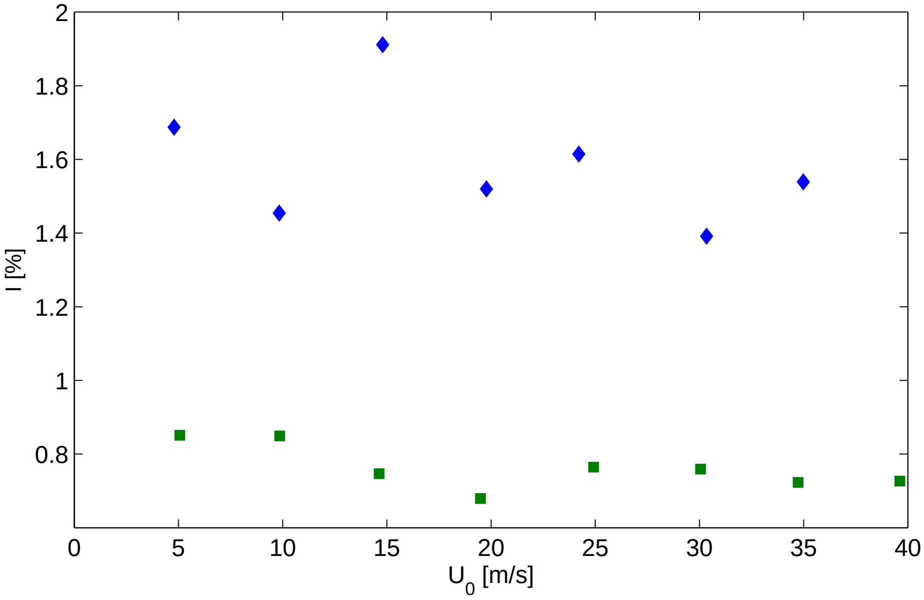

Figure 3.3: Turbulence intensity vs freestream velocity with and without diffuser vanes, ♦ no diffuser vanes; ■ with diffuser vanes

3.1.2 Turbulence Reduction Screens

Wind tunnels primarily employ two devices to reduce turbulence intensity: honeycomb flow straighteners and wire mesh screens. Honeycomb flow straighteners serve to reduce the lateral fluctuations and the wire mesh screens reduce the streamwise fluctuations [9]. Both of these devices were installed at the inlet to the contraction in the wind tunnel. The ratio of open area to wire area of a screen is called the porosity and is often expressed as a percentage. Mehta and Bradshaw [67] recommend screens with a porosity of 57% or higher in order to reduce instabilities. The single screen originally installed by Sperandei had a porosity of 54% and therefore was replaced. A new screen box which holds the turbulence reduction screens is outlined below.

Criteria

- The screen box design must be as simple as possible in order to minimize manufacturing and installation time.

- The screen box must be as short as possible in order to not unnecessarily increase the overall wind tunnel length.

Constraints

- The new screens must lower the turbulence intensity of the wind tunnel
- The design must allow for a method to clean the screens without any disassembly.
- The screen porosity must be 57% or more [67].
- The screen box must be able to attach easily between the existing contraction and settling chamber.
- The distance between screens must be at least 25 times the screen mesh length, as recommended by Groth and Johansson [68].

Based on the listed criteria and constraints a screen box was designed. It is a square frame made from 38.1 mm square aluminum tubing with a 3.18 mm wall thickness. Size 30 mesh screens with a porosity of 65% and mesh length of 0.85 mm, were stretched over and fixed to each side of the frame. The mesh size refers to the number of cells per linear inch. A window was cut into one side of the frame to allow access between the screens for cleaning. An extension the same size as the screen box was added between corner 1 and the fan. Bolting patterns with accompanying angle brackets were designed to attach the screen box between the existing contraction and settling chamber. The finished screen box is shown in Figure 3.4 with one screen attached.

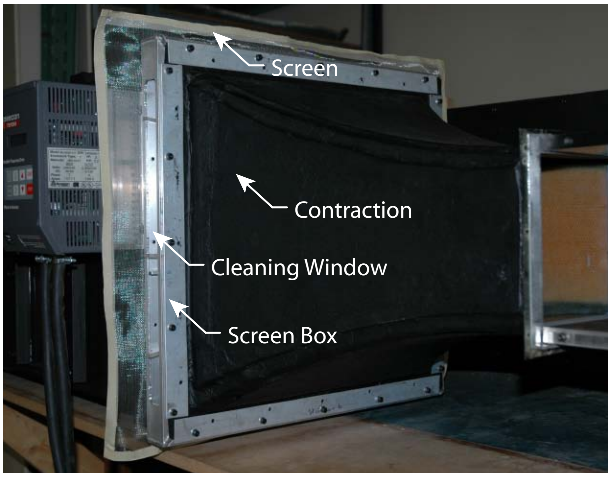

Figure 3.4: Screen box

Using the LDA the turbulence intensity was measured for one screen and with two screens. The turbulence intensity vs freestream velocity is plotted in Figure 3.5 for both cases. The turbulence intensity is below 1% and decreases to approximately 0.75% at the maximum freestream velocity. There is no significant change in turbulence with the addition of the second screen. This could be due to insufficient spacing between screens. Although Groth and Johansson [68] recommend a spacing of 25 times the mesh length (in this case a separation of 21 mm), Mehta and Bradshaw [67] recommend a spacing approximately equal to 0.2 times the settling chamber diameter (in this case 76.2 mm). Due to the pressure drop across each screen the maximum freestream velocity (at a VFD setting of 60 Hz) was reduced from 40.2 m/s to 39.0 m/s. It was reasoned that both screens should be left in the wind tunnel, despite the loss in maximum freestream velocity, in an attempt to reduce any turbulence that the acoustic foam (discussed in the next subsection) might add.

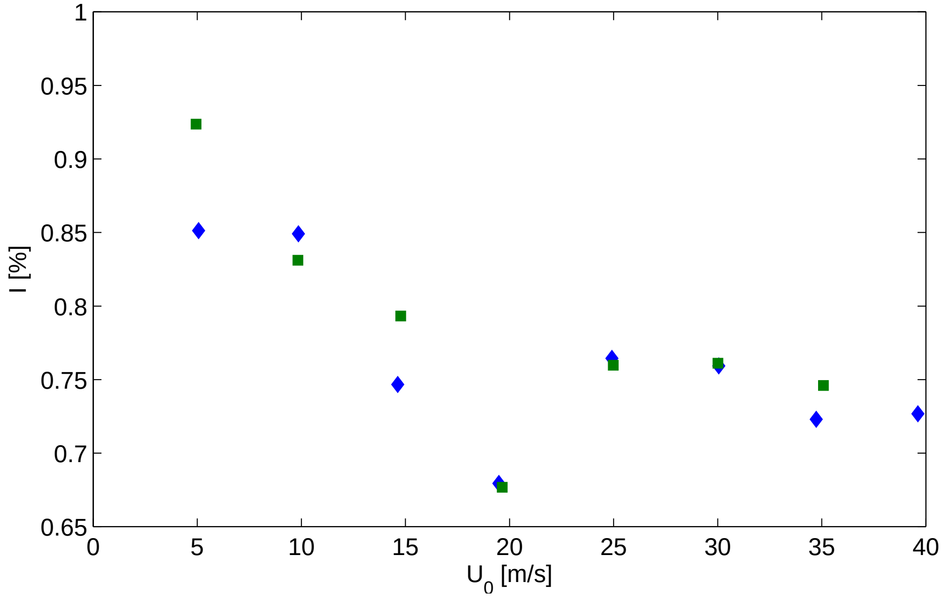

Figure 3.5: Turbulence intensity vs freestream velocity,♦ one turbulence screen; ■ two turbulence screens

3.1.3 Acoustic Foam

Due to the relatively small separation between the wind tunnel fan and the test section, fan noise easily travels to the test section. In order to improve the quality of the aeroacoustic experiments the background noise level in the test section needed to be lowered. The simplest way to accomplish this was the addition of sound absorbing foam [11]. Three types of sound absorbing foam were considered: Armacell SA Duct Liner, Whispertone®

Tackboard, and Melamine foam. All three foams have limited sound absorption below approximately 500 Hz, and improved sound absorption as the frequency increases. The Melamine foam was chosen because of its superior sound absorption and proven capabilities at the VTSWT [11]. The foam was placed inside the walls between corners 1 and 2, and corners 3 and 4, as shown in Figure 3.1. It was impractical to have the foam flush mounted inside the tunnel therefore it was simply attached to the wind tunnel walls. A foam thickness of 12 mm was chosen to minimize the constriction effect on the flow. Additionally the foam was chamfered on either end in order to reduce the risk of flow separation. The foam was glued to sheets of cellophane, which were then fixed to the wind tunnel walls with double sided tape. This provided a semi-permanent attachment in case the foam needed to be removed in the future.

Background noise level results for a test section speed of 20 m/s are shown below in Figure 3.6. The narrowband noise spectrum is plotted in decibels with a frequency range of 0–5000 Hz. As expected the acoustic foam has virtually no effect below 500 Hz. However above this the background noise level is clearly attenuated.

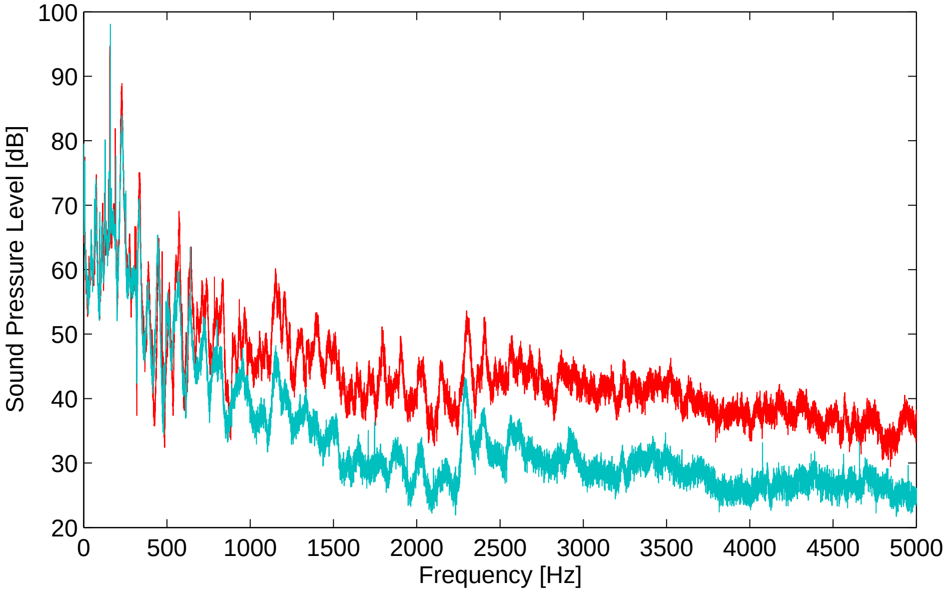

Figure 3.6: Test section background noise levels, — without acoustic foam; — with acoustic foam

In an attempt to further reduce the background noise and prevent resonance a test section ceiling panel lined with Melamine foam was constructed. This modification was implemented by Nash et al. [15] and successfully reduced resonance. For this study the foam lined test section did not significantly lower the background noise level. Additionally the foam caused a 17% reduction in flow velocity for a given fan frequency setting. Although this effect was not thoroughly investigated it is believed to be caused by the relatively rough surface of the foam compared to the other smooth test section walls. For these reasons the foam lined ceiling panel was not used in further tests. It was later found that the foam panel did not prevent test section resonance.

3.1.4 Glass Test Section Front Panel

The front panel of the test section constructed by McPhee [55] was made from 12.7 mm thick Lexan. Preliminary LDA tests showed that this had detrimental effects on the maximum achievable data rate. Impurities in the Lexan cause this poor data rate and a 3 mm thick piece of float glass was used instead because of its superior optical characteristics. The new front glass panel along with the supporting hardware are shown in Figure 3.17.

3.1.5 Final Wind Tunnel Calibration

After all wind tunnel modifications, the final wind tunnel calibration was performed with the LDA to determine the relationship between VFD frequency and freestream velocity and turbulence intensity. Two calibration tests were done in order to determine the repeatability of the wind tunnel and to create an average calibration curve. Temperature measurements of the flow inside the test section were performed in conjunction with the velocity measurements. This was done so the air density and viscosity (and thus the Reynolds number) could be accurately calculated and so that subsequent tests could be performed at the same temperature. A K-type thermocouple was used along with the measurement system employed by McPhee [55]. A period of approximately 10 minutes was allowed to elapse between VFD setting measurements to allow for the wind tunnel to heat up and reach a steady state. Both velocity and temperature results are presented in Figure 3.7.

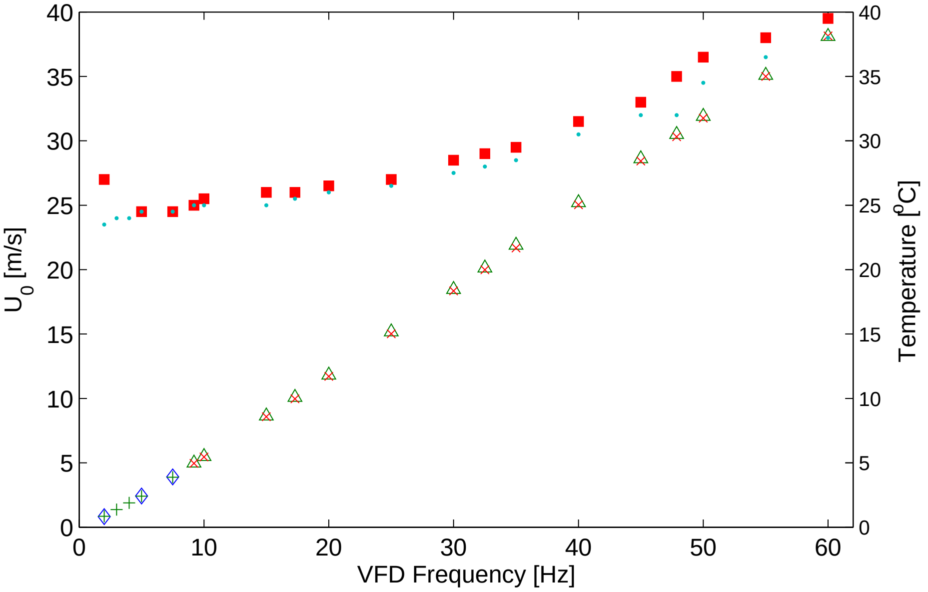

Figure 3.7: Freestream velocity and temperature vs VFD frequency, ◇, low speed test 1; +, low speed test 2; △, high speed test 1; × high speed test 2; ■ temperature test 1; ● temperature test 2

Each calibration curve was extremely linear except for low VFD settings below approximately 7.5 Hz. Because of this a low speed (below 7.5 Hz) and a high speed (above 7.5 Hz) calibration curve were created using linear regression. The average low speed calibration is given by:

$$f_{VFD,l} = \frac{U_0 + 0.2148}{0.5272}\,;\ (f_{VFD,l} < 7.5\,Hz) \tag{3.1}$$

where $f_{VFD,l}$ is the VFD setting in Hz and U_0 is the freestream velocity in m/s. The average high speed calibration is given by:

$$f_{VFD,h} = \frac{U_0 + 1.215}{0.6575}\,;\ (f_{VFD,h} > 7.5\,Hz) \tag{3.2}$$

where $f_{VFD,h}$ is the VFD setting in Hz and U_0 is the freestream velocity in m/s. Both calibration curves have an R^2 value of 0.999. Due to the blockage of the acoustic foam the maximum freestream velocity (at a VFD setting of 60 Hz) was reduced from 39.0 m/s to 38.2 m/s. Temperature results show that the air in the wind tunnel heated up significantly at higher speeds. Since the fan's motor is in the flow, heat from the motor is added directly into the wind tunnel. Freestream turbulence intensity results are shown for both tests in Figure 3.8. Compared to the pre-acoustic foam data (Figure 3.5) the turbulence intensity with the acoustic foam increased to approximately 1.1%. Although undesirable, the increased turbulence due to the acoustic foam was deemed worth the decrease in background noise levels.

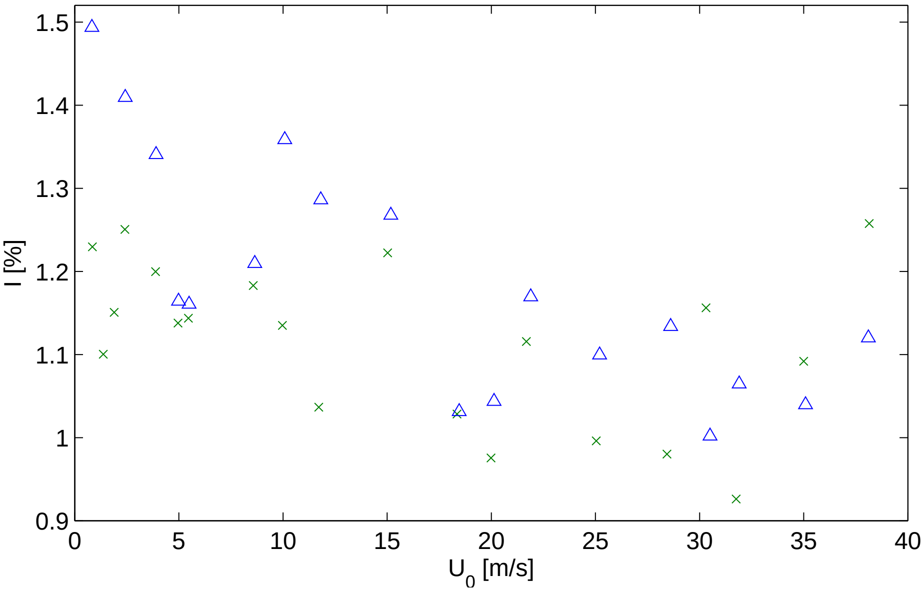

Figure 3.8: Turbulence intensity vs freestream velocity from final calibration, △ test 1; × test 2

3.2 Airfoil Selection

Airfoil selection was primarily dictated by the geometry and maximum freestream velocity of the wind tunnel. Due to the size of the wind tunnel, only an airfoil designed for low Reynolds number could be properly tested. The selection of a wind turbine specific airfoil was a secondary constraint. Wind turbine airfoil requirements differ significantly from aircraft airfoils. Examples of a detailed description of the wind turbine airfoil design process are given by Somers [69, 70]. Because of the particular design constraints, the National Renewable Energy Laboratory (NREL) has designed a family of airfoils for different sections of the blade and for different sized wind turbines [69, 70]. The S822 airfoil is designed for the tip of 3–10 m diameter wind turbines with a Reynolds number range of 10^5–8×10^5 [69]. The tip airfoil was chosen because it is thinner than the root airfoil allowing for a lower frontal area blockage ratio in the wind tunnel. Frontal area blockage is defined as the ratio of the projected frontal area of the airfoil to the test section cross-sectional area. The S822 airfoil is shown schematically in Figure 3.9 [69].

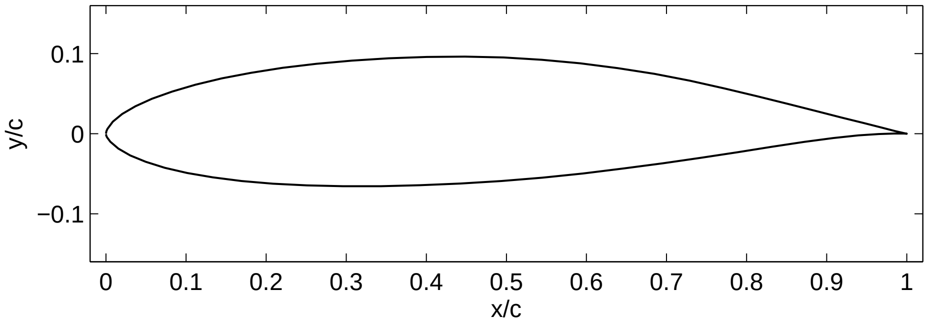

Figure 3.9: Non-dimensional schematic of the S822 airfoil

It was desirable to maximize the airfoil chord in order to attain the highest possible Reynolds number. The airfoil size was constrained only by blockage effects in the wind tunnel such that the frontal area blockage did not exceed 7.5% [9]. A chord length of 55 mm was chosen resulting in a blockage of 5.8% at $\alpha = 0°$, and 7.8% at $\alpha = 10°$. This chord length resulted in a maximum $Re_c = 1.15 \times 10^5$ with a maximum thickness of 8.9 mm.

The airfoil was machined from a single block of aluminum using a three-axis CNC mill. The milling process had a 0.025 mm tolerance. After milling, the surface was smoothed out using 1000 grit sandpaper. Using a micrometer, the trailing edge was measured to have a thickness of approximately 0.05 mm or less. The airfoil was attached to the test section on one side only by employing a steel spar. An existing angular adjustment device (constructed by McPhee [55]) that allowed for precise 1° increments was connected to the spar.

The section lift coefficient curves for the S822 at various Reynolds numbers from Selig and McGranahan [28] and Selig et al. [71] are shown in Figure 3.10. These measurements were made using a load balance. For the lower two Reynolds number cases the lift curves are non-linear at low angles of attack. They also have a negative lift coefficient at a zero angle of attack. This is more than likely due to a large laminar separation bubble on the airfoil or a separated flow that fails to reattach. For $Re_c = 2 \times 10^5$, the lift curve is linear for low angles of attack and has a positive lift coefficient for zero angle of attack.

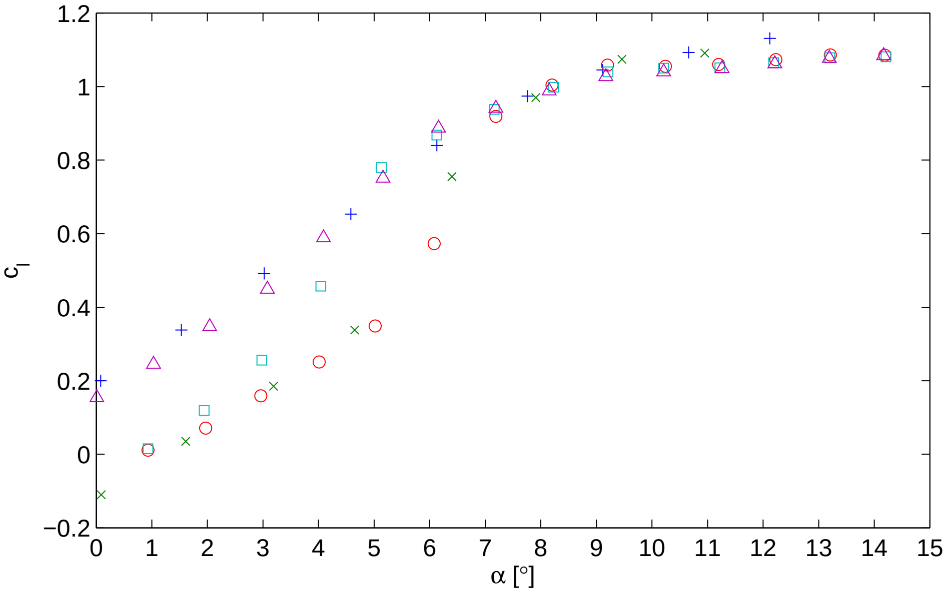

Figure 3.10: Section lift coefficient vs angle of attack for the S822; × $Re_c = 1.0 \times 10^5$ [71]; + $Re_c = 2.0 \times 10^5$ [71]; ∘ $Re_c = 1.0 \times 10^5$ [28]; □ $Re_c = 1.5 \times 10^5$ [28]; △ $Re_c = 2.0 \times 10^5$ [28]

The S822 lift to drag coefficient ratio for a given angle of attack at various Reynolds numbers is plotted in Figure 3.11. These data are also from Selig and McGranahan [28] and Selig et al. [71]. For all cases the lift to drag ratio increases with angle of attack, reaches a peak then decreases. In general, for a given angle of attack in the region below the peak, the lift to drag ratio increases with Reynolds number. The angle of attack at which the maximum lift to drag ratio occurs, decreases as the Reynolds number increases. At $Re_c = 1.5 \times 10^5$ the maximum lift to drag ratio occurs at approximately $\alpha = 8°$.

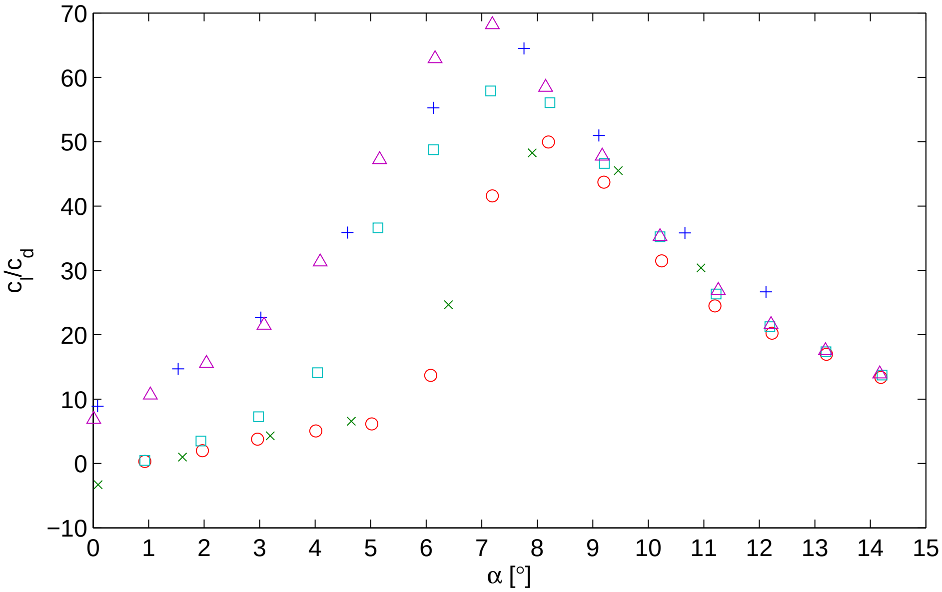

Figure 3.11: Lift to drag coefficient ratio vs angle of attack for the S822; × $Re_c = 1.0\times10^5$ [71]; + $Re_c = 2.0\times10^5$ [71]; ∘ $Re_c = 1.0\times10^5$ [28]; □ $Re_c = 1.5\times10^5$ [28]; △ $Re_c = 2.0\times10^5$ [28]

Oerlemans [52] investigated the acoustic emissions from six low Reynolds number wind turbine specific airfoils including the S822. These tests were performed with a 42 microphone phased array in an anechoic wind tunnel. In an open jet wind tunnel the physical angle of attack relative to the upstream flow velocity is different than the effective angle of attack relative to the unbounded local flow velocity. In this work α represents physical angle of attack and α_{eff} represents the effective angle of attack. A sample beam map from this work of S822 trailing edge noise is shown in Figure 3.12.

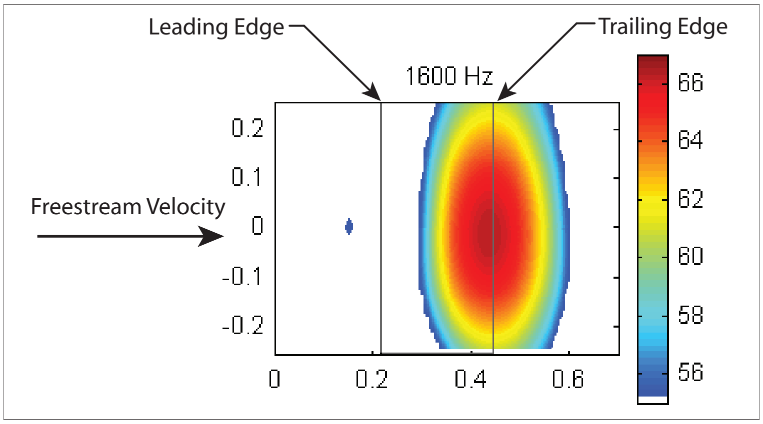

Figure 3.12: Trailing edge noise beam map of an S822 airfoil at a scan frequency of 1600 Hz from Figure 29 b) in Oerlemans [52]. Dimensions are in meters and the color bar is measured in decibels. $Re_c = 5.0 \times 10^5$ (U_∞ =32.0 m/s), $\alpha_{eff} = 7.9°$

Narrowband pure tones were not found for the S822 but rather a more broadband tone that increases in frequency with Reynolds number as shown in Figure 3.13. Additionally, the overall noise amplitude increases with Reynolds number.

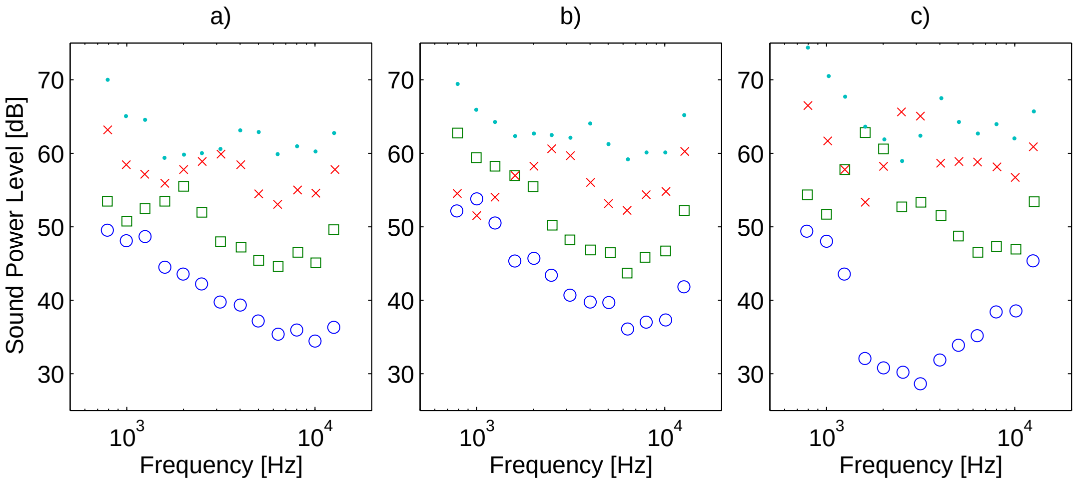

Figure 3.13: Acoustic spectra of S822 airfoil from Figure 22 in Oerlemans [52], a) $\alpha = 0.0°$ ($\alpha_{eff} = 0.0°$); b) $\alpha = 10.0°$ ($\alpha_{eff} = 4.4°$); c) $\alpha = 18.0°$ ($\alpha_{eff} = 7.9°$); $\circ$ $Re_c = 3.5 \times 10^5$; $\square$ $Re_c = 5.0 \times 10^5$; $\times$ $Re_c = 7.5 \times 10^5$; $\cdot$ $Re = 10^6$

3.3 Flow Visualization Setup

3.3.1 Smoke Wire Flow Visualization

The smoke wire flow visualization technique was employed at freestream velocities of 10, 15, 20, and 26 m/s in order to qualitatively assess the flow around the S822 airfoil. Tests were performed at both $\alpha = 0°$ and $\alpha = 8°$. For the experiments, a stainless steel wire with a diameter, d_{wire}, of 0.0762 mm, (0.003 inches) was used. It is recommended that the maximum Reynolds number based on wire diameter ($Re_{d_{wire}}$) be less than approximately 49 [25] to avoid vortex shedding from the wire. However at 26 m/s, $Re_{d_{wire}} \approx 130$ and good results were still obtained. The wire was strung through holes in the top and bottom of the test section and placed behind the airfoil touching the trailing edge for the majority of the tests. This placement allowed smoke to be entrained into the wake as well as into the separation bubble if reattachment did not occur. A few tests were conducted with the wire placed upstream of the airfoil in order to visualize the flow over the airfoil. Smoke was created from a fluid solution of approximately 70% glycerol in water. This fluid was found by Yarusevych et al. [25] to have the best results. A variable transformer was used to adjust the amount of current through the wire. Higher freestream velocities will result in a higher heat transfer through the wire requiring more current to evaporate the fluid. Yarusevych et al. [25] recommend the use of a scaling function that predicts the required voltage for a given freestream velocity. The transformer settings used ranged from 30–40% of full scale (120 V) for $U_0 = 10$–20 m/s. When heated, the wire elongated; therefore it was kept under tension with 10 g weight to keep it straight when the current was applied. However too much tension and the wire could have broken because it is much weaker when heated. To achieve regularly spaced streaklines the fluid was applied to the wire with one constant swiping motion using a cotton swab while the tunnel was off [25]. The fluid did not evenly coat the wire but rather formed into small beads along the wire. Once the fluid evaporated the wire rapidly heated up and would break if the current was not immediately shut off. Depending on the freestream velocity the smoke may only last a fraction of a second. Once the tunnel is turned on the fluid droplets will evaporate or be blown off shortly thereafter. Because of this, the test was performed immediately after the tunnel was turned on, especially at higher air speeds.

Two different photography setups were used to capture the smoke wire images. For the 10 and 15 m/s cases, a Nikon D70 digital SLR camera with a Nikkor 50 mm F/1.8 lens was used. This lens was chosen because it offers excellent sharpness with virtually no lens distortion [72]. Also, this lens has a large maximum aperture of 28 mm allowing for a large amount of light for each exposure. The camera was mounted on a tripod in front of the test section and positioned so the test section filled the frame as shown in Figure 3.14. The flow was illuminated with a Vivitar 285HV flash (triggered by the camera) mounted above the test section such that light was directed in plane with the smoke sheet. To prevent the flash from illuminating the back wall and the glass front panel, a black paper mask was placed on top of the test section to create a narrow band of light. The process for taking an image was to turn on the electricity and then immediately turn it off so the wire did not have time to overheat and break. As soon as the electricity was turned on the camera was triggered with a remote so as to not move the camera. Because the smoke was present for such a short period of time, timing the camera triggering to coincide with the smoke was extremely difficult. For the still images, the vortex shedding frequency, f_s was estimated with:

$$f_s = \frac{U_0}{s_v} \tag{3.3}$$

where s_v is the measured distance between subsequent vortices shed from the same side of the airfoil and U_0 is the mean freestream velocity. The convective velocity of the vortices was not known but was approximated by the mean freestream velocity.

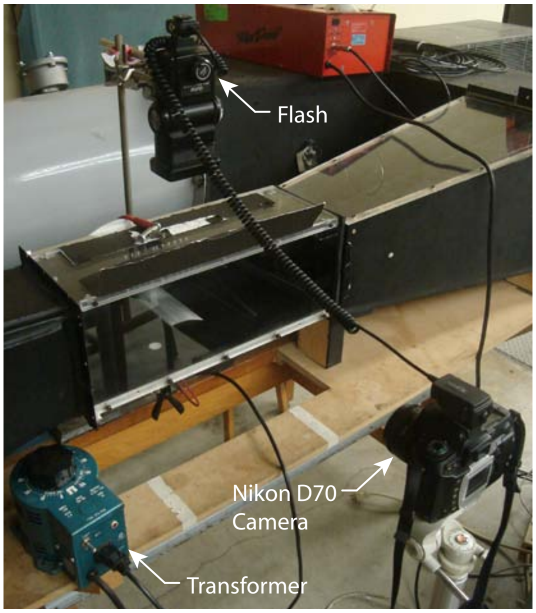

Figure 3.14: Smoke wire flow visualization setup with Nikon digital SLR camera

At the higher freestream velocities of 20 and 26 m/s the smoke was present for a even shorter period of time and because of this could not easily be photographed with a still camera. A Photron SA1.1 high speed video camera with a Nikkor 85 mm F/1.4 AI-s lens was used. This 85 mm lens is of higher quality than the 50 mm lens with a larger aperture [73]. This lens is incompatible with the Nikon D70 and therefore was not used for the still images. In order to capture the streaklines properly a frame rate of $f_{camera} = 5000$ fps was selected with a shutter speed of 1/5000 s. The camera was mounted in front of test section and positioned so the test section filled the frame; however a Diagnostic Instruments

SMS6B Boom Stand was used to support the camera because of the camera's weight. A 500 W halogen flood light pointed parallel with the smoke plane was used to illuminate the streaklines. A light masking setup similar to the one used for the still images was employed to create a narrow band of light. This setup is shown in Figure 3.15. The camera was started just before the electricity was momentarily turned on and approximately 1000 images were taken. Of the images taken only approximately 50 adequately showed the streaklines. For the high speed video of the flow, the vortex shedding frequency f_s was estimated with:

$$f_s = \frac{\triangle x_v f_{camera}}{s_v} \tag{3.4}$$

where $\triangle x_v$ is the average distance that each vortex moved between frames.

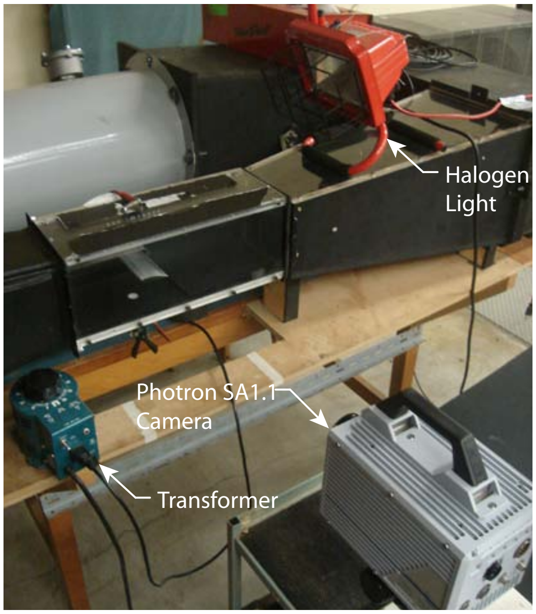

Figure 3.15: Smoke wire flow visualization setup with Photron SA1.1 camera

3.3.2 Oil Film Visualization

A mixture of mineral oil (Monarch #70) and graphite powder was used and a thin layer was spread over the airfoil surface. A method to spray the oil mixture onto the airfoil to replicate the experiment of Selig and McGranahan [28] was not available. Rather than remaining distributed over the entire airfoil, the oil accumulated in the laminar separation bubble region after the wind tunnel was turned on. It is believed that a higher viscosity fluid and a method to spray on the oil is needed to replicate the results of Selig and McGranahan [28]. Despite this, information about the bubble's size and position could still be inferred. The oil moved in unison with the separation bubble as the angle of attack or velocity changed. This allowed for the acquisition of images of the oil film visualization for every combination of angle of attack from 0°–10° and velocity from 15–35 m/s. Photos were taken with a Nikon D70 and a Nikkor 50 mm F/1.8 lens. Using the Diagnostic Instruments SMS6B Boom Stand the camera was positioned above the test section and pointed down towards the airfoil. Additional lighting was provided by a 500 W halogen light bulb positioned above and downstream of the airfoil. The process for taking the images was to start at 15 m/s, take an image for every angle from 0°–10° starting with 0° then incrementing the velocity by 1 m/s and repeating the photos for each angle.

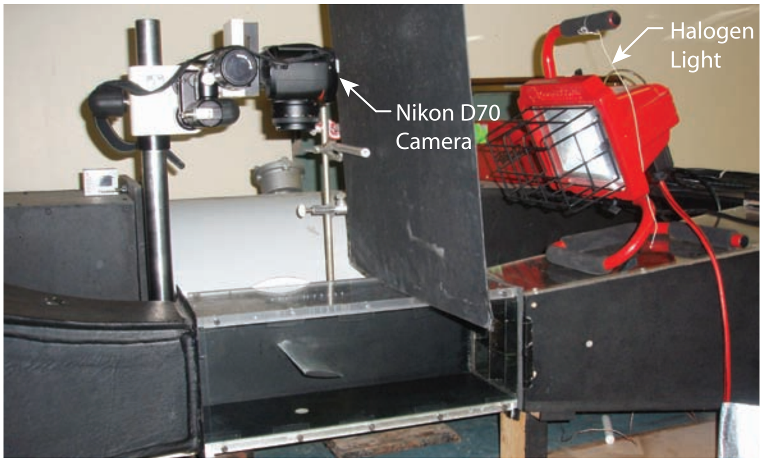

Figure 3.16: Oil film flow visualization setup

3.4 Laser Doppler Anemometry

3.4.1 System Description

A two component Dantec FiberFlow LDA system was used for the measurements. A Coherent Innova 70, 5 W Argon Ion laser was also used. A Dantec 60X41 transmitter contains a Bragg cell which splits the beam and shifts it by 40 MHz. The unshifted and shifted beams are each split into green, blue, and violet light with wavelengths of 514.5, 488, and 476.5 nm respectively, however only the green and blue beams are used. Here four 60X24 fibre manipulators connect the transmitter to each optical cable which allows for precise alignment of the beam. The probe used was a two component Dantec 60X81 with a 55X12 beam expander and a 310 mm 50X57 focal length lens. This probe operates in back scatter so the transmitting and receiving optics are in the same unit and visual access to the test section is only needed from one side. Individual translation adjustment of each beam was possible with this probe for more precise beam alignment. The smallest available focal length lens and beam expander were used to make the measurement volume as small as possible. The beam expander had an expansion ratio of 1.98 yielding a nominal beam separation of 76 mm. This resulted in the measurement volume dimensions listed below in Table 3.1 as estimated by the BSA Flow software where dz is the long axis of the measurement volume, and dx and dy are the two short axes.

Table 3.1: Measurement volume dimensions

	dx [mm]	dy [mm]	dz [mm]
Blue beam	0.073	0.072	0.59
Green beam	0.077	0.076	0.61

3.4.2 Physical Setup

The LDA probe was mounted to a three-axis traverse which allowed for the precise placement of the measurement volume inside the wind tunnel. The traverse could be positioned with an accuracy of approximately 0.0063 mm in the Z direction and 0.013 mm in the X and Y directions. A series of coordinates were programmed into the software and all measurements were taken automatically. The flow velocity in a wind tunnel is dominated by the freestream velocity where the transverse velocity is comparatively smaller. If the transverse velocity were to be measured directly the data rate would be significantly lower than if the freestream velocity were to be measured directly. This is because there are comparatively fewer seeding particles moving in the transverse direction. In order to acquire a high data rate for both velocity vectors the probe was rotated 45° degrees so that the magnitude of each velocity vector was approximately equal [31]. This is shown in Figure 3.17. A transformation was applied to the rotated velocity vectors in order to obtain the freestream and transverse velocity components which is shown below in Equation 3.5. The origin of the global coordinate system was located at the entrance of the test section where the bottom panel and back panel intersect as shown in Figure 3.17. This was the point at which it was easiest to align the probe's measurement volume to the test section.

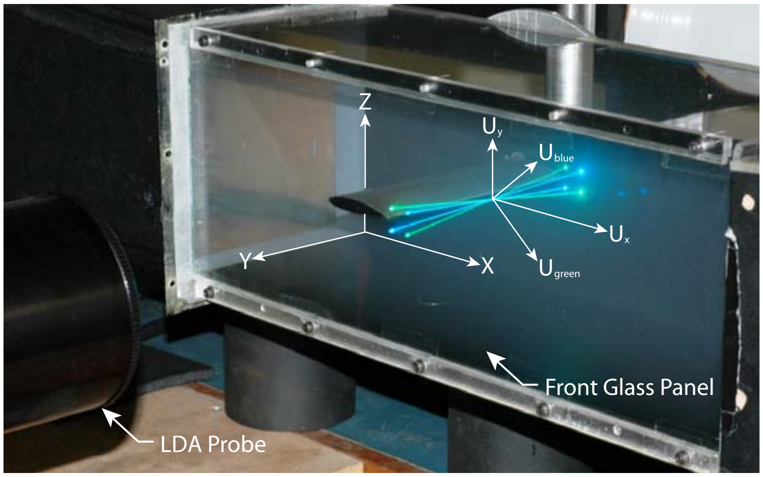

Figure 3.17: Rotated LDA probe and coordinate system

$$\begin{bmatrix} U_x \\ U_y \end{bmatrix} = \begin{bmatrix} \cos 45^\circ & \sin 45^\circ \\ -\sin 45^\circ & \cos 45^\circ \end{bmatrix} \begin{bmatrix} U_{blue} \\ U_{green} \end{bmatrix} \tag{3.5}$$

3.4.3 Seeding Particles

Two seeding particle generators were tested before the final experiments. Preliminary tests were conducted with a smoke wand which vaporizes mineral oil with a heated element. Although this produced adequately high data rates, the smoke wand could not produce a high enough volume rate of smoke. This increased experimentation time because extra time was required to fill the wind tunnel with smoke. Additionally, the smoke wand could not be controlled remotely. A Le Maitre Special Effects Inc., Red Devil smoke generator was ultimately used because it could quickly produce a large amount of smoke and had a remote control. This is a water based theatrical smoke generator shown in Figure 3.18. The smoke generator was connected to the wind tunnel via a flexible tube just upstream of the fan. A “T” connector was used to allow the condensed smoke fluid to collect in the sealed tube attached to the lower branch of the connector. Two types of smoke fluid were tried, 100A and CFC 300C both manufactured by Corona Integrated Technologies Inc. The 100A fluid produces larger particles and thus lasts considerably longer than the CFC 300C fluid. The 100A fluid also provided a high enough LDA data rate.

Figure 3.18: Red Devil smoke generator connected to the wind tunnel

There was a concern that if there was too much smoke in the wind tunnel it would condense on the turbulence reduction screens and clog them. This would constrict the flow and lower the freestream velocity for a given VFD setting. This was investigated by injecting smoke into the tunnel continuously for seven seconds and measuring the freestream velocity over a period of ten minutes. There was no measurable decrease in freestream velocity over this time. However as a preventative measure, cleaning of the screens through the cleaning window in the screen box was performed after every few tests. It was also found that immediately after the smoke was injected the turbulence intensity increased. A plot of turbulence intensity vs time is shown in Figure 3.19 for the period of time immediately after continuous smoke injection for seven seconds. After approximately eight minutes, the turbulence intensity reached normal levels. However the data rate also decreased with time, therefore if a high data rate was needed it was not possible to wait until the turbulence intensity stabilized. Whenever possible measurements were performed a short period of time after smoke injection and smoke was injected sparingly.

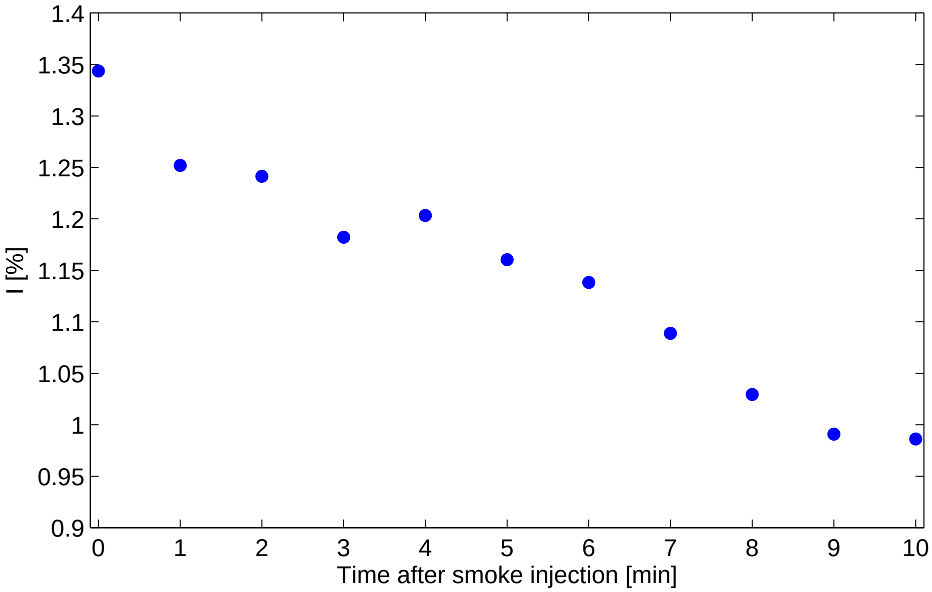

Figure 3.19: Decrease in turbulence intensity over time after injection of smoke

3.4.4 LDA Tests

All LDA measurements were taken on the mid-span plane around the airfoil. Single location LDA experiments were performed over a Reynolds number range of 5.24×10^4–11.5×10^4 ($U_0 = 15$–35 m/s) at $\alpha = 0°$ and $\alpha = 8°$. These angles of attack were chosen to replicate the test conditions of Oerlemans [52]. Also, $\alpha = 8°$ corresponds to the approximate maximum lift to drag ratio for the S822 airfoil. This velocity range was chosen so that both the 3×10^4–7×10^4, and 7×10^4–20×10^4 Reynolds number regimes could be studied. The specific measurement location was at $x/c = 1.13$ (where $x/c = 1$ is the trailing edge) and a y/c position corresponding to the maximum RMS value of the freestream velocity. The $x/c = 1.13$ location corresponds to the closest point to the airfoil where a profile could be measured without the laser beams hitting the airfoil. For each velocity and angle of attack case, three sets of measurements were taken each comprising of approximately 3.1×10^5 data points recorded at approximately 20–30 kHz. Higher sampling rates were possible at lower freestream velocities. The BSA Flow software calculated a power spectrum with a maximum frequency of 6125 Hz and a FFT size of 8192 data points resulting in a frequency resolution of 0.75 Hz. The maximum frequency and FFT size were chosen to achieve a frequency resolution equal to that of the acoustic spectrum (discussed in Subsection 3.5.1). An averaged FFT was created from the three data sets for each measurement case. A Hanning filter with a filter width of 0.1 [32] was applied to the spectra to smooth out high frequency noise.

Additional measurements were performed in both regimes at $Re_c = 6.91 \times 10^4$ and $Re_c = 10.0 \times 10^4$ ($U_0 = 20$ m/s and $U_0 = 30$ m/s) where the LDA was used to measure wake profiles at $\alpha = 0°$ and $\alpha = 8°$. For each combination of velocity and angle of attack a profile was taken at x/c locations of 1.13, 1.25, 1.5, 2, and 3. At each measurement location approximately 7.7×10^5 data points were recorded at a sampling rate of approximately 3–6 kHz. Wake profiles were measured to determine the location of the maximum RMS freestream velocity in the wake. This was needed so that the measurement volume could be at this location for the single point LDA measurements. Additionally, the wake profiles were measured to determine the separation between freestream velocity RMS peaks, denoted as d^*.

3.5 Acoustic Measurement Tools

3.5.1 Brüel and Kjær Microphone

The wind tunnel background noise and airfoil noise measurements were performed with a Brüel and Kjær (B&K) 4192 microphone. The microphone setup and LabVIEW program used to acquire the data were the exact ones used by McPhee [55]. The microphone was a 12.7 mm diameter microphone with a frequency range from 3–20000 Hz and a dynamic range of 20.7–161 dB. The frequency response was flat from 100–15000 Hz. The microphone signal was fed into a B&K preamplifier, model 2669-C with a single channel conditioning amplifier, model 2690-A-0S1. The preamplifier output was connected to a National Instruments PCI-6143 data acquisition card that has a 16 bit analog-to-digital converter (96 dB dynamics range) with an input voltage of ±5 V. This yields a voltage resolution of 0.153 mV. Additionally, this system is capable of a sampling rate of 250 kHz.

The microphone was recess mounted behind a Dacron® fabric membrane in the bottom wall of the test section, 150 mm downstream of the test section inlet. Recess mounting the microphone reduces the boundary layer noise over the microphone. The setup is shown below in Figure 3.20. The microphone was positioned on the pressure side of the airfoil such that it was in a high amplitude region of the trailing edge dipole directivity as shown in Figure 2.12 in Section 2.5.

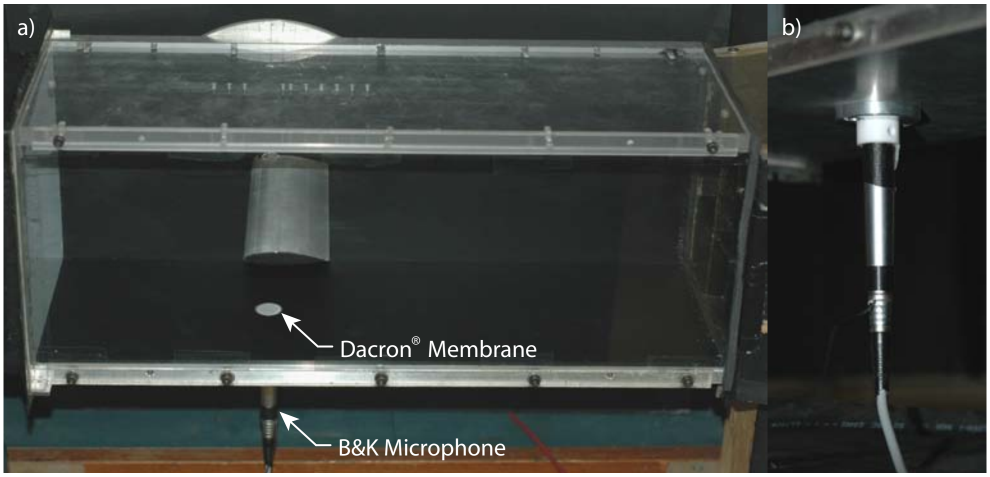

Figure 3.20: Brüel and Kjær 4192 microphone mounted inside the test section, a) view from in front of the test section; b) view from underneath the test section

Microphone measurements were performed at the same time as the single point LDA measurements as well as with an empty test section in order to measure the background noise levels. For each configuration of freestream velocity and angle of attack, 2.45×10^6 data points were collected at a sampling rate of 24500 Hz (as recommended by McPhee [55]). The data processing code from McPhee [55] was used which divides the data into 100 blocks, so an FFT can be performed on each to produce a final averaged FFT. The resulting FFT had a frequency resolution of 0.75 Hz.

3.5.2 Microphone Phased Array

3.5.2.1 Microphone Array Design

Typically microphone phased arrays used for research employ costly condenser microphones [45]. Recently some researchers have used inexpensive electret microphones with great success [74, 75]. Another type of inexpensive microphone is the Micro Electro-Mechanical System (MEMS) microphone which was successfully used by Humphreys et al. [44] to measure airframe noise. MEMS microphones are inexpensive, compact, and can have built in noise filtering and amplification circuitry. For these reasons MEMS microphones were chosen to be used for the microphone phased array. Specifically Knowles Acoustics type SPM0408LE5H microphones were used which feature a built in amplifier with adjustable gain and built in RF protection circuitry. Each microphone measures 4.7 mm × 3.8 mm with a thickness of 1.3 mm and is designed to be surface mounted to a circuit board. The microphones are bottom ported meaning sound must travel through an opening in the circuit board before reaching the microphone's diaphragm.

Microphone phased array design is based on the type of measurements that need to be performed, as well as the project's budget. The desired frequency range to be measured and the distance from the source to the array play the most important role in the array design. Having more microphones will always improve the signal-to-noise ratio however there is a balance between cost (ie. number of microphones) and quality of results. Much research has been done on the optimal microphone layout. A well accepted design rule is to arrange the microphones in such a way that there are no duplicate vector spacings between microphones [47]. It is therefore disadvantageous to arrange the microphones in a cartesian grid or in a circle with an even number of microphones. The most common arrangement to ensure unique microphone vector spacings is a logarithmic spiral. Both Dougherty [76] and Underbrink [77] have patents for spiral array layouts. Underbrink's "Equal Area Aperture Array" layout has multiple spirals, an improvement over the single Dougherty spiral [47]. Additionally the Underbrink array is laid out such that the area around each microphone is equal, providing a more equal microphone weighting. The inter-microphone spacing and overall size of the array are also important design parameters to consider. The smallest microphone spacing dictates the highest measurable frequency. To avoid "spatial aliasing" the smallest inter-microphone spacing must not be larger than half the wavelength of the highest frequency to be measured [47]. The aperture dictates the degree to which low frequency sources can be resolved. A larger aperture array will permit better resolution of low frequencies.

The array used in this thesis was designed by Bale [78] and is composed of three logarithmic spirals each with nine microphones for a total of 27 microphones. The Underbrink "Equal Area Aperture Array" [77] layout was used. The array was designed to make measurements in the 152.4 mm × 152.4 mm cross section wind tunnel and therefore has an aperture of 141 mm. All microphones and supporting components (ie, resistors, capacitors, and connectors) were surface mounted to a single printed circuit measuring 203.2 mm × 152.4 mm. The microphone signals were recorded with National Instruments 9237 modules each attached to a National Instruments cDAQ-9172 chassis. The NI-9172 modules have 24 bit analog-to-digital converters (144 dB dynamics range) with an input voltage of ±250 mV, yielding a resolution of 0.03 mV. This data acquisition system is capable of simultaneous sampling at 50 kHz over all channels.

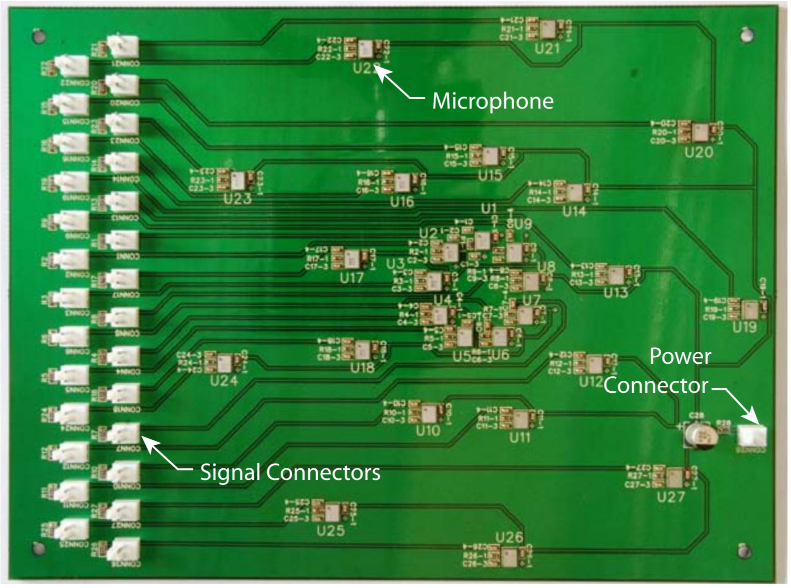

Figure 3.21: Microphone phased array circuit board

3.5.2.2 Microphone Array Testing

The microphone mounting structure will affect the results and is an important matter to consider. If microphones are flush mounted to a surface a pressure doubling will occur at the surface which must be removed prior to beamforming [79], as is the case for this array. Microphones can be mounted protruding from a support structure to avoid this problem. In the case of array measurements in a hard wall wind tunnel, it is often simplest to flush mount the microphones. However with this arrangement each microphone will be subjected to boundary layer noise which can saturate the microphone amplifier. Since the boundary layer noise is incoherent between microphones it is attenuated with the removal of the CSM's diagonal. Jaeger et al. [80] found that boundary layer noise can be avoided and results improved by recessing the microphones behind a stretched Kevlar® membrane flush with the wind tunnel wall. Kevlar® has a very high tensile strength allowing the membrane to be stretched very taut providing a solid boundary. Jaeger et al. found that Kevlar® 120, (1.8 oz/yd^2, 61 g/m^2) provided excellent acoustic permeability. Remillieux et al. [11] constructed a test section with Kevlar® membrane walls at the Virginia Tech Stability Wind Tunnel and successfully performed aeroacoustic tests. Attempts were made to fabricate a Kevlar® membrane for the wind tunnel used in this work, however a satisfactory design was not found. Due to time constraints this matter was not investigated further and as a result no satisfactory beamforming tests were performed on the airfoil inside the wind tunnel.

Preliminary tests with the microphone array were performed in order to determine if the beamforming code worked for real signals and if the array worked physically. Tests were performed with a single monopole source in a stationary flow field located a known distance away from the array along the centreline. The monopole source was created by affixing a 370 mm long aluminum tube with a 12.7 mm inner diameter to a B&C DE10 compression driver. This method of creating a monopole source is recommended by Arnold [81]. Tests were performed for source pure tone frequencies of 3, 5 and 7 kHz each with an array-to-source separation of 164 and 385 mm. These pure tones were created by an Agilent 33220A Function Generator outputting a sine wave directly to the compression driver. This setup is shown in Figure 3.22. The array was mounted to an acrylic plate using metal standoffs which was then fixed to a tripod allowing for three-dimensional positioning. A total of 409600 data points (50 blocks of 8192 data points) were recorded for each channel at a sampling rate of 50 kHz. This resulted in a frequency resolution of 6.1 Hz. A Hamming window was applied to each block of data before being transformed into the frequency domain with a FFT. The beamforming process described in Section 2.6 and in Appendix D was used to process the signals into source maps.

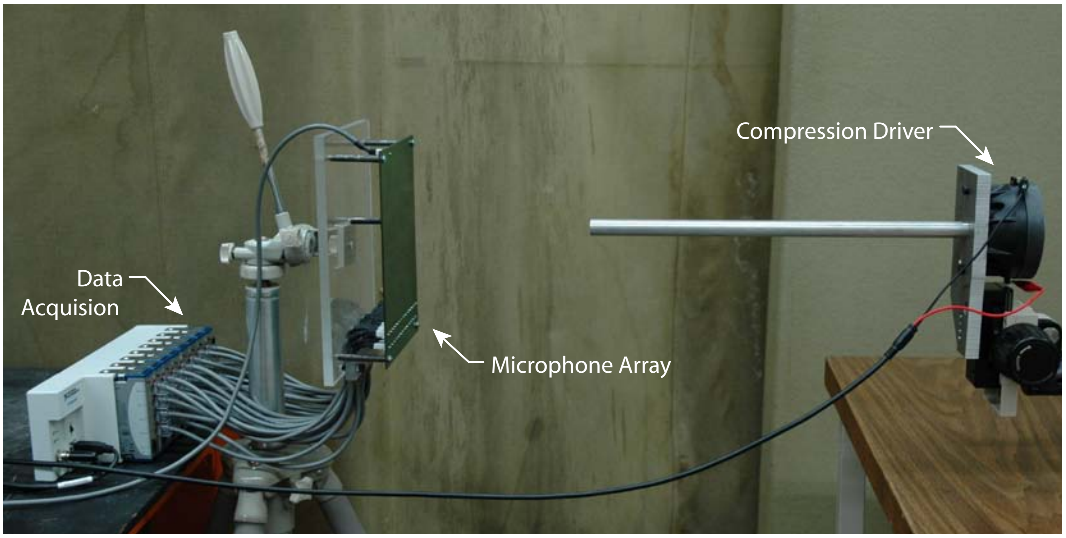

Figure 3.22: Setup for preliminary microphone array testing

Chapter 4

Results and Discussion

4.1 Experimental Plan

Several types of measurements were conducted and the results are presented in this chapter. A detailed table of each type of measurement and the velocity and angle of attack at which it was performed is shown in Table 4.1. To assess the relationship between the velocity spectra and acoustic spectra, a LDA measurement at a single location in the wake was performed in conjunction with a microphone measurement. Although it would have been beneficial to acquire the microphone and LDA data simultaneously, such that a LDA reading and a microphone reading had the same time stamp, this was not possible due to instrumentation limitations. However the microphone and LDA measurements were performed at the same time so that the operating conditions were the same. Single location LDA and microphone experiments were performed over a Reynolds number range of 5.24×10^4–11.5×10^4 ($U_0 = 15$–35 m/s) at $\alpha = 0°$ and $\alpha = 8°$. The LDA was also used to measure wake profiles at $Re_c = 6.91 \times 10^4$ and $Re_c = 10.0 \times 10^4$ ($U_0 = 20$ m/s and $U_0 = 30$ m/s) for $\alpha = 0°$ and $\alpha = 8°$. Smoke wire visualizations were performed at 10, 15, 20, and 26 m/s at $\alpha = 0°$, and 10 m/s, and 15 m/s at $\alpha = 8°$. Surface flow visualization images were taken at all combinations of velocity from 15–35 m/s and angles of attack from 0°–10°. The values of U_0 are nominal values measured with an empty test section. Blockage corrections are taken into account when Re_c and St_{d^*} are calculated. The details of the blockage corrections are outlined in Appendix B.

Table 4.1: Experimental measurement matrix, × Single location LDA and microphone; ⋆ LDA wake profiles; ∘ Surface flow visualization; ⊗ Smoke wire visualization

U_0 [m/s]		10	15	16	17	18	19	20	21	22	23	24
$Re_c \times 10^{-4}$		3.5	5.1	5.5	5.8	6.1	6.4	6.8	7.1	7.4	7.7	8.0
α [°]	0	⊗	× ∘ ⊗	×∘	×∘	×∘	×∘	× ⋆ ∘⊗	×∘	×∘	×∘	×∘
	1		∘	∘	∘	∘	∘	×∘	∘	∘	∘	∘
	2		∘	∘	∘	∘	∘	×∘	∘	∘	∘	∘
	3		∘	∘	∘	∘	∘	×∘	∘	∘	∘	∘
	4		∘	∘	∘	∘	∘	×∘	∘	∘	∘	∘
	5		∘	∘	∘	∘	∘	×∘	∘	∘	∘	∘
	6		∘	∘	∘	∘	∘	×∘	∘	∘	∘	∘
	7		∘	∘	∘	∘	∘	×∘	∘	∘	∘	∘
	8	⊗	× ∘ ⊗	×∘	×∘	×∘	×∘	× ⋆ ∘	×∘	×∘	×∘	×∘
	9		∘	∘	∘	∘	∘	×∘	∘	∘	∘	∘
	10		∘	∘	∘	∘	∘	×∘	∘	∘	∘	∘

U_0 [m/s]		25	26	27	28	29	30	31	32	33	34	35
$Re_c \times 10^{-4}$		8.4	8.7	8.9	9.2	9.5	9.8	10.1	10.4	10.8	11.0	11.3
α [°]	0	×∘	× ∘ ⊗	×∘	×∘	×∘	× ⋆ ∘	×∘	×∘	×∘	×∘	×∘
	1	∘	∘	∘	∘	∘	×∘	∘	∘	∘	∘	∘
	2	∘	∘	∘	∘	∘	×∘	∘	∘	∘	∘	∘
	3	∘	∘	∘	∘	∘	×∘	∘	∘	∘	∘	∘
	4	∘	∘	∘	∘	∘	×∘	∘	∘	∘	∘	∘
	5	∘	∘	∘	∘	∘	×∘	∘	∘	∘	∘	∘
	6	∘	∘	∘	∘	∘	×∘	∘	∘	∘	∘	∘
	7	∘	∘	∘	∘	∘	×∘	∘	∘	∘	∘	∘
	8	×∘	×∘	×∘	×∘	×∘	× ⋆ ∘	×∘	×∘	×∘	×∘	×∘
	9	∘	∘	∘	∘	∘	×∘	∘	∘	∘	∘	∘
	10	∘	∘	∘	∘	∘	×∘	∘	∘	∘	∘	∘

4.2 Flow Visualization Results

4.2.1 Smoke Wire Visualization

The smoke wire flow visualization method was used to obtain information about the airfoil's wake. For $\alpha = 0°$, the airfoil wake is shown at $Re_c = 3.5 \times 10^4$ ($U_0 = 10$ m/s) in Figure 4.1 a) and at $Re_c = 5.1 \times 10^4$ ($U_0 = 15$ m/s) in Figure 4.1 b). For both cases the smoke is being entrained into the separation bubble on the suction side making it visible. The presence of the separation bubble without reattachment is expected at these low Reynolds

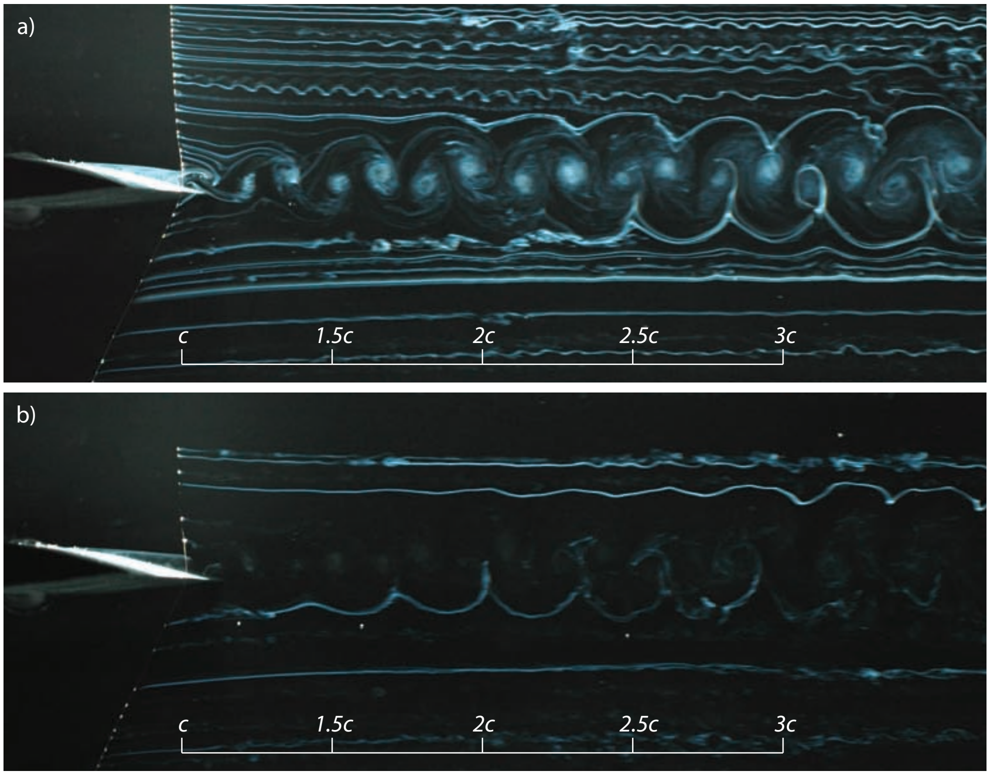

Figure 4.1: Smoke wire flow visualization at $\alpha = 0°$ for a) $Re_c = 3.5 \times 10^4$ ($U_0 = 10$ m/s); b) $Re_c = 5.1 \times 10^4$ ($U_0 = 15$ m/s)

numbers. The Kármán vortex streets of alternating vortices are clearly visible in the airfoil wake for both cases. The vortex streets are very definitive and the vortex spacing is highly regular. For $Re_c = 3.5 \times 10^4$, $\alpha = 0°$ the vortex shedding frequency is approximately 580 Hz and is approximately 870 Hz for the $Re_c = 5.1 \times 10^4$, $\alpha = 0°$ case. There appears to be little influence of vortex shedding from the wire on the airfoil's Kármán vortex street and separation bubble at these freestream velocities. The majority of the streaklines above and below the Kármán vortex street are relatively straight and do not reveal any vortex shedding from the wire.

Smoke wire flow visualization tests were performed at $\alpha = 8°$. The $Re_c = 3.5 \times 10^4$ results are shown in Figure 4.2 a) and the $Re_c = 5.1 \times 10^4$ results are shown in Figure 4.2 b). For the $Re_c = 3.5 \times 10^4$, $\alpha = 8°$ case the smoke is entrained into the separation bubble from the trailing edge showing that reattachment does not occur. Had reattachment occurred, the smoke created at the trailing edge would not have been carried upstream. Also from the images, the separation bubble is seen to be larger in size compared to the same Reynolds number at $\alpha = 0°$. The $Re_c = 5.1 \times 10^4$, $\alpha = 8°$ case reveals a much different flow where the smoke does not appear to be entrained into the separation bubble

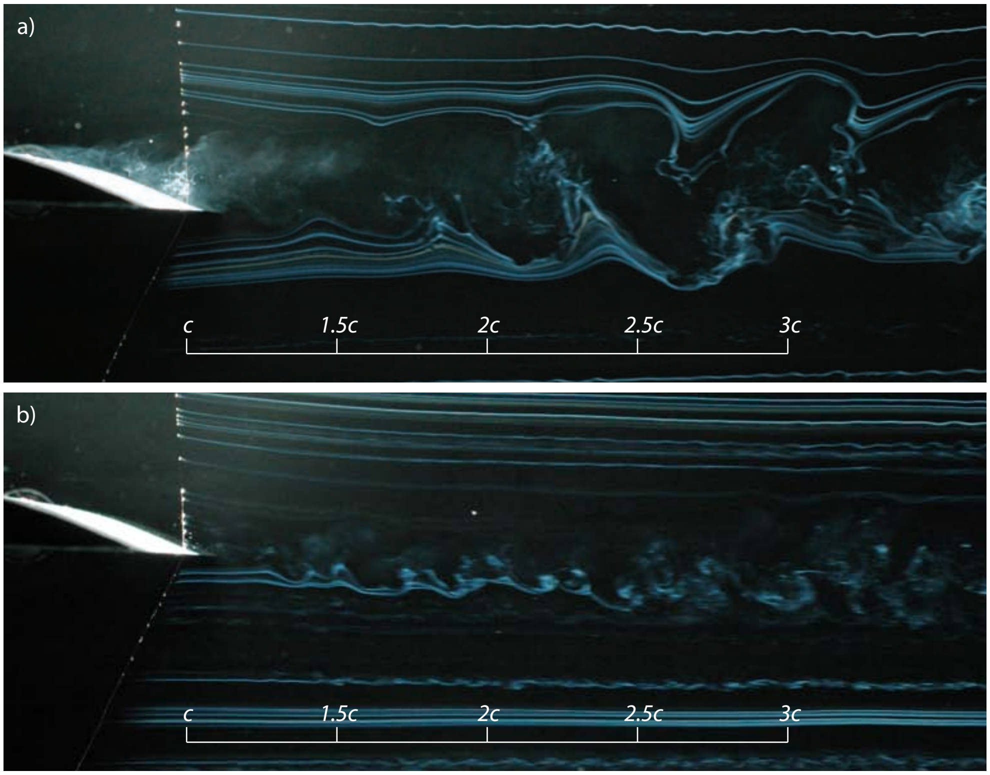

Figure 4.2: Smoke wire flow visualization at $\alpha = 8°$ for a) $Re_c = 3.5 \times 10^4$ ($U_0 = 10$ m/s); b) $Re_c = 5.1 \times 10^4$ ($U_0 = 15$ m/s)

suggesting flow reattachment. This was further investigated by placing the smoke wire upstream of the airfoil. Shown in Figure 4.3 are the smoke streaklines from the upstream wire that show the flow reattaching to the airfoil. Flow reattachment corresponds to an increase in the ratio of lift to drag [21]. Since the $Re_c = 5.1 \times 10^4$, $\alpha = 8°$ case has flow reattachment compared to the $Re_c = 3.5 \times 10^4$, $\alpha = 8°$ case with no reattachment, it must have a higher ratio of lift to drag. This increase in lift to drag ratio with increasing Reynolds number is also shown in the S822 lift to drag coefficient curves from in Figure 3.11 in Section 3.2. A Kármán vortex street was present for the $Re_c = 3.5 \times 10^4$, $\alpha = 8°$ case where $f_s \approx 340$ Hz. However for the $Re_c = 5.1 \times 10^4$, $\alpha = 8°$ case, the vortical structure is not as visible as in the $Re_c = 3.5 \times 10^4$, $\alpha = 8°$ case. The vortex street can only been seen in Figure 4.3 where $f_s \approx 700$ Hz.

A different smoke wire method was used to acquire images at higher Reynolds numbers. A Photron SA1.1 high speed video camera was used since all the smoke evaporates very quickly making it difficult to capture the smoke with a single photograph. Smoke wire images from this camera are shown in Figure 4.4 at Reynolds numbers of 6.8×10^4 ($U_0 = 20$ m/s) and 8.7×10^4 ($U_0 = 26$ m/s), both at $\alpha = 0°$. At these higher velocities the smoke

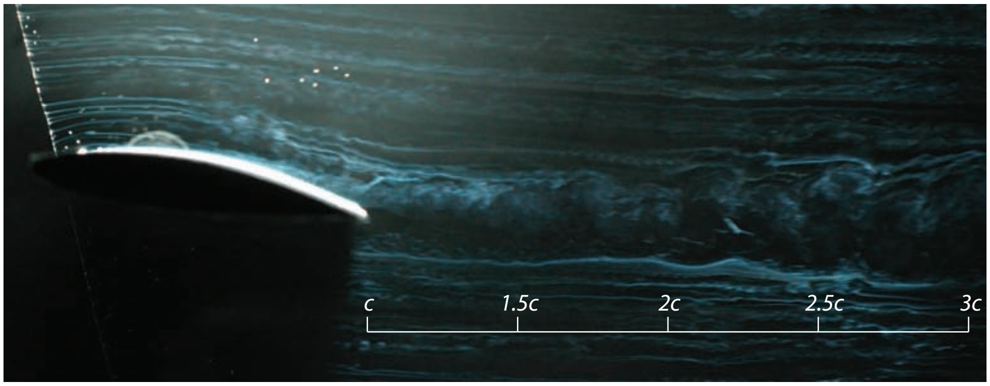

Figure 4.3: Upstream smoke wire flow visualization at $\alpha = 8°$ for $Re_c = 5.1 \times 10^4$ ($U_0 = 15$ m/s)

was very diffuse and the image quality was not as good as at lower velocities. Although not clearly visible in the still image, for the $Re_c = 6.8 \times 10^4$, $\alpha = 0°$ case shown in Figure 4.4 a), the smoke can be seen to entrain into the separation bubble in the series of images obtained from the high speed video. The flow is not expected to reattach at this low Reynolds number. At the slightly higher Reynolds number of 8.7×10^4, the flow does reattach. This is known since the smoke does not entrain into the separation bubble and move upstream. However this is only clearly visible in the sequence of images and not clearly visible in Figure 4.4 b). The Kármán vortex street is visible in both cases, however they are not as well defined and the vortex separation not as regularly spaced as in the two lower Reynolds number cases at $\alpha = 0°$. The vortex shedding frequency was estimated at 1100 Hz and for the $Re_c = 6.8 \times 10^4$, $\alpha = 0°$ case and 1250 Hz for the $Re_c = 8.7 \times 10^4$, $\alpha = 0°$ case. For these two higher velocity cases there is an increased risk that the vortex shedding from the wire will affect the flow. However, similar to the lower velocity cases, the streaklines away from the Kármán vortex street are relatively straight and no significant vortex shedding from the wire was observed.

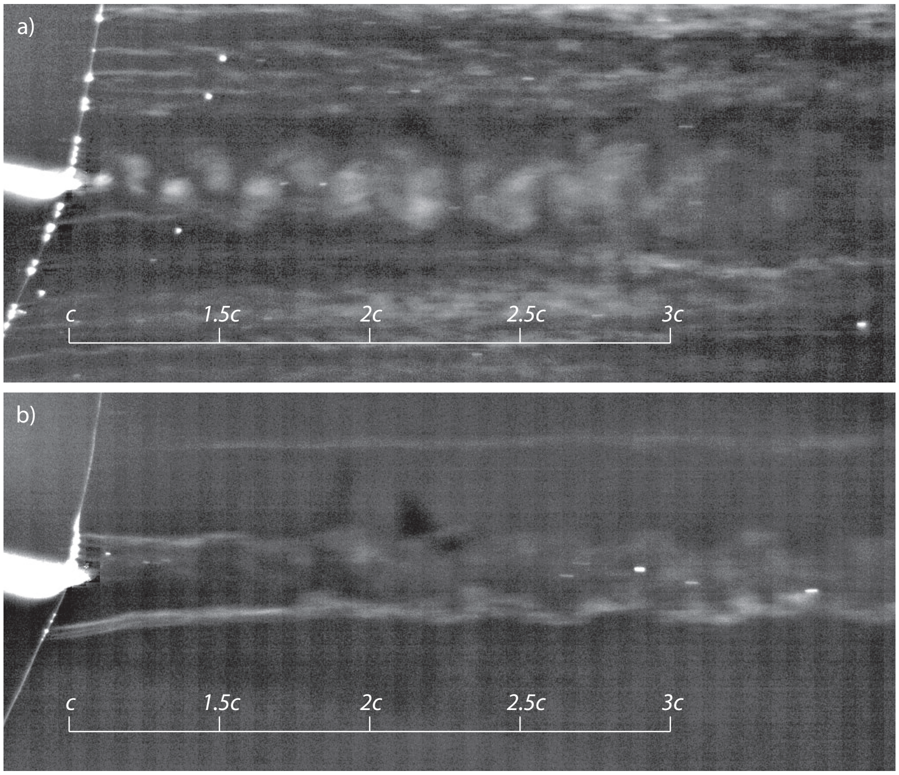

Figure 4.4: Smoke wire flow visualization at $\alpha = 0°$ for a) $Re_c = 6.8 \times 10^4$ ($U_0 = 20$ m/s); b) $Re_c = 8.7 \times 10^4$ ($U_0 = 26$ m/s)

4.2.2 Oil Film Visualization

The oil film visualization technique was employed to gain insight into the boundary layer development on the suction side of the airfoil. Images were taken for every combination of freestream velocity from 15–35 m/s and angle of attack from 0°–10° for a total of 231 images. Shown in Figure 4.5 is a sample image taken at $Re_c = 9.5 \times 10^4$ ($U_0 = 29$ m/s) and $\alpha = 3°$ where the flow is from top to bottom. The laminar separation bubble is bounded by the two lines of oil parallel to the leading edge, here called the separation oil line and the reattachment oil line. Selig and McGranahan [28] report that the actual separation point was slightly upstream of the separation oil line and the actual reattachment point was slightly downstream of the reattachment oil line. For the majority of the images the separation oil line was faint since the flow pushes the majority of the oil downstream. From this image the two-dimensionality of the flow is also visible since the oil lines are nearly parallel to the leading edge for the spanwise extent of the airfoil. All surface flow visualization images are shown in an array in Figures 4.6 and 4.7. The angle of attack is incremented in the images from bottom to top and the velocity is incremented in the

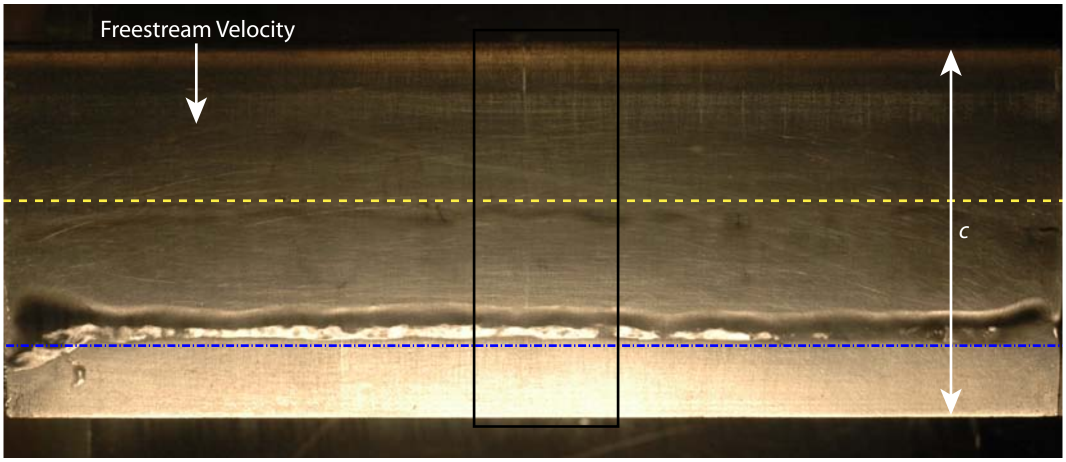

Figure 4.5: Top view of the airfoil's suction side showing oil film surface flow visualization, $Re_c = 9.5 \times 10^4$ ($U_0 = 26$ m/s), $\alpha = 3°$, – – – separation oil line; –·– reattachment oil line; —— cropped area for Figures 4.6 and 4.7

images from left to right. For angles of attack from 0°–6° the separation bubble can be seen to decrease in size and move slightly towards the leading edge as the Reynolds number increases. This is analogous to the findings of Nakano et al. [16, 17] and Gerakopulos et al. [22] where the separation bubble on the suction side of a NACA 0018 airfoil decreased in size and moved upstream as the angle of attack increased. For small angles of attack, the flow does not reattach to the airfoil until $Re_c \approx 8 \times 10^4$ ($U_0 \approx 23$ m/s). This is consistent with reports by Lissaman [20] and Carmichael [21] that at this Reynolds number the airfoil chord is long enough for reattachment to occur. Flow reattachment is visible when the reattachment oil line moves away from the trailing edge. Both the surface flow and smoke wire visualizations show no flow reattachment at $Re_c = 6.8 \times 10^4$ ($U_0 = 20$ m/s) and flow reattachment at $Re_c = 8.7 \times 10^4$ ($U_0 = 26$ m/s). As the Reynolds number increases the separation bubble is seen to decrease in size and move upstream. This phenomenon was also measured by Gerakopulos et al. [22]. With increasing Reynolds number the boundary layer transitions to turbulent farther upstream, which causes reattachment to take place farther upstream. This is the cause for the decrease in separation bubble size with increasing Reynolds number.

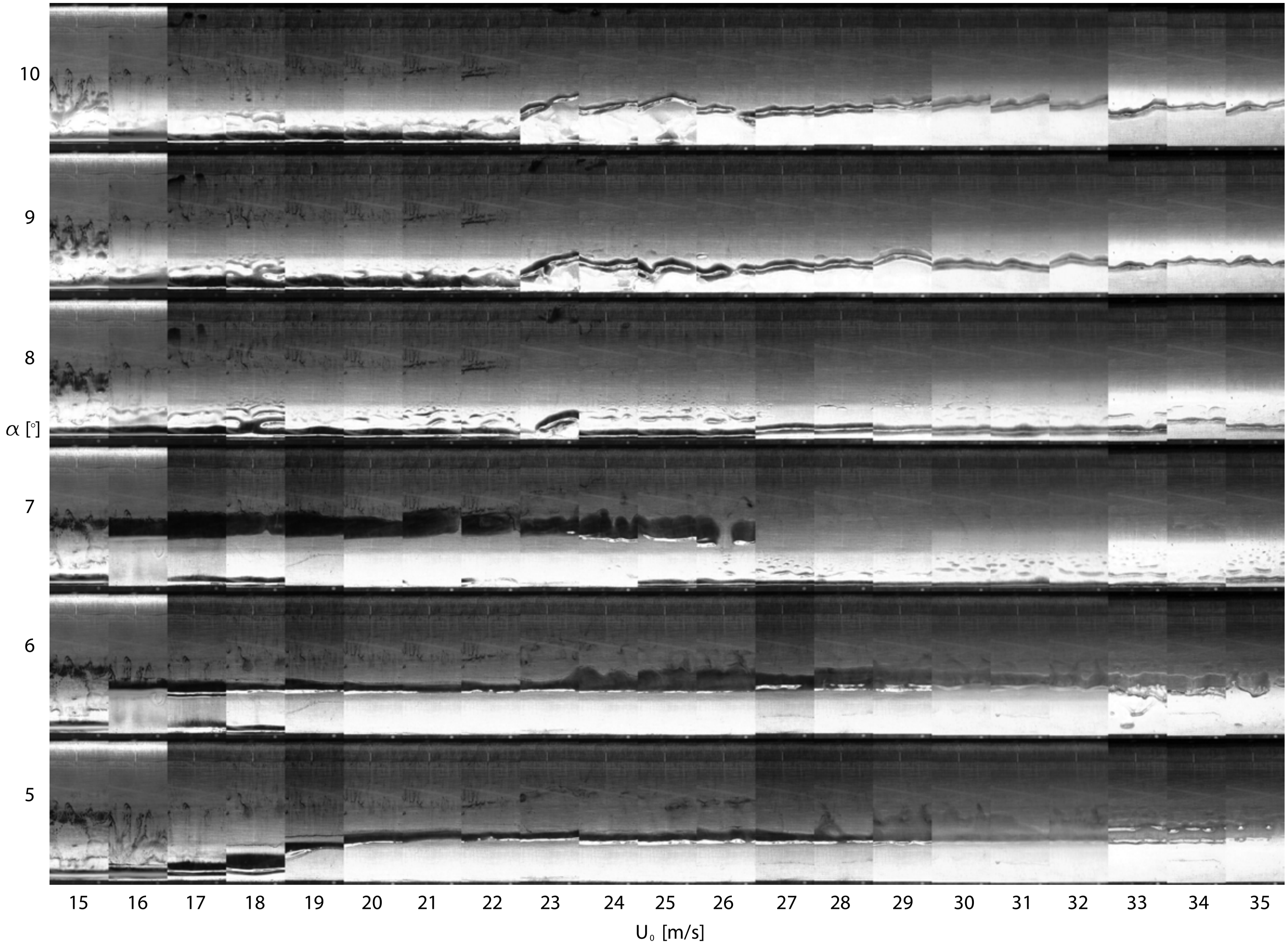

Figure 4.6: All oil film surface flow visualization images for angles of attack from 5°–10°

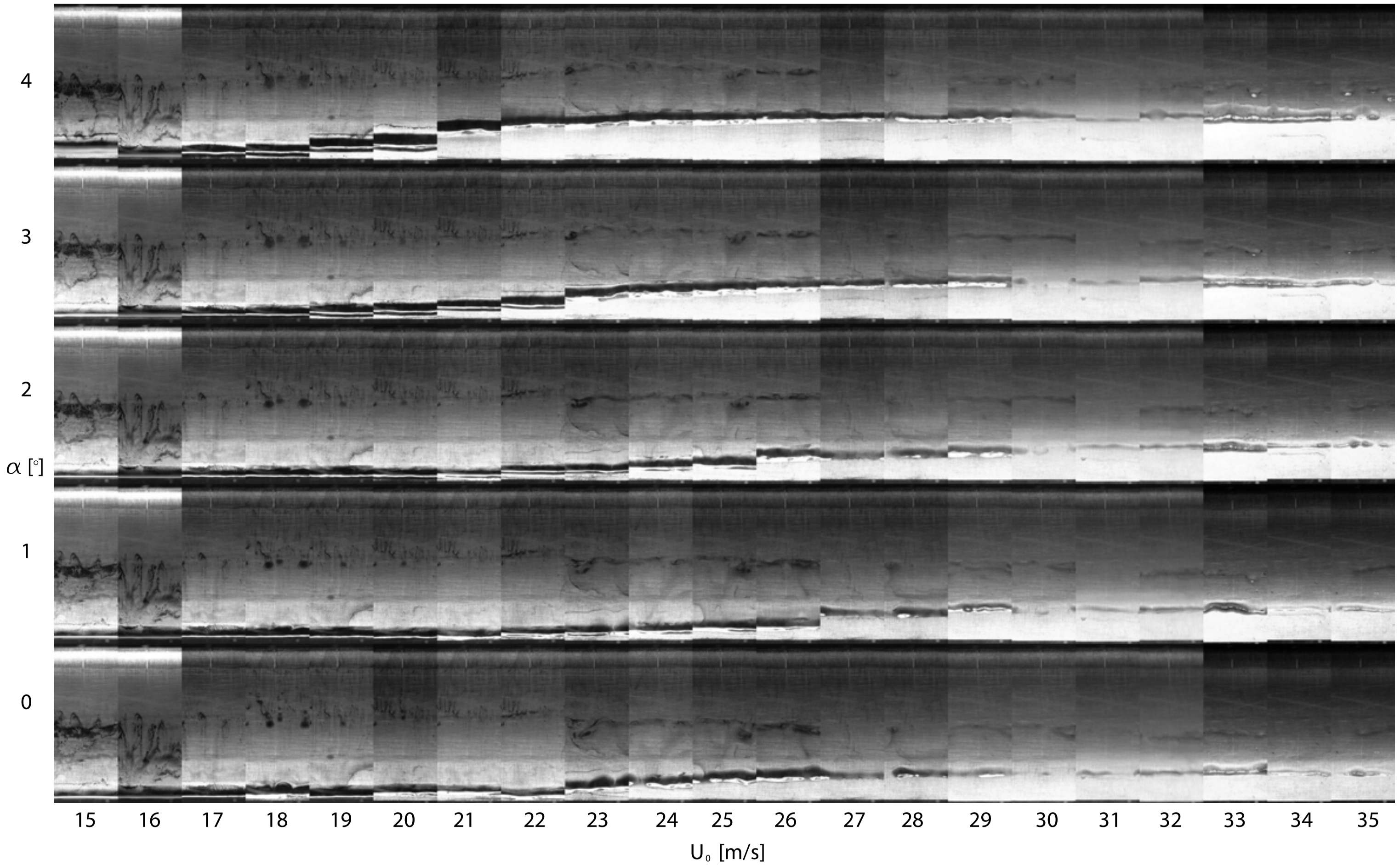

Figure 4.7: All oil film surface flow visualization images for angles of attack from 0°–4°

4.3 Velocity Results

4.3.1 Wake Profiles

Wake profiles were measured at $Re_c = 6.8 \times 10^4$ and $Re_c = 9.8 \times 10^4$ ($U_0 = 20$ m/s and $U_0 = 30$ m/s) each at $\alpha = 0°$ and $\alpha = 8°$. Using the LDA, measurements were taken at distances from the leading edge of $x/c = 1.13$, 1.25, 1.5, 2, and 3. Data points were separated by 0.5 mm in the velocity deficit region and by 2 mm outside this region. In Figure 4.8, the normalized RMS freestream velocity wake profiles are plotted against the transverse coordinate, y, normalized by the airfoil thickness, t_a. For both $\alpha = 8°$ cases the RMS peaks are shifted down which is expected due to the deflection of flow at increased angles of attack. All cases show the peaks flattening and becoming less distinct as x/c increases. The presence of flow reattachment can be inferred by examining the wake profiles near the trailing edge. Previous studies have shown that without flow reattachment the wake is wider compared to when there is flow reattachment [56]. Here the wake width is taken as the size of the profile where the value of u'/U_0 increases above the freestream value. For the $\alpha = 0°$ cases at $x/c = 1.13$, the wake profile for $Re_c = 6.8 \times 10^4$ is larger than the wake profile for $Re_c = 9.8 \times 10^4$ suggesting flow reattachment occurs for the higher Reynolds number. This is substantiated by the flow visualization results which show flow reattachment above $Re_c \approx 8 \times 10^4$.

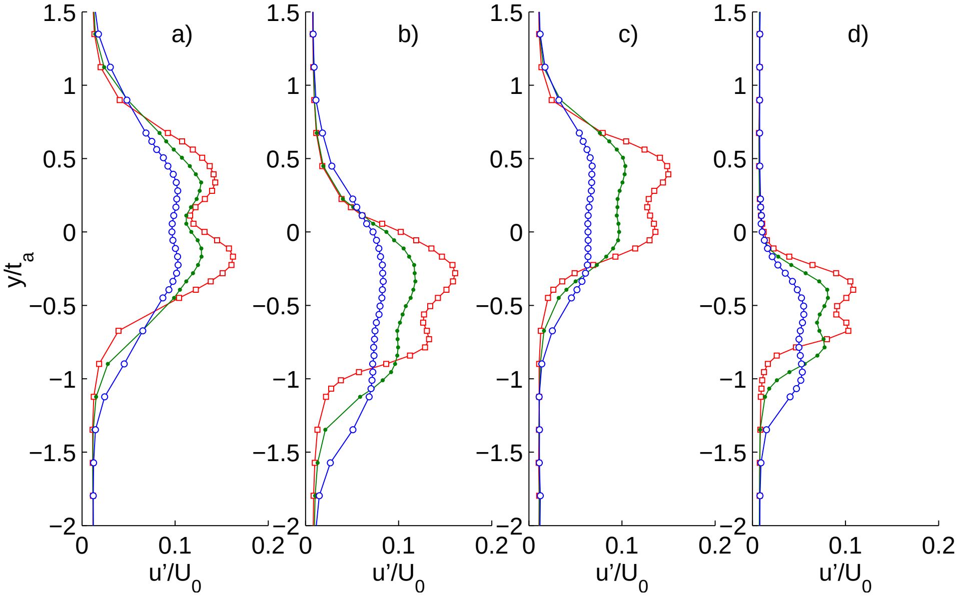

Figure 4.8: Normalized RMS freestream velocity wake profiles, a) $Re_c = 6.8 \times 10^4$, $\alpha = 0°$; b) $Re_c = 6.8 \times 10^4, \alpha = 8°$; c) $Re_c = 9.8 \times 10^4, \alpha = 0°$; d) $Re_c = 9.8 \times 10^4, \alpha = 8°$; □ $x/c = 1.25$; ● $x/c = 1.5$; ○ $x/c = 2$

These data were used to determine the location of the maximum freestream velocity RMS value so the single point LDA measurements could be performed at this location. Linear interpolation was used to determine this location for the velocity and angle of attack cases where a wake profile measurement was not taken. Using the RMS velocity plots the separation between freestream velocity RMS peaks, d^* was calculated for $x/c = 2$ and values are shown in Table 4.2. A 6^{th} order polynomial curve fit was applied to the RMS wake profiles in order to calculate d^*. Due to the large size of the measurement volume relative to the wake, and the separation between measurement points, the calculation of d^* is only accurate to ±0.54 mm. This measurement was used as a length scale in Strouhal number discussed in Subsection 4.4.3.

Table 4.2: d^* values in mm calculated from wake profiles at $x/c = 2$

d^* [mm]		Re_c	
		6.8×10^4	9.8×10^4
α [°]	0	4.5	4.5
	8	5.5	3.5

4.3.2 Velocity Spectrum

Single location LDA and microphone measurements were performed to compare the velocity and acoustic spectra. The LDA measurement volume was positioned at the vertical point corresponding to the maximum freestream RMS value at a downstream location of $x/c = 1.13$. The power spectrum for the transverse velocity component is plotted against frequency in Figure 4.9 for each freestream velocity from 15–35 m/s at $\alpha = 0°$. The spectra are shifted so they are more easily visible. These spectra appear to be divided into three distinct sets: from $U_0 = 15$–17 m/s, from $U_0 = 18$–24 m/s, and from $U_0 = 25$–35 m/s. The $Re_c = 5.1 \times 10^4$ ($U_0 = 15$ m/s) spectrum (shown in detail in Figure 4.10) is representative of the spectra in the $U_0 = 15$–17 m/s range. It is characterized by a strong peak frequency at about 550 Hz with harmonics at 1100 and 1650 Hz. The shedding frequency calculated from the smoke wire photos at $Re_c = 5.1 \times 10^4$ is 870 Hz and correlates with the peak measured with the LDA. The reason for this discrepancy is unknown. However the shedding frequency from the smoke wire images at $Re_c = 3.5 \times 10^4$ is 580 Hz which correlates well with the peak in the LDA results in the $U_0 = 15$–17 m/s range.

The spectrum for the $Re_c = 6.8 \times 10^4$ ($U_0 = 20$ m/s) case which is also shown in Figure 4.10 is indicative of the spectra in the range from $U_0 = 18$–24 m/s. These spectra are characterized by a strong frequency peak at approximately 1100 Hz, with harmonics at 2200, 3300, and 4400 Hz. The smoke wire results for $Re_c = 6.8 \times 10^4$ ($U_0 = 20$ m/s), show the shedding frequency is approximately 1100 Hz. Therefore the strong peak in the LDA spectrum at 1100 Hz is the airfoil's shedding frequency. There was no linear increase in shedding frequency with freestream velocity for the $U_0 = 15$–24 m/s range, a finding reported by Yarusevych and Boutillier [56] for a similar Reynolds number range. This suggests that the behaviour of the Kármán vortex street is not similar to past experiments.

The higher velocity, $Re_c = 9.8 \times 10^4$ ($U_0 = 30$ m/s) case in Figure 4.10 is indicative of the spectra range from $U_0 = 25$–35 m/s. In this range, there are sharp peaks at approximately 3100 and 3800 Hz as well as a broad peak that shifts to higher frequencies with increased freestream velocity. This increase in peak frequency is roughly shown with line $\boxed{1}$ in Figure 4.9. From the smoke wire results for $Re_c = 8.7 \times 10^4$ the shedding frequency is shown to be approximately 1250 Hz, which coincides with the peak in the velocity spectrum. This suggests that the broad frequency peaks denoted by line $\boxed{1}$ are in fact the vortex shedding frequency peaks. Yarusevych and Boutillier [56], and Yarusevych et al. [57] also note broad peaks that correspond to the airfoil's vortex shedding at similar Reynolds numbers. Also, the broad peaks with energy distributed over a frequency range are indicative of the quasi-regular vortex separation nature of the vortex street seen in the smoke wire images.

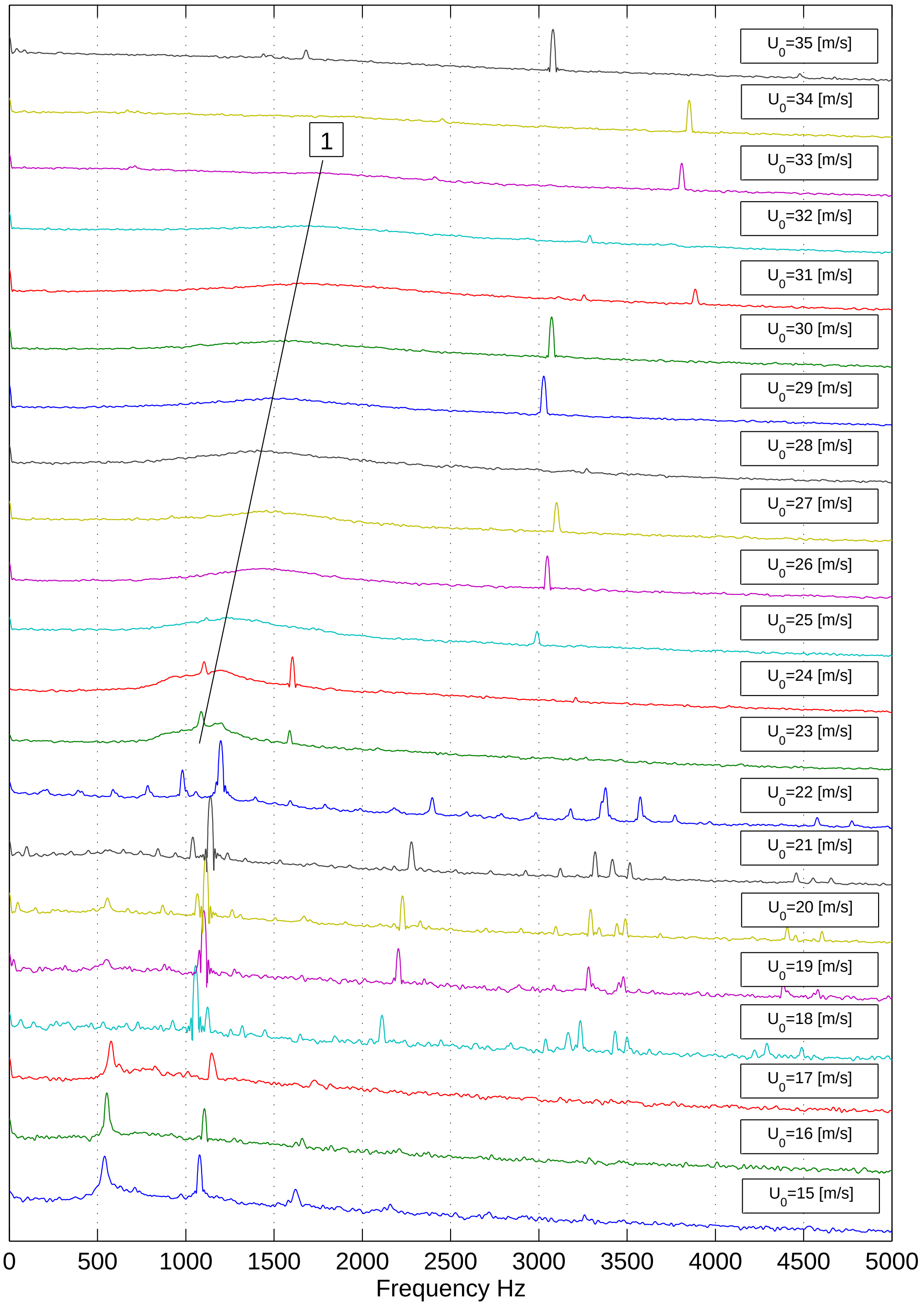

Figure 4.9: Transverse velocity component, E_v, narrowband power spectra at $\alpha = 0°$ for U_0 =15–35 m/s at 1 m/s increments

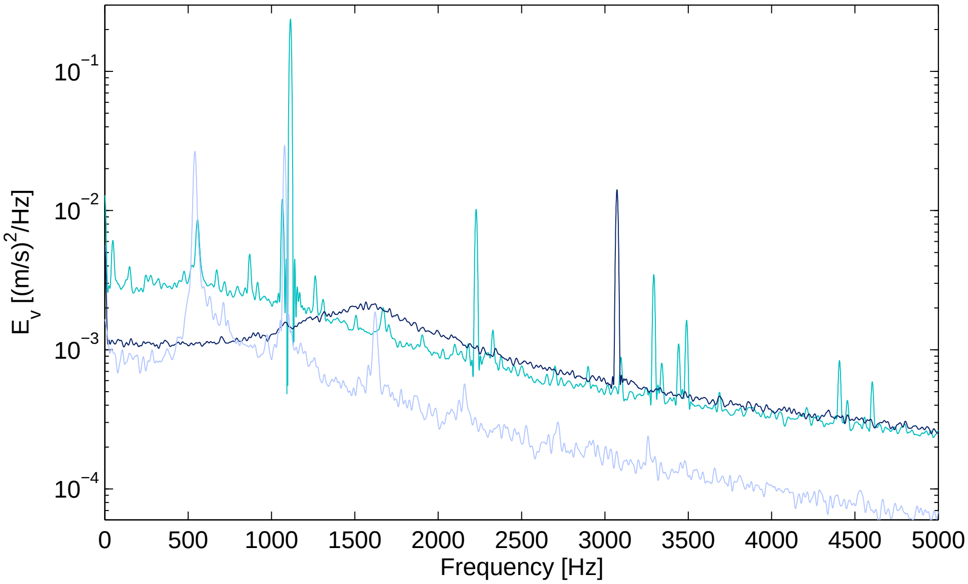

Figure 4.10: Transverse velocity component, E_v, narrowband power spectrum at $\alpha = 0°$, — $Re_c = 5.1 \times 10^4$ ($U_0 = 15$ m/s); — $Re_c = 6.8 \times 10^4$ ($U_0 = 20$ m/s); — $Re_c = 9.8 \times 10^4$ ($U_0 = 30$ m/s)

Single location LDA measurements were also performed at $\alpha = 8°$ over a range of U_0 =15–35 m/s. A shedding frequency of approximately 1100 Hz was detected for U_0 =15–18 m/s, however no distinct shedding frequencies were detected above this velocity range. As a result, the data for $\alpha = 8°$ will not be discussed further.

4.4 Acoustic Results

4.4.1 Acoustic Spectrum

The narrowband acoustic spectra for $Re_c = 5.1 \times 10^4$ ($U_0 = 15$ m/s), $Re_c = 6.8 \times 10^4$ ($U_0 = 20$ m/s), and $Re_c = 9.8 \times 10^4$ ($U_0 = 30$ m/s) at $\alpha = 0°$ are presented in Figure 4.11. Both the $Re_c = 5.1 \times 10^4$ and $Re_c = 6.8 \times 10^4$ cases are characterized by a very strong pure tone of greater than 100 dB at approximately 1100 Hz with a much weaker subharmonic at 550 Hz. This pure tone was clearly audible during the tests. Harmonics at 2200, 3300, and 4400 Hz are also present. This is unlike the LDA spectra results which show the fundamental peak at 550 Hz for U_0 =15–17 m/s as opposed to 1100 Hz in the case of the acoustic spectra. Smaller, broader peaks are also present at approximately 2600, 3100, 3800, and 4700 Hz. The $Re_c = 9.8 \times 10^4$ case exhibits similar peaks although at different amplitudes. In general, the broadband noise level is higher compared to the

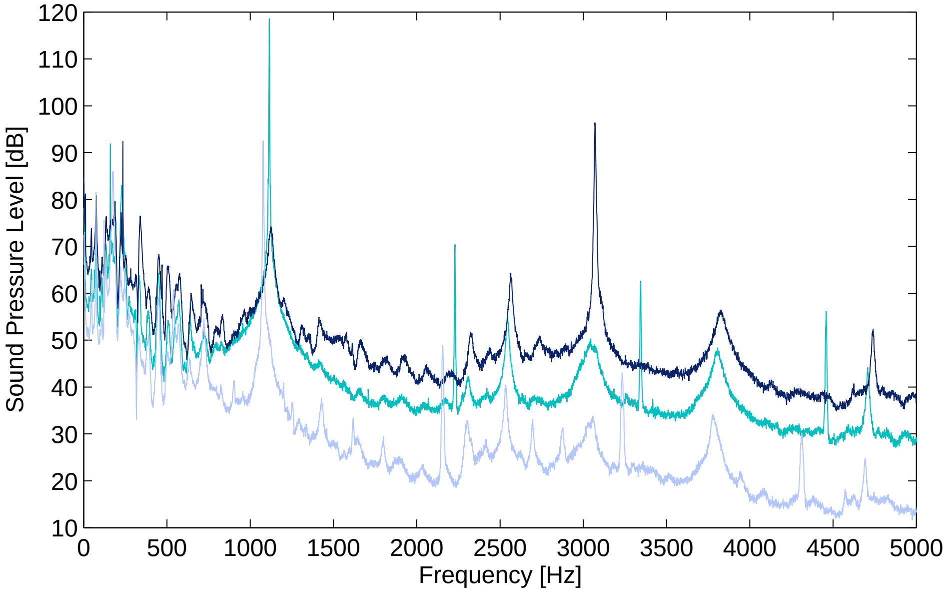

Figure 4.11: Narrowband sound pressure levels at $\alpha = 0°$, — $Re_c = 5.1 \times 10^4$ ($U_0 = 15$ m/s); — $Re_c = 6.8 \times 10^4$ ($U_0 = 20$ m/s); — $Re_c = 9.8 \times 10^4$ ($U_0 = 30$ m/s)

lower velocity case because the tunnel is louder at higher velocities. The strongest pure tone is 85 dB at 3100 Hz, and lower amplitude peaks are present at 1100, 2600, 3800, and 4700 Hz. The spectra for all freestream velocities from 15–35 m/s are shown in Appendix A. The 1100, 2600, 3100, and 3800 Hz peaks were always present in acoustic spectra but only 1100, 3100, and 3800 Hz were amplified at specific speeds. To gain insight into the origin of these peak frequencies, the background noise level of the test section without the airfoil was examined which is shown in Figure 4.12. None of the peaks in question (1100, 2600, 3100, and 3800 Hz) correspond to peaks in the background noise spectrum. This shows that these peaks were not caused solely by the wind tunnel. Only the small peak at approximately 2300 Hz is present in both spectra suggesting this tone is caused by the wind tunnel alone. Acoustic measurements were also performed for freestream velocities from 15–35 m/s at $\alpha = 8°$. Compared to the $\alpha = 0°$ cases, no high decibel pure tones were measured, however peaks were observed at frequencies of approximately 1100, 2600, 3100, and 3800. This is shown in Figure 4.13 with the narrowband acoustic spectra for $Re_c = 6.8 \times 10^4$ and $Re_c = 9.8 \times 10^4$ at $\alpha = 8°$.

4.4.2 Wind Tunnel Resonance

The acoustic measurements show intense pure tones at 1100, 2600, 3100, and 3800 Hz. It is believed that these tones are caused by wind tunnel resonance as opposed to airfoil trailing

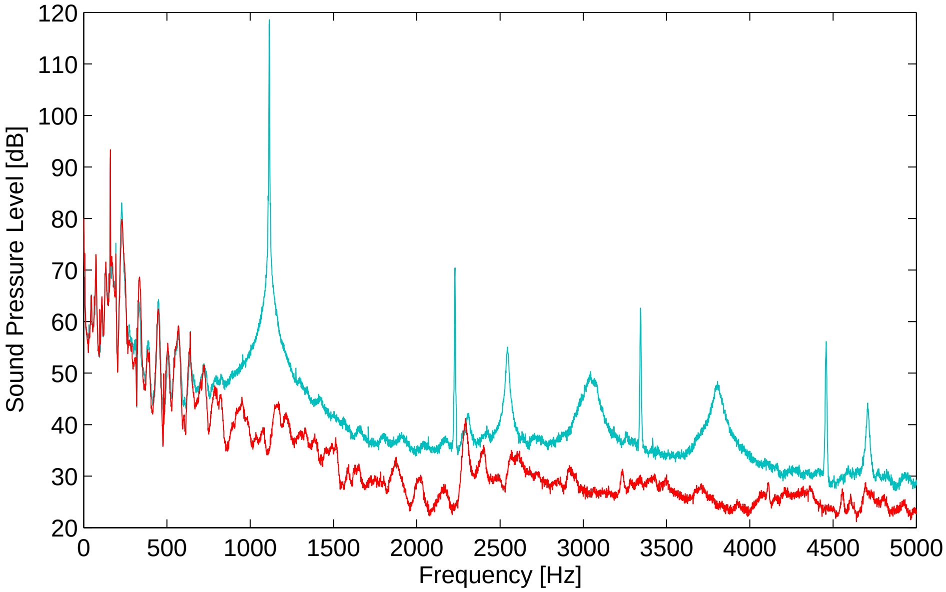

Figure 4.12: Narrowband sound pressure levels at $Re_c = 6.8 \times 10^4$ ($U_0 = 20$ m/s), $\alpha = 0°$, — with airfoil; — without airfoil

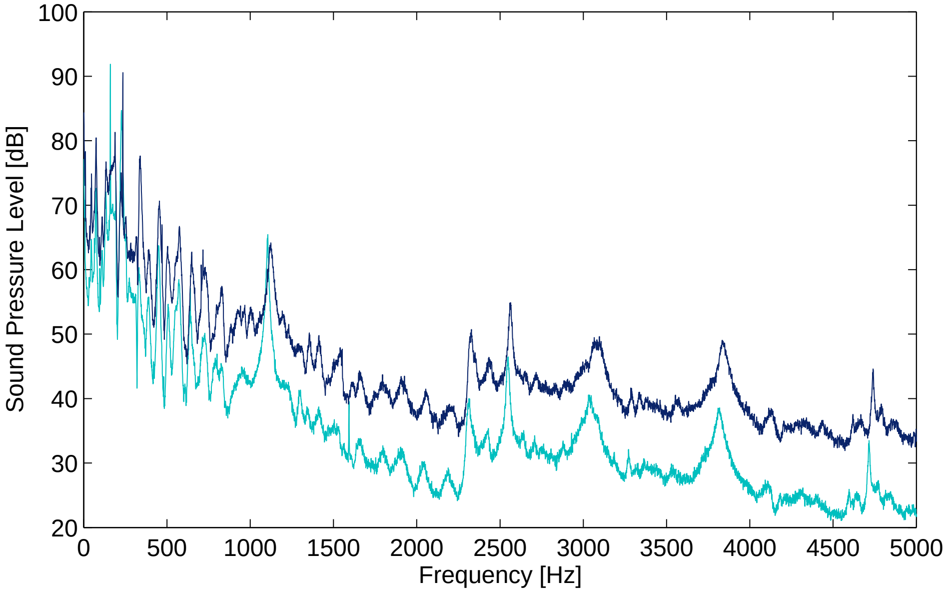

Figure 4.13: Narrowband sound pressure levels at $\alpha = 8°$, — $Re_c = 6.8 \times 10^4$ ($U_0 = 20$ m/s); — $Re_c = 9.8 \times 10^4$ ($U_0 = 30$ m/s)

edge noise. To further confirm this, Parker's resonance model [13] was used to predict the resonant frequency based on the airfoil chord and the test section geometry. This model was developed by measuring the standing wave frequencies from a cascade of plates in a wind tunnel and relating the detected frequencies to the cascade geometry. Using Equation 2.3 the β_P mode resonant frequency was calculated to be approximately 1120 Hz. This prediction matches the measured intense pure tone of 1100 Hz that is present at lower test velocities. Although there is a peak at 1100 Hz in the acoustic spectrum at all velocities it is only amplified at lower velocities. At higher velocities, intense pure tones are present at 3100 and 3800 Hz however these frequencies could not be predicted with Parker's resonance model [13]. It is more than likely that these frequencies are the result of a complex superposition of standing waves or three-dimensional standing waves as hypothesized by Parker [13].

4.4.3 Correlation of Acoustic and Velocity Spectra

To assess the relationship between the LDA spectra, acoustic spectra, and shedding frequency calculations from the smoke wire images, the detected peak frequency vs Reynolds number is plotted in Figure 4.14. A data point is plotted for any peak that is present in both the LDA and acoustic spectra; therefore some Reynolds numbers have multiple data points. For the U_0 = 15–24 m/s range the peaks from both the LDA and acoustic spectra are extremely consistent. From the smoke wire images at $Re_c = 6.8 \times 10^4$, $\alpha = 0°$ the shedding frequency is calculated to be 1100 Hz which is also coherent with the LDA and acoustic data. This shows that the β_P mode resonant frequency is forcing the shedding frequency in this range. This result is unlike the findings of Yarusevych et al. [82] who reported attenuation of the vortex shedding frequency when speakers in the test section emitted a pure tone of the same frequency. This is an undesired result that was not foreseen at the time of planning the experiment.

The sudden jump in peaks from 1100 Hz to 3100 Hz to 3800 Hz in Figure 4.14 is similar to Parker and Griffiths' [14] results in Figure 2.4 which shows a "ladder-like" relationship between frequency and velocity. For wind tunnel tests of a NACA 0012 airfoil, Nash et al. [15] also report a "ladder-like" peak frequency vs freestream velocity relationship which is attributed to resonance due to the hard wall test section. The similarity of the present results to past studies further suggests that the frequencies at 3100 and 3800 Hz are a result of test section resonance. The peaks at these frequencies are not believed to be related to the vortex shedding frequency of the airfoil. However the cause of the flow structures causing these sharp peaks in the LDA spectra is unclear. The shedding frequency from smoke wire results for $Re_c = 8.7 \times 10^4$ is 1250 Hz. This correlates well with the series of broad peaks in the LDA spectra that increase from 1200–1700 Hz as shown in the U_0 = 25–35 m/s range in Figure 4.14. These broad peaks represent the vortex shedding. The shedding frequency increases with freestream velocity, but not as quickly as in the

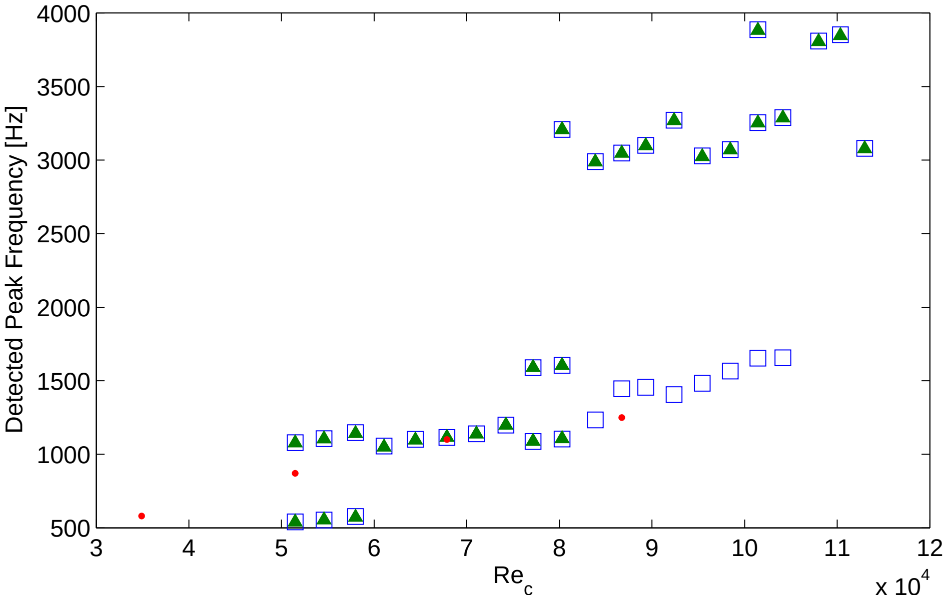

Figure 4.14: Detected peak frequency vs Re_c data at $\alpha = 0°$, □ LDA data; ▲ acoustic data; ● smoke wire data

results of Yarusevych and Boutillier [56].

Yarusevych et al. [57] and Yarusevych and Boutillier [56] showed the Strouhal vs Reynolds number data very approximately collapsed onto two horizontal lines, one for the case without flow reattachment, $St_{d^*} \approx 0.2$ and one with flow reattachment, $St_{d^*} \approx 0.16$. This Strouhal number, St_{d^*} is based on the separation between RMS peaks in the wake, d^*. This scaling is applied to the present data and shown in Figure 4.15 along with the data of Yarusevych et al. [57] and Yarusevych and Boutillier [56]. The length scale d^* was measured to be approximately 4.5 mm for both $Re_c = 6.8 \times 10^4$ and $Re_c = 9.8 \times 10^4$, therefore this value was used for all data points. The "without flow reattachment" data are reasonably close to the expected value of $St_{d^*} \approx 0.2$. However, the "with flow reattachment" data do not shift to $St_{d^*} \approx 0.16$ like the data of past experiments. Although the results do not fall onto the predicated values it is reasonably close considering the error associated with the calculation of d^*. If d^* is calculated based on the expected values of St_{d^*}, for the "without flow reattachment" data, $d^* \approx 3.7$ mm and for the "with flow reattachment" data, $d^* \approx 3.1$ mm. Both of these are reasonable values for d^*.

4.4.4 Preliminary Microphone Array Results

The original intention was to use the microphone phased array to quantify and locate the trailing edge noise from the airfoil. Due to the test section resonance this was abandoned.

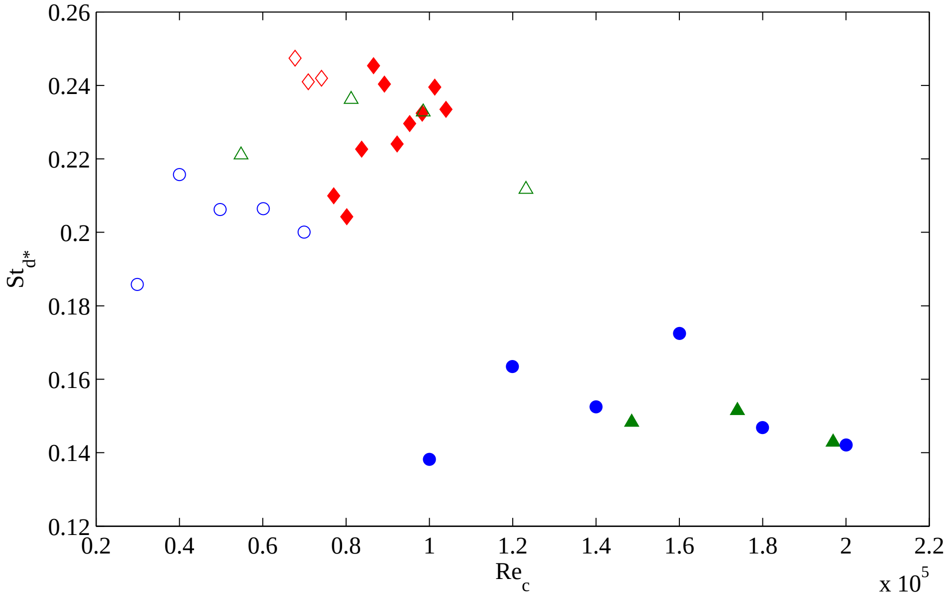

Figure 4.15: St_{d^*} vs Re_c plot, ◇ no flow reattachment, ◆ flow reattachment, $\alpha = 0°$ present work; ○ no flow reattachment, ● flow reattachment, NACA 0018 airfoil $\alpha = 10°$ Yarusevych and Boutillier [56]; △ no flow reattachment, ▲ flow reattachment, NACA 0025 airfoil $\alpha = 10°$ Yarusevych et al. [57]

However preliminary microphone phased results for a monopole source are presented. Using a monopole source initial tests with the microphone array were performed. Tests were performed at array-to-source separation distances of 164 mm and 385 mm. For each distance tests were performed with source pure tones of 3, 5, and 7 kHz. The source was placed in line with the center of the array (at the origin of the beam map). The scanning grid for the 164 mm case is 400 mm × 400 mm with a grid spacing of 2.5 mm and for the 385 mm case is 800 mm × 800 mm with a grid spacing of 5 mm. The 1/3-octave-band beam maps for the 164 mm separation case are shown in Figure 4.16 and the 385 mm separation case beam maps are shown in Figure 4.16. For all tests the microphone array and beamforming code are able to accurately locate the monopole source. The beamwidth (diameter of the main lobe measured 3 dB below the peak) is calculated for each beam map and presented in Table 4.3. The results show that as the frequency increases the beamwidth decreases which is in agreement with Equation 2.24. The beamwidth increases with array-to-source separation distance, which is also in agreement with Equation 2.24.

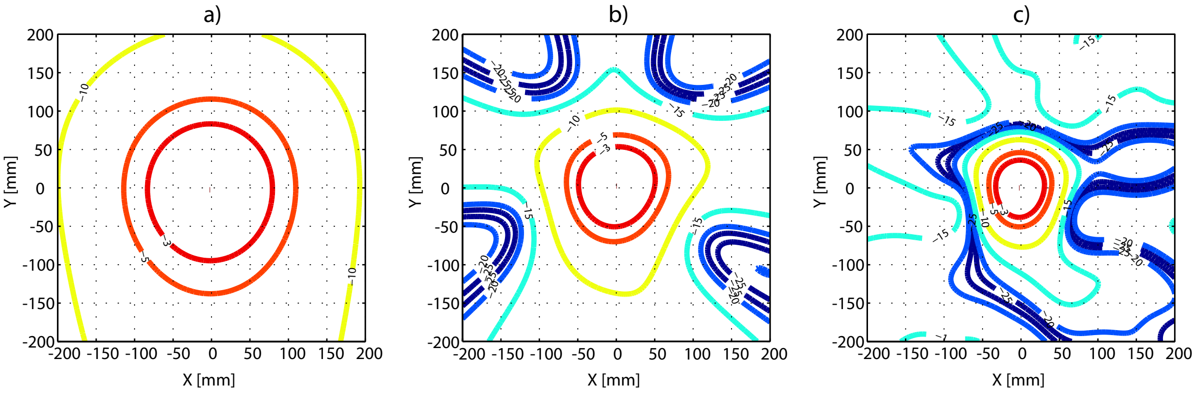

Figure 4.16: Source maps for a separation of 164 mm for a) 3 kHz, b) 5 kHz, and c) 7 kHz

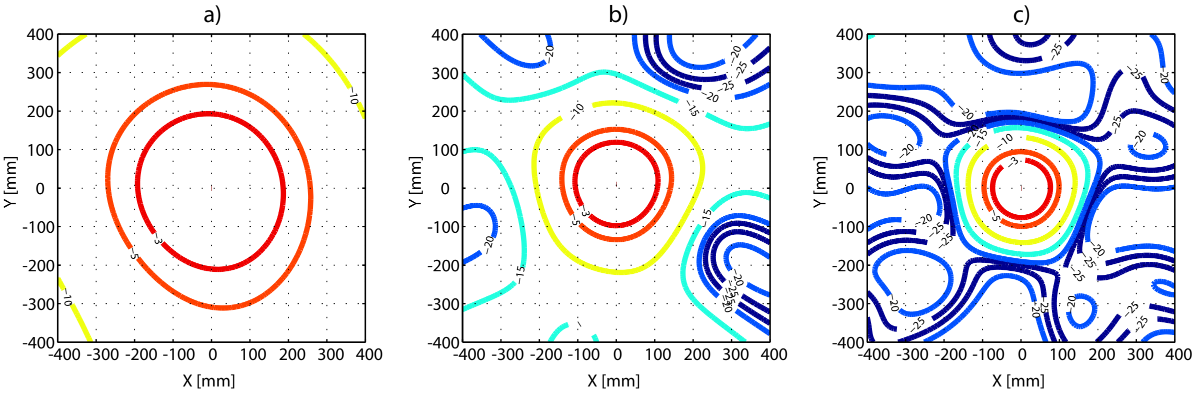

Figure 4.17: Source maps for a separation of 385 mm for a) 3 kHz, b) 5 kHz, and c) 7 kHz

Table 4.3: Beamwidths

	3 kHz	5 kHz	7 kHz
164 mm separation	170 mm	102 mm	69 mm
385 mm separation	390 mm	216 mm	150 mm

Chapter 5

Conclusions

5.1 Wind Tunnel

Several modifications to the Sperandei [63] wind tunnel were made before the present work was completed. With the addition of steel diffuser vanes and two low porosity (54%) turbulence reduction screens the turbulence intensity was lowered to approximately 1.1%. Melamine foam was fixed to the inside of the wind tunnel which successfully reduced the background noise from approximately 42 dB to 27 dB above 1000 Hz.

5.2 Flow Visualization

5.2.1 Smoke Wire Visualization

Smoke wire flow visualization was successfully performed at Reynolds numbers of 3.5×10^4, 5.1×10^4, 6.8×10^4, and 8.7×10^4 at $\alpha = 0°$, and at Reynolds numbers of 3.5×10^4, and 5.1×10^4 at $\alpha = 8°$. This process allowed for the visualization of flow reattachment (if any) as well as the calculation of the vortex shedding frequency. The flow separation details are summarized in Table 5.1 and the shedding frequencies are summarized in Table 5.2. According to Lissaman [20] and Carmichael [21] flow reattachment will likely not occur below $Re_c \approx 7 \times 10^4$ which was proven with the smoke wire results. However reattachment was observed below this threshhold for the $Re_c = 5.1 \times 10^4$, $\alpha = 8°$ case. This is possibly due to the increased turbulence due to the higher angle of attack.

5.2.2 Oil Film Visualization

The oil film visualization method was successfully used to assess the boundary layer flow over the airfoil. The oil film visualization showed no flow reattachment below $Re_c \approx 8 \times 10^4$ for low angles of attack which correlates well with the smoke wire visualization results.

Table 5.1: Presence of flow reattachment from smoke wire results

		$Re_c \times 10^{-4}$			
		3.5	5.1	6.8	8.7
α [°]	0	no	no	no	yes
	8	no	yes	no data	no data

Table 5.2: Vortex shedding frequency, f_s [Hz] calculated from smoke wire images

		$Re_c \times 10^{-4}$			
		3.5	5.1	6.8	8.7
α [°]	0	580	870	1100	1250
	8	340	700	no data	no data

5.3 Velocity Measurements

Wake profile and single point LDA measurements were undertaken on the S822 airfoil. The wake profiles were measured to determine the separation between freestream velocity RMS peaks, d^*, and to determine the maximum RMS location for the single point measurements. Examination of the wake profiles also provided further evidence that flow reattachment occurs at $Re_c \approx 8 \times 10^4$. Flow reattachment is accompanied by the narrowing of the wake width which is visible in the wake profile results.

The single point LDA measurements revealed information about the energy spectrum in the wake. The results revealed three distinct velocity spectrum ranges; U_0 = 15–17 m/s, U_0 = 18–24 m/s, and U_0 = 25–35 m/s. The two lower velocity ranges showed strong peaks at approximately 550 Hz and 1100 Hz but no increase in frequency with Reynolds number. The 1100 Hz peak corresponds well to the 1100 Hz shedding frequency calculated from the smoke wire measurement at $Re_c = 6.8 \times 10^4$. The U_0 = 25–35 m/s range exhibits sharp peaks at 3100 and 3800 Hz, and broad peaks which increase in frequency with Reynolds number. The broad peaks with increasing frequency are indicative of the vortex shedding frequencies reported by Yarusevych and Boutillier [56], and Yarusevych et al. [57]. The shedding frequency of 1250 Hz calculated from the smoke wire measurement at $Re_c = 8.7 \times 10^4$ lines up well with this series of broad peaks. Therefore this series of broad peaks from U_0 = 25–32 m/s represent the shedding frequencies. The Strouhal number based on the separation d^* was calculated and plotted against the results of Yarusevych and Boutillier [56], and Yarusevych et al. [57]. The "without flow reattachment" data points line up reasonably well with past results but the "with flow reattachment" data points are approximately 25% higher than past results. This discrepancy is largely due to the error associated with the measurement of d^*.

5.4 Acoustic Measurements

Acoustic measurements inside the test section were performed along with the LDA measurements. Pure tones of 1100, 2600, 3100, and 3800 Hz were observed at all Reynolds numbers tested however only certain frequencies were amplified at certain Reynolds numbers. By comparing the acoustic spectrum with and without the airfoil it was found that these peaks are caused by the presence of the airfoil and are not due to the wind tunnel alone. It was hypothesized that these strong peaks were caused by resonance in the test section. Using the Parker [13] resonance model, the tone at 1100 Hz in the $U_0 = 15$–24 m/s range was predicted based on the airfoil and test section geometry. This 1100 Hz peak was measured by the LDA in this velocity range and using smoke wire visualization the shedding frequency was measured to be 1100 Hz at $Re_c = 6.8 \times 10^4$ ($U_0 = 20$ m/s). This evidence strongly suggests that in this velocity range, the resonance is forcing the shedding frequency. The strongest tones of 1100, 3100, and 3800 Hz exhibited a "ladder-like" relationship with the freestream velocity which is indicative of test section resonance as shown by Parker [13]. Therefore in addition to the 1100 Hz resonance the peaks at 3100 and 3800 Hz are likely due to test section resonance. The peaks at 3100 and 3800 Hz were also measured with the LDA meaning the resonance is causing oscillating flow structures. The nature of these flow structures was not investigated further.

Since the resonance has such a large effect on the airfoil noise generation, the acoustic results are not applicable to any real world wind turbine applications. Although the initial goal was to use the microphone array to measure the trailing edge noise, this was never accomplished and only preliminary tests in a stationary flow field were done. However these tests did show that both the array and beamforming code performed as expected. The array in combination with the beamforming code were able to accurately locate simple monopoles sources of 3, 5, and 7 kHz at two distances.

Chapter 6

Recommendations

6.1 Wind Tunnel

It was found that wind tunnel resonance was the most significant contributing factor to the undesirable results. The resonance model proposed by Parker [13] shows that β_P mode resonance will not occur if the ratio of airfoil chord to test section height is much less than 0.4. This should be used as a design parameter for the planning of future aeroacoustic experiments in hard walled wind tunnels. In general a large test section will result in lower resonant frequencies. By lowering the frequency of resonance there is less of a chance the resonance will interfere with the airfoil vortex shedding.

6.2 Flow Visualization

6.2.1 Smoke Wire Visualization

The majority of the difficulty in taking smoke wire flow visualization still images was in manually timing the electric current and camera shutter. This was best done with two people, one operating the electric current and the other operating the camera. Due to the very short amount of time that the smoke lasted, the camera would often not capture the smoke. To improve the smoke wire visualization process for still images a system to trigger both the camera and electric current should be designed. This could be accomplished using LabVIEW and a National Instruments data acquisition system with analog outputs (such as the NI PCI-6251). Through the analog output of the data acquisition, the variable transformer can be controlled via a relay. The camera's infrared remote can be triggered through the analog output; however there are a variety of ways to trigger the camera depending on the camera and available software. This system would also allow for the precise control over the duration of the electric current, which will significantly reduce the number of times the wire breaks due to overheating. Additionally with proper synchronization it may be possible to photograph high velocity flows with the still camera as opposed to the high speed camera. With the acquisition of a newer flash unit capable of flash bursts, a series of images could be captured.

A stainless steel wire was used for the experiments presented in this work; however the use of a Nichrome alloy wire should be investigated. Nichrome is often used for heating elements because of its strength at high temperatures [83]. This could result in fewer broken wires due to overheating, thus improving the reliability of the smoke wire method.

6.2.2 Oil Film Visualization

The oil film flow visualization results can be improved by painting the airfoil a matte black and using a fluorescent or white pigment such as titanium-dioxide. The high reflectance of the bare machined aluminum airfoil proved to be difficult to photograph and a non-reflective surface would improve results. Attempts can be made to replicate the oil film visualization process of Selig and McGranahan[28] in which the fluorescent pigment suspended in oil was applied with an airbrush. This process allowed for more detailed results of the boundary layer flow development. However it was noted that this process works best for airfoils larger than the $c = 55$ mm airfoil used in this thesis.

6.3 Velocity Measurements

The LDA measurements undertaken were primarily inhibited by the size of the airfoil relative to the measurement volume. A larger airfoil would create a larger wake and therefore the d^* separation would be larger relative to the measurement volume. This would lower the error associated with the d^* measurement and hence result in a more accurate calculation of St_{d^*}. LDA measurements of the boundary layer were not undertaken due to the size of the boundary layer being approximately the same order of magnitude as the measurement volume. A larger airfoil hence larger boundary layer would facilitate boundary layer measurements with the LDA. These measurements could be used to investigate the relationship between airfoil trailing edge noise sound pressure level and boundary layer thickness.

The current Dantec LDA system comes with a 4 channel 62N520 Analog/Digital input card. Although this system was not used, it could be used to record pressure, temperature, humidity, noise or any other sensor output simultaneously with the LDA measurements.

6.4 Acoustic Measurements

Due to the resonance in the wind tunnel, any further attempts to use the microphone phased array in it would only yield unsatisfactory results. A larger wind tunnel is needed if microphone phased array tests on an airfoil need to be performed. The wind tunnel should be large enough such that the chord to tunnel height ratio (c/h) is well below 0.4 as recommended by Parker [13] to avoid resonance.

Although the microphone phased array was successfully built and tested, due to its small size, it has poor resolution of lower frequency noise. Building on the knowledge gained from the preliminary array, a larger array should be designed and tested. It is recommended to again use MEMS microphones with built-in amplification due to their low cost and simplicity. A larger array could potentially be used to measure noise from a small wind turbine.

References

[1] Howe, B., B. Gastmeier and N. McCabe, *Wind Turbines and Sound: Review and Best Practice Guidelines*. Tech. rep., HGC Engineering Limited, 2007. 1, 2

[2] Ramakrishnan, R., *Wind Turbine Facilities Noise Issues*. Tech. rep., Aiolos Engineering Corporation, 2007. 1

[3] Colby, W. D., R. Dobie, G. Leventhall, D. M. Lipscomb, R. J. McCunney, M. T. Seilo and B. Søndergaard, *Wind Turbine Sound and Health Effects, An Expert Panel Review*. Tech. rep., American Wind Energy Association and Canadian Wind Energy Association, 2009. 1, 2

[4] Burton, T., D. Sharpe, N. Jenkins and E. Bossanyi, *Wind Energy Handbook*. Chichester: John Wiley & Sons, Inc., 2001. 3

[5] Wagner, S., R. Bareiss and G. Guidati, *Wind Turbine Noise*. Berlin: Springer, 1996. 3

[6] Oerlemans, S. and B. M. Lopez, *Acoustic Array Measurements on a Full Scale Wind Turbine*. In *11th AIAA/CEAS Aeroacoustics Conference, Monterey, California*, vol. 2005-2963, 2005. 3, 4, 26, 28

[7] Oerlemans, S., M. Fisher, T. Maeder and K. Kögler, *Reduction of Wind Turbine Noise Using Optimized Airfoils and Trailing-Edge Serrations*. AIAA, 47(6):1470–1481, 2009. 3, 4, 29

[8] Migliore, P., *The Potential for Reducing Blade-Tip Acoustic Emissions For Small Wind Turbines*. Subcontractor Report SR-500-43472, NREL, 2009. 4

[9] Barlow, J. B., W. H. Rae Jr. and A. Pope, *Low-Speed Wind Tunnel Testing, Third Edition*. New York: John Wiley & Sons, Inc., 1999. 6, 33, 34, 41, 94

[10] Blake, W. K. and D. A. L. III, *Aeroacoustic Measurements*, chap. Beamforming In Acoustic Testing, 218–257. Berlin: Springer, 2002. 6

[11] Remillieux, M. C., E. D. Crede, H. E. Camargo, R. A. Burdisso, W. J. Deveport, M. Resnick, P. V. Seeters and A. Chou, *Calibration and Demonstration of the New Virginia Tech Anechoic Wind Tunnel.* In *14th AIAA/CEAS Aeroacoustics Conference, Vancouver, British Columbia, Canada*, vol. 2008-2911, 2008. 7, 36, 37, 56

[12] Parker, R., *Resonance Effects In Wake Shedding From Parallel Plates: Some Experimental Observations.* Journal of Sound and Vibration, 4(1):62–72, 1966. 7

[13] Parker, R., *Resonance Effects In Wake Shedding From Parallel Plates: Calculation of Resonant Frequencies.* Journal of Sound and Vibration, 5(2):330–343, 1967. 7, 8, 9, 74, 80, 81, 83

[14] Parker, R. and W. M. Griffiths, *Low Frequency Resonance Effects In Wake Shedding From Parallel Plates.* Journal of Sound and Vibration, 7(3):371–379, 1968. 7, 9, 10, 74

[15] Nash, E. C., M. V. Lowson and A. McAlpine, *Boundary-Layer Instability Noise on Aerofoils.* Journal of Fluid Mechanics, 382:27–61, 1999. 8, 25, 29, 30, 37, 74

[16] Nakano, T., N. Fujisawa and S. Lee, *Measurement of tonal-noise characteristics and periodic flow structure around NACA0018 airfoil.* Experiments in Fluids, 40:482–490, 2006. 8, 12, 30, 64

[17] Nakano, T., N. Fujisawa, Y. Oguma, Y. Takagi and S. Lee, *Experimental Study on Flow and Noise Characteristics of NACA0018 Airfoil.* Journal of Wind Engineering and Industrial Aerodynamics, 95:511–531, 2007. 8, 12, 25, 30, 64

[18] Zaman, K. B. M. Q., A. Bar-Sever and S. M. Mangalam, *Effect of Acoustic Excitation on the Flow Over a low-Re Airfoil.* Journal of Fluid Mechanics, 182:127–148, 1987. 8

[19] Wood, C. J., *The Effect of Lateral Vibrations on Vortex Shedding From Blunt-Based Aerofoils.* Journal of Sound and Vibration, 14(1):91–102, 1971. 8

[20] Lissaman, P. B. S., *Low-Reynolds-Number Airfoils.* Annual Review of Fluid Mechanics, 15:223–239, 1983. 11, 12, 64, 78

[21] Carmichael, B. H., *Low Reynolds Number Airfoil Survey Volume I.* Contractor Report 165803, NASA, 1982. 11, 12, 61, 64, 78

[22] Gerakopulos, R., M. S. H. Boutilier and S. Yarusevych, *Aerodynamic Characterization of a NACA 0018 Airfoil at Low Reynolds Numbers.* In *40th Fluid Dynamics Conference and Exhibit, Chicago, Illinois*, vol. 2010-4629, 2010. 12, 64

[23] Hu, H. and Z. Yang, *An Experimental Study of the Laminar Flow Separation on a Low-Reynolds-Number Airfoil*. Journal of Fluids Engineering, 130:1–11, 2008. 12

[24] Mueller, T. J., L. J. Pohlen, P. E. Conigliaro and B. J. Jansen Jr., *The Influence of Free-Stream Disturbances on Low Reynolds Number Airfoil Experiments*. Experiments in Fluids, 1(1):3–14, 1983. 12

[25] Yarusevych, S., P. E. Sullivan and J. G. Kawall, *Smoke-Wire Flow Visualization in Separated Flows at Relatively High Velocities*. AIAA, 47(6):1592–1595, 2009. 13, 45

[26] Yang, W.-J., *Handbook of Flow Visualization*. New York: Hemisphere Pub. Corp., 1989. 13

[27] Merzkirch, W., *Flow Visualization*. Orlando: Academic Press, 2nd ed., 1987. 13

[28] Selig, M. S. and B. D. McGranahan, *Wind Tunnel Aerodynamic Tests of Six Airfoils for Use on Small Wind Turbines*. Subcontractor Report SR-500-34515, NREL, 2004. 14, 41, 42, 43, 47, 63, 82, 94

[29] Absil, L. H. J. and D. M. Passchier, *An Experimental Study of the Trailing Edge Flow of an NLR 7702 Airfoil, Using Laser-Doppler Anemometry*. Experimental Thermal and Fluid Science, 9:174–185, 1994. 15

[30] Cuerno-Rejado, C., G. López-Martínez, J. L. Escudero-Arahuetes and J. López-Díez, *Experimental Aerodynamic Characteristics of NACA0012 Airfoils With Simulated Glaze and Rime Ice*. Proceedings Institution of Mechanical Engineers, 215 Part G:229–240, 2001. 15

[31] Albrecht, H.-E., M. Borys, N. Damaschke and C. Tropea, *Laser Doppler and Phase Doppler Measurement Techniques*. New York: Springer, 2002. 15, 16, 49, 95, 96

[32] Dantec Dynamics A/S, *BSA Flow Software Version 4 Installation & User's Guide*, 2005. 16, 17, 52, 96, 97

[33] Kinsler, L. E., A. R. Fry, A. B. Coppens and J. V. Sanders, *Fundamentals of Acoustics*. New York: John Wiley & Sons, Inc., 2000. 18

[34] Norton, M. and D. Karczub, *Fundamentals of Noise and Vibration Analysis for Engineers*. Cambridge: Cambridge University Press, 2nd ed., 2003. 18, 19

[35] Finch, R. D., *Introduction to Acoustics*. Upper Saddle River: Prentice-Hall, 2005. 19

[36] Brooks, T. F., D. S. Pope and M. A. Marcolini, *Airfoil Self-Noise and Prediction*. Reference Publication 1218, NASA, 1989. 19, 20, 25, 26, 27, 28, 29

[37] Hutcheson, F. V. and T. F. Brooks, *Effects of Angle of Attack and Velocity on Trailing Edge Noise*. International Journal of Aeroacoustics, 5(1):39–66, 2006. 19, 25

[38] Howe, M. S., *Acoustics of Fluid-Structure Interactions*. Cambridge: Cambridge University Press, 1998. 20

[39] Justice, J. H., N. L. Owsley, J. L. Yen and A. C. Kak, *Array Signal Processing*. Upper Saddle River: Prentice-Hall, 1985. 20

[40] Johnson, D. H. and D. E. Dudgeon, *Array Signal Processing*. Upper Saddle River: Prentice-Hall, 1993. 20, 21

[41] Oerlemans, S., *Detection of aeroacoustic sound sources on aircraft and wind turbines*. Ph.D. thesis, University of Twente, 2009. 21, 22, 23, 24, 25, 29

[42] Brooks, T. F. and W. M. Humphreys Jr., *A Deconvolution Approach for the Mapping of Acoustic Sources (DAMAS) Determined from Phased Microphone Arrays*. In *10th AIAA/CEAS Aeroacoustics Conference, Manchester, UK*, vol. 2004-2954, 2004. 22

[43] Humphreys Jr., W. M., T. F. Brooks, W. W. Hunter Jr. and K. R. Meadows, *Design and Use of Microphone Directional Arrays for Aeroacoustic Measurements*. In *36th Aerospace Sciences Meeting and Exhibit, Reno, Nevada*, vol. 98-0471, 1998. 22, 24

[44] Humphreys Jr., W. M., Q. A. Shams, S. S. Graves, B. S. Sealey, S. M. Bartram and T. Comeaux, *Application of MEMS Microphone Array Technology to Airframe Noise Measurements*. In *11th AIAA/CEAS Aeroacoustics Conference, Monterey, California*, vol. 2005-3004, 2005. 22, 54

[45] Brooks, T. F. and W. M. Humphreys Jr., *Effect of Directional Array Size On The Measurement of Airframe Noise Components*. In *5th AIAA/CEAS Aeroacoustics Conference, Seattle, Washington*, vol. 99-1958, 1999. 22, 25, 54

[46] Dougherty, R. P., *Aeroacoustic Measurements*, chap. Beamforming In Acoustic Testing, 62–97. Berlin: Springer, 2002. 22

[47] Underbrink, J. R., *Aeroacoustic Measurements*, chap. Aeroacoustic Phased Array Testing in Low Speed Wind Tunnels, 98–215. Berlin: Springer, 2002. 23, 55

[48] Shepherd, K. P. and H. H. Hubbard, *Sound Propagation Studies For a Large Horizontal Axis Wind Turbine*. Contractor Report 172564, NASA, 1985. 24

[49] Hubbard, H. H. and K. P. Shepherd, *Wind Turbine Acoustics*. Technical Paper 3057, DOE/NASA, 1990. 24

[50] Amiet, R. K., *Refraction of Sound by a Shear Layer*. Journal of Sound and Vibration, 58:467–482, 1978. 24

[51] Schlinker, R. H. and R. K. Amiet, *Refraction and Scattering of Sound by a Shear Layer*. Contractor Report 3371, NASA, 1980. 24

[52] Oerlemans, S., *Wind Tunnel Aeroacoustic Tests of Six Airfoils for Use on Small Wind Turbines*. Subcontractor Report SR-500-35339, NREL, 2004. 25, 26, 29, 43, 44, 52

[53] Barone, M. F. and D. Bergy, *Aerodynamic and Aeroacoustic Properties of a Flatback Airfoil: An Update*. In *47th AIAA Aerospace Sciences Meeting, Orlando, Florida*, vol. AIAA 2009-271, 2009. 25

[54] Bahr, C., *An Assessment of Trailing Edge Noise Measurement Techniques*. Ph.D. thesis, University of Florida, 2010. 25

[55] McPhee, A. D., *The Development of a Research Technique for Low Speed Aeroacoustics*. Master's thesis, University of Waterloo, 2008. 26, 28, 32, 38, 41, 53, 54

[56] Yarusevych, S. and M. S. H. Boutilier, *Vortex Shedding Characteristics of a NACA 0018 Airfoil at Low Reynolds Numbers*. In *40th AIAA Fluid Dynamics Conference and Exhibit, Chicago, Illinois*, vol. 2010-4628, 2010. 27, 67, 69, 75, 76, 79

[57] Yarusevych, S., P. E. Sullivan and J. G. Kawall, *On Vortex Shedding from an Airfoil in Low Reynolds Number Flows*. Journal of Fluid Mechanics, 632:215–271, 2009. 27, 69, 75, 76, 79

[58] Schepers, J. G., A. Curves, S. Oerlemans, K. Braun, A. Herrig, W. Würz, A. Mantesanz, L. Garcillán, M. Fisher, K. Kögler and T. Maeder, *Silent Rotors by Acoustic Optimisation*. In *Second International Meeting on Wind Turbine Noise, Lyon, France*, 2007. 28

[59] Moriarty, P. and P. Migliore, *Semi-Empirical Aeroacoustic Noise Prediction Code for Wind Turbines*. Technical Report TP-500-34478, NREL, 2003. 29

[60] Raffel, M., C. E. Willert and J. Kompenhans, *Particle Image Velocimetry*. Berlin: Springer, 1998. 30

[61] Schröder, A., U. Dierksheide, J. Wolf, M. Herr and J. Kompenhans, *Investigation on Trailing-Edge Noise Sources By Means of High-Speed PIV*. In *12th International Symposium on Applications of Laser Techniques to Fluid Mechanics, Lisbon, Portugal*, 2004. 30

[62] Shannon, D. W., S. C. Morris and T. J. Mueller, *Trailing Edge Flow Physics and Acoustics*. In *11th AIAA/CEAS Aeroacoustics Conference, Monterey, California*, vol. 2005-2957, 2005. 30

[63] Sperandei, B., *The Application of Particle Image Velocimetry in a Small Scale Wind Tunnel*. Master's thesis, University of Waterloo, 2002. 31, 32, 78

[64] Mehta, R. D., *The Aerodynamic Design of Blower Tunnels With Wide-Angle Diffusers*. Progress in Aerospace Science, 18:59–120, 1977. 32

[65] Bale, A. E., *A Laser Doppler Anemometry Study of The Effects of Flow Conditioning in a Small-Scale Wind Tunnel*, 2009, University of Waterloo ME 770. 32

[66] Runstadler Jr., P. W., F. X. Dolan and R. C. Dean Jr., *Diffuser Data Book*. Technical note, Creare Incorporated, 1975. 33

[67] Mehta, R. D. and P. Bradshaw, *Design Rules for Small Low-Speed Wind Tunnels*. Aeronautical Journal of the Royal Aeronautical Society, 73:443–449, 1979. 34, 35, 36

[68] Groth, J. and A. V. Johansson, *Turbulence Reduction by Screens*. Journal of Fluid Mechanics, 197:139–155, 1988. 35, 36

[69] Somers, D. M., *The S822 and S823 Airfoils*. Subcontractor Report 500-36342, NREL, 2005. 40

[70] Somers, D. M., *The S833, S834, and S835 Airfoils*. Subcontractor Report 500-36340, NREL, 2005. 40

[71] Selig, M. S., J. J. Guglielmo, A. P. Broeren and P. Giguère, *Summary of Low-Speed Airfoil Data*, vol. 1. Virginia Beach: SoarTech Publications, 1995, http://www.ae.illinois.edu/m-selig/pd.html. 41, 42, 43

[72] Rockwell, K., *Nikon 50mm f/1.8 D*, 2010, `http://www.kenrockwell.com/nikon/5018daf.htm`, accessed: November 18, 2010. 45

[73] Rockwell, K., *Nikon 85mm f/1.4 AI-s*, 2008, `http://www.kenrockwell.com/nikon/85mm-f14.htm`, accessed: November 18, 2010. 46

[74] Bahr, C., T. Yardibi, F. Liu and L. Cattafesta, *An Analysis of Different Measurement Techniques for Airfoil Trailing Edge Noise*. In *14th AIAA/CEAS Aeroacoustics Conference, Vancouver, British Columbia*, vol. 2008-2957, 2008. 54

[75] Remillieux, M. C., *Aeroacoustic Study of a Model-Scale Landing Gear in a Semi-Anechoic Wind-Tunnel*. Master's thesis, Virginia Polytechnic Institute and State University, 2007. 54

[76] Dougherty, R. P. Spiral-Shaped Array for Broadband Imaging, US Patent: 5838284, 1998. 55, 98

[77] Underbrink, J. R. Circularly Symmetric, Zero Redundancy, Planar Array Having Broad Frequency Range Applications, US Patent: 6205224 B1, 2001. 55

[78] Bale, A. E., *Design of a MEMS Microphone Arrays*. Master's thesis, University of Waterloo, 2011. 55

[79] Soderman, P. T. and C. S. Allen, *Aeroacoustic Measurements*, chap. Microphone Measurements In and Out of Airstream, 1–58. Berlin: Springer, 2002. 56

[80] Jaeger, S. M., W. C. Horne and C. S. Allen, *Effect of Surface Treatment on Array Microphone Self-Noise*. In *6th AIAA/CEAS Aeroacoustics Conference, Lahaina, Hawaii*, vol. 2000-1937, 2000. 56

[81] Arnold, D. P., *A MEMS-Based Directional Acoustic Array for Aeroacoustic Measurements*. Master's thesis, University of Florida, 2001. 57

[82] Yarusevych, S., P. E. Sullivan and J. G. Kawall, *Effect of Acoustic Excitation Amplitude on Airfoil Boundary Layer and Wake Development*. AIAA, 45(4):760–771, 2007. 74

[83] Callister Jr., W. D., *Materials Science and Engineering an Introduction*. New York: John Wiley & Sons, Inc., 6th ed., 2003. 82

[84] Moffat, R. J., *Describing the Uncertainties in Experimental Results*. Experimental Thermal and Fluid Science, 1:3–17, 1988. 95

[85] White, F. M., *Fluid Mechanics*. Toronto: McGraw-Hill, 5th ed., 2003. 95, 96

Appendices

Appendix A

Acoustic Spectra

Shown below are all the acoustic spectra at $\alpha = 0°$ for U_0 =15–35 m/s at 1 m/s increments. The vertical axis is measured in decibels and each plot is shifted for clarification.

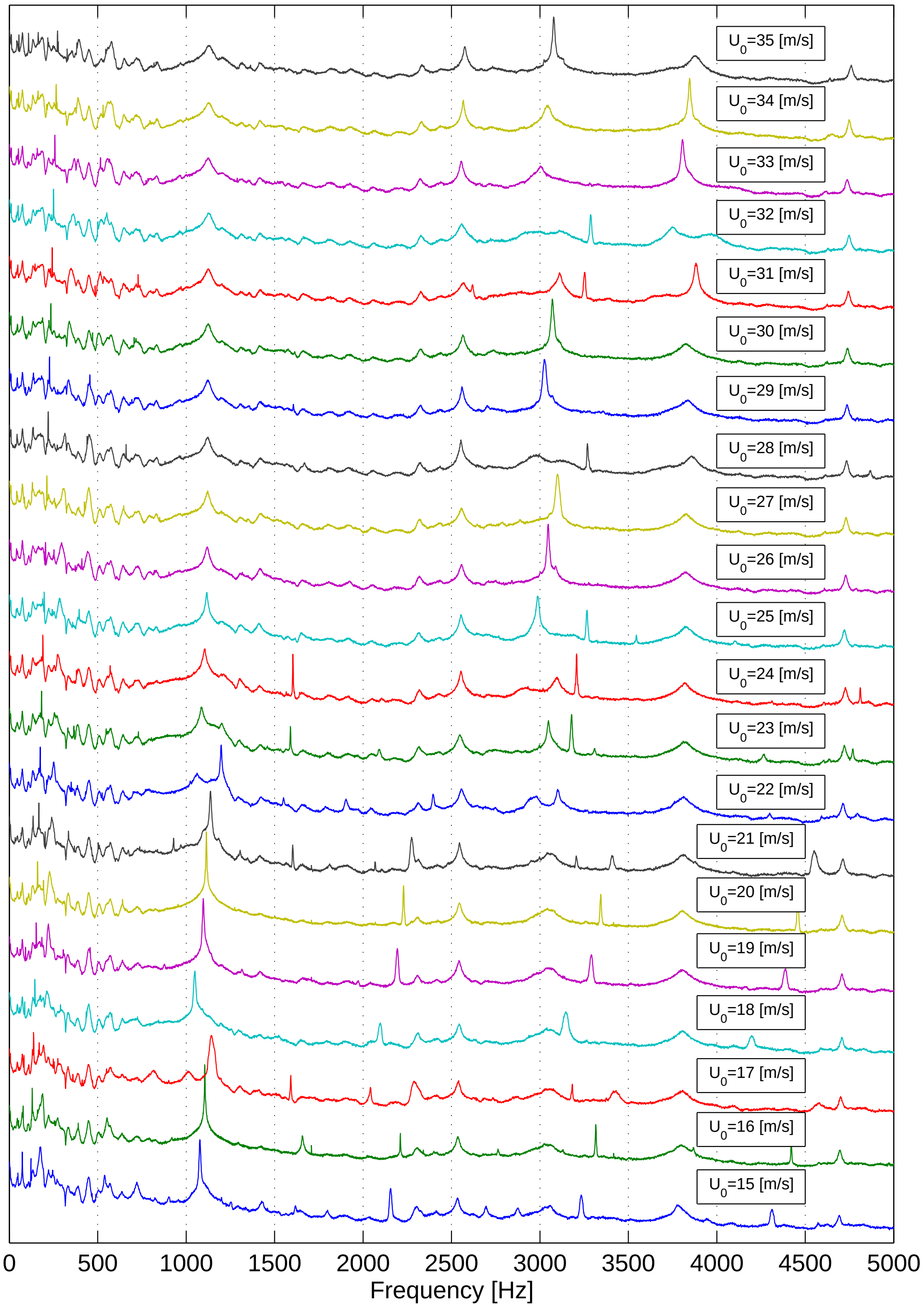

Figure A.1: Sound pressure level narrowband spectra at $\alpha = 0^\circ$ for U_0 =15–35 m/s at 1 m/s increments

Appendix B

Boundary Corrections

The flow in a closed test section wind tunnel is restricted by the walls and because of this the flow around the airfoil is accelerated. Corrections to the freestream velocity must be made to account for this velocity increase. The following correction method is taken from Barlow et al. [9]. For two-dimensional airfoil tests the freestream velocity must be corrected for wake blockage and solid blockage. The solid blockage correction factor, ε_{sb} is defined by:

$$\varepsilon_{sb} = \frac{K_1\,(model\,volume)}{C^{3/2}} \tag{B.1}$$

where $K_1 = 0.74$ and C is the test section area. The wake blockage correction factor, ε_{wb}, is defined by:

$$\varepsilon_{wb} = \frac{{}^{c}/_{h}}{4} c_{du} \tag{B.2}$$

where c_{du} is the uncorrected drag coefficient taken as $c_{du} \approx 0.03$ from Selig and McGranahan [28]. For the S822 airfoil used, $\varepsilon_{sb} = 0.01$ and $\varepsilon_{wb} = 0.003$. The corrected freestream velocity, $U_{0,c}$, is given by:

$$U_{0,c} = U_0\,(1 + \varepsilon_{sb} + \varepsilon_{wb}) \tag{B.3}$$

where U_0 is the nominal, uncorrected freestream velocity measured with an empty test section. The corrected freestream velocity is used to calculate the Reynolds number, Re_c, and Strouhal number, St_{d^*}.

Appendix C

Error Analysis

An error analysis is performed to determine the error associated with the measured and derived quantities. Sources of error can be divided into two categories, "bias" errors and "precision" errors [31, 84]. Bias errors are fixed and usually associated with the measurement device or measurement setup. Precision errors are random and associated with the measurement of a stochastic process such as: velocity, temperature or pressure. The propagation of precision error through a calculation is calculated with the addition of composite error terms using the root-sum-square (RSS) method. Using the RSS method, the total error of the Reynolds number, ΔRe_c, is given by:

$$\Delta Re_c = \sqrt{\left(\Delta\rho\frac{\partial Re_c}{\partial\rho}\right)^2 + \left(\Delta U_0\frac{\partial Re_c}{\partial U_0}\right)^2 + \left(\Delta\mu\frac{\partial Re_c}{\partial\mu}\right)^2} \tag{C.1}$$

$$\Delta Re_c = Re_c\sqrt{\left(\frac{\Delta\rho}{\rho}\right)^2 + \left(\frac{\Delta U_0}{U_0}\right)^2 + \left(\frac{\Delta\mu}{\mu}\right)^2} \tag{C.2}$$

where $\Delta\rho$ is the precision error on the density, ΔU_0 is the precision error on the freestream velocity, and$\Delta\mu$ is the precision error on the viscosity.

The density, ρ, of the air in the wind is defined by the following equation from White [85]:

$$\rho = \frac{P_0}{RT} \tag{C.3}$$

where $P_0 = 97200$ Pa is the atmospheric pressure, $R = 287$ J/(kg·K) is the specific gas constant, and T is the temperature in Kelvin inside the wind tunnel. Also using the RSS method, the precision error on the density, $\Delta\rho$, is defined by:

$$\Delta\rho = \sqrt{\left(\Delta P_0\frac{\partial\rho}{\partial P_0}\right)^2 + \left(\Delta T\frac{\partial\rho}{\partial T}\right)^2} = \rho\sqrt{\left(\frac{\Delta P_0}{P_0}\right)^2 + \left(\frac{\Delta T}{T}\right)^2} \tag{C.4}$$

where ΔP_0 is the error on the atmospheric pressure measurement and ΔT is the error on the temperature measurement.

The temperature was measured with a K-type thermocouple and was measured to vary by ±1 K during a test at a specific velocity. Using a mercury manometer, the atmospheric pressure was measured before and after a series of tests and was found to vary by ±200 Pa.

The total error of the freestream velocity measurement is composed of two dominant error sources. The maximum 95% mean confidence interval calculated by the BSA Flow Software [32] is approximately 0.002 m/s. Another precision error is due to the variability of the wind tunnel caused by leaks and clogging of the turbulence reduction screens. Based on the maximum variability between the two wind tunnel calibration tests this precision error is estimated at 0.13 m/s. Bias errors associated with the LDA are due to the uncertainty in beam separation distance which in turn affects the fringe spacing; this error is considered to be negligible [31]. The uncertainty in the rotational alignment of the probe also causes a bias error. The probe's rotation has an estimated precision of ±0.5° resulting in a negligible effect on the velocity measurement. The total error of the freestream velocity is calculated to be $\Delta U_0 = 0.13$ [m/s]. It should be noted that the maximum 95% mean confidence interval in the airfoil wake is much larger and can be up to 2.5 m/s.

Using a power law from White [85], the dynamic viscosity of the air in the wind tunnel, μ is defined by:

$$\mu = \mu_0 \left(\frac{T}{T_0}\right)^{0.7} \tag{C.5}$$

where $\mu_0 = 1.71 \times 10^{-5}$ Pa·s is the reference dynamic viscosity, $T_0 = 273$ K is the reference temperature. The precision error on the viscosity, $\Delta\mu$, is given by:

$$\Delta\mu = \Delta T \frac{\partial \mu}{\partial T} = 0.7 \Delta T \frac{\mu_0}{T_0} \left(\frac{T_0}{T}\right)^{0.3} \tag{C.6}$$

Using the RSS method, the total error of the Strouhal number, ΔSt_{d^*}, is given by:

$$\Delta St_{d^*} = \sqrt{\left(\Delta f_s \frac{\partial St_{d^*}}{\partial f_s}\right)^2 + \left(\Delta d^* \frac{\partial St_{d^*}}{\partial d^*}\right)^2 + \left(\Delta U_0 \frac{\partial St_{d^*}}{\partial U_0}\right)^2} \tag{C.7}$$

$$\Delta St_{d^*} = St_{d^*} \sqrt{\left(\frac{\Delta f_s}{f_s}\right)^2 + \left(\frac{\Delta d^*}{d^*}\right)^2 + \left(\frac{\Delta U_0}{U_0}\right)^2} \tag{C.8}$$

where Δf_s is the error of the shedding frequency estimate and Δd^* is the error of the d^* measurement. The shedding frequency is calculated from curve fit of the LDA spectrum and because of this precision error is estimated at 10 Hz.

Table C.1: Summary of errors

Variable	Absolute error	Percent error
ΔP_0	200 Pa	0.21
ΔT	1 K	0.34
$\Delta \rho$	4.5×10^{-3} kg/m^3	0.39
$\Delta \mu$	4.2×10^{-8} Pa·s	0.24
ΔU_0	0.13 m/s	1.3
ΔRe_c	650	1.4
Δd^*	0.54 mm	12
Δf_s	10 Hz	0.92
ΔSt_{d^*}	0.03	12

The quantity d^* is the measured distance between RMS peaks in the wake. Therefore the error associated with d^* is equal to twice the error of the location of each point. The error associated with d^* is due to three error sources. Firstly, the bias error of the LDA traverse in the Z direction is estimated at 0.01 mm [32]. The precision error due to the relative movement between the LDA system and the wind tunnel caused by random vibrations of the wind tunnel is estimated at 0.1 mm. Lastly there is precision error due to the calculation of d^* from the curve fit of the RMS freestream velocity wake profiles, which is estimated at 0.25 mm. Using the RSS method, $\Delta d^* \approx 0.54$ [mm]. The resulting total error on the Strouhal number is $\Delta St_{d^*} = 0.03$. A summary of the maximum errors over the velocity range is given in Table C.1.

Appendix D

Beamforming Code

The following code is a series of functions written to apply the beamforming algorithm. A description of each “m-file” function is as follows.

beamforming.m – Main function that calls other functions which create the array coordinates, generate the signals or read them from data files. Beamforming algorithm is done in this function.

LinearArray.m – Creates linear array coordinates.

RandomCircularArray.m – Creates random array coordinates within a prescribed radius.

ConcentricCircleArray.m – Creates concentric circle array coordinates.

DoughertySpiral.m – Creates array coordinates based on the Dougherty spiral [76].

UnderbrinkSpiralArray.m – Creates array coordinates based on the Underbrink “Equal Area Aperture Array”.

PredefinedArray.m – Reads array coordinates and microphone sensitivities from a data file.

StretchMicrophoneCoordinates.m – Stretches current microphone array coordinates in prescribed directions.

GenerateSignals.m – Generates time-delayed acoustic signals for each microphone.

ReadSignals.m – Reads acoustic signals stored in a National Instruments .tdms binary file.

```
%----------------------Start beamforming.m
clear all
tic
c_0=340000;   % Speed of sounds [mm/s]
T_b =  2^13 ;                           %Samples per block, block length
K = 50;                                 %Number of blocks
T_tot=K*T_b;                            %Total number of samples
Fs=5E4;                                 %Sampling frequency
L=T_tot/Fs;                             %Length of signal in seconds
s_f=8000;                               %Scanning frequency
t=((0:T_tot-1)/Fs)';          %Time in seconds for m_0 channels
%---------------Start of Array Type
%LinearArray  %Call LinearArray.m array coordinate generator
%RandomCircularArray  %Call RandomCircularArray.m array coordinate generator
%ConcentricCircleArray  %Call ConcentricCircleArray.m array coordinate generator
%DoughertySpiralArray  %Call DoughertySpiralArray.m array coordinate generator
UnderbrinkSpiralArray  %Call UnderbrinkSpiralArray.m array coordinate generator
%PredefinedArray  %Call PredefinedArray.m which reads array coordinate file
%StretchMicrophoneCoordinates  %Call StretchMicrophoneCoordinates.m to apply stretching transform
%---------------End of Array Type

%-----------------------Start Signal Generation
source_f=8000;
xs_source_locs=[0,0,1000;500,500,1000]; % Location of sources [x1,y1,z1; x2,y2,z3;...;xn,yn,zn]
%xs_source_locs=horzcat(zeros(27,1),(-97.5:7.5:97.5)',100*ones(27,1));
GenerateSignals  %Call SignalGeneration.m to generate signals
%--------------------End Signal Generation

%-----------------------Start Read Signals
% xs_source_locs=[0,0,1000]; % Location of scanning plane center [x,y,z]
% ReadSignals  %Call ReadSignals.m which reads .tdms binary data file
%-----------------------End Read Signals

s_b=zeros(length(t)/K,m_0,K);  % Initialize complete blocks microphone signal matrix
for c=1:K
    s_b(:,:,c)=s(length(t)/K*(c-1)+1:length(t)/K*c,:);   %Reshape matrix into 3 dimensions where 3rd dimension is the block number
end
clear s % Clear s to free memory

window=hamming(length(s_b),'periodic'); %Hamming window
w_s=mean(window);                       %Hamming window weighting constant
s_b=s_b.*repmat(window,[1,m_0,K]);        %Apply Hamming window to all signal blocks

zs=xs_source_locs(1,3);   % Perpendicular distance between source plane and microphone plane [mm]
start_xs=-500; % Starting x-coordinate of source plane [mm]
inc_xs=10;     % X Increment of source location
end_xs=500;     % Ending x-coordinate of source plane  [mm]
start_ys=-500; % Starting y-coordinate of source plane  [mm]
inc_ys=10;     % Y Increment of source location
end_ys=500;     % Ending y-coordinate of source plane [mm]
n_xgrid=(end_xs-start_xs)/inc_xs+1; % Number of grid points in x
n_ygrid=(end_ys-start_ys)/inc_ys+1; % Number of grid points in y
N=n_xgrid*n_ygrid; % Total number of grid points

xs=repmat((start_xs:inc_xs:end_xs)',n_ygrid,1); % X-coordinates as a column vector
ys=reshape(repmat((start_ys:inc_ys:end_ys)',1,n_xgrid)',N,1); % Y-coordinates as a column vector

rc=(xs.^2+ys.^2+zs.^2).^0.5;   % Distance between source plane grid points and center of array
dx=repmat(xs,1,m_0)-repmat(m(:,1)',N,1);
dy=repmat(ys,1,m_0)-repmat(m(:,2)',N,1);
dz=repmat(zs,N,m_0)-repmat(m(:,3)',N,1);
rm=(dx.^2+dy.^2+dz.^2).^0.5;  % Distance between microphones and source plane grid points

NFFT = 2^nextpow2(T_b); % Next power of 2 from length of T_b
P = fft(s_b,NFFT)/T_b;  % Will zero-pad if necessary
P_ss=2*P(1:NFFT/2,:,:);  %P_ss is the single sided complex power spectrum
clear P
freq = Fs/2*linspace(0,1,NFFT/2);

%Pabs=abs(P(1:NFFT/2,:,:)); % Get magnitude of single sided power spectrum
%Pabs(2:size(Pabs,1),:,:)=2*Pabs(2:size(Pabs,1),:,:);  %Multiply by 2 to get true magnitude except for DC component

%---------------- Set Start and End Frequencies for 1/3 octave band
start_f=s_f/2^(1/24);  % Lower end of 1/3 octave band
end_f=s_f*2^(1/24);    % Upper end of 1/3 octave band
start_f_loc=find(freq<=start_f, 1,'last' );  % Returns the vector address corresponding to the first frequency below start_f
```

```
end_f_loc=find(freq>=end_f, 1 );  % Returns the vector address corresponding to the first frequency above end_f
%---------------- End Set Start and End Frequencies for scanning frequency band

%------------------Set single scanning frequency equal to s_f
% start_f_loc=find(abs(freq-s_f)==min(abs(freq-s_f)));  % Find the frequency location closest to that corresponding to s_f
% end_f_loc=start_f_loc;  % Set end_f_loc=start_f_loc if we want to scan for a single frequency
% start_f=s_f;
% end_f=s_f;
%------------------End Set single scanning frequency equal to s_f

Y=complex(ones(N,end_f_loc-start_f_loc+1),ones(N,end_f_loc-start_f_loc+1));  % Initialize output matrix

for f_loc=start_f_loc:end_f_loc  % f_loc is the current frequency row number (location) in freq
%---------Cross Spectral Matrix
G=zeros(m_0,m_0,K);  % Initialize cross spectral matrix
for c=1:K
    G(:,:,c)=repmat(P_ss(f_loc,:,c)',[1,m_0]).*repmat(P_ss(f_loc,:,c),[m_0,1]);  %Cross-spectral matrix for each block K where ".'" is the unconjugated ↙
complex transpose
end
G=sum(G,3)/(w_s*K);  %Average cross-spectral matrix over K blocks
G_f=zeros(m_0,m_0,end_f_loc-start_f_loc+1);  % Initialize averaged cross spectral matrix
G_f(:,:,f_loc-start_f_loc+1)=tril(G,-1)+triu(G,1); %Remove diagonal elements

clear G  % Clear G to free memory
%--------------End Cross Spectral Matrix

e=rm./repmat(rc,1,m_0).*(exp(1).^(2*pi*1i*freq(f_loc)*rm/c_0));  % Steering vector matrix [position (left to right then down), microphone]
%e=(exp(1).^(2*pi*1i*freq(f_loc)*rm/c_0));  % No weighting Steering vector matrix [position (left to right then down), microphone]

for c=1:N
    Y(c,f_loc-start_f_loc+1)=conj(e(c,:))*G_f(:,:,f_loc-start_f_loc+1)*e(c,:).'/(m_0^2-m_0);
end
(f_loc-start_f_loc)/(end_f_loc-start_f_loc)*100
end

Y_mag=sqrt(abs(Y));   %Y comes out as a real number with imaginary coefficients of 0.  Sqrt returns [Pa]
Y_rms_sum=sqrt(sum(Y_mag.^2,2));  %Add pressure from discrete frequencies in 1/3 octave band using rms summed method
Y_dB=20*log10(sqrt(0.5)*Y_rms_sum/20E-6);  %Convert output to decibels and average over frequencies
Y_dB_exp=Y_dB;
Y_dB=reshape(Y_dB,n_xgrid,n_ygrid)';  % Reshape into matrix form

%---------Calculate Beamwidth
%contourc returns indices of contour.  Indices must be converted to actual [x,y] coordinates
bw_contour=contourc(Y_dB,[max(max(Y_dB))-3 max(max(Y_dB))-3]); % Get contour indices at -3dB from peak
x_bw_coord=(bw_contour(1,2:length(bw_contour))-1)*inc_xs+start_xs; % Get actual x-coordinates of contour -3dB from peak
y_bw_coord=(bw_contour(2,2:length(bw_contour))-1)*inc_ys+start_ys; % Get actual y-coordinates of contour -3dB from peak
peak_indice=contourc(Y_dB,[max(max(Y_dB)) max(max(Y_dB))]);% Get indices of peak
bw=sqrt(polyarea(x_bw_coord, y_bw_coord)*4/pi);  % Calculate beamwidth as diameter of circle equivalent in area to area enclosed by -dB contour
%---------End Calculate Beamwidth

% Shift Y_dB so the center of a mesh square corresponds to a value in Y_dB not the vertex,
Y_dB_plot=horzcat(vertcat(Y_dB,zeros(1,n_xgrid)),zeros(n_ygrid+1,1));  % Add a row and column of zeros to the right and bottom of Y_db
x_plot_coord=(start_xs-inc_xs/2:inc_xs:end_xs+inc_xs/2);
y_plot_coord=(start_ys-inc_ys/2:inc_ys:end_ys+inc_ys/2);

figure
surf(x_plot_coord,y_plot_coord,Y_dB_plot);  % Plot noise map
shading interp;
axis equal;
axis tight;
alpha(0.75);
box on;
annotation(gcf,'textbox','FitBoxToText','on','Position',[0.48,0.82,0.1,0.1],'linestyle','none','String',[num2str(round(start_f)), ' Hz - ',num2str(round(end_f)), ' ↙
Hz']);
dB_down=15; %Set dB level below peak
set(gca,'ZLim',[max(max(Y_dB))-dB_down max(max(Y_dB))]);
caxis([max(max(Y_dB))-dB_down max(max(Y_dB))]);
hold on;
h2=scatter3(m(:,1),m(:,2),m(:,3)+max(max(mean(Y_dB,3))),'.','sizedata',500,'markeredgecolor','black','markerfacecolor','black');  % Plot microphone layout
view(0,90);
colorbar('location','south');
toc
%----------------------End beamforming.m
```

22/01/11 9:45 PM C:\Documents and Settings\Administrator\My Documents\Master's Work\Phased Array Stuff\LinearArray.m 1/1

```
%---------------LinearArray.m
m_0=16;
m_x=[-70,-40,-20,-5,5,20,40,70,-70,-40,-20,-5,5,20,40,70]';
m_y=vertcat(-10*ones(8,1),10*ones(8,1));
m_z=zeros(16,1);
m=horzcat(m_x,m_y,m_z);

% m_0=8;
% m_x=[-70,-40,-20,-5,5,20,40,70]';
% m_y=zeros(m_0,1);
% m_z=zeros(m_0,1);
% m=horzcat(m_x,m_y,m_z);
%---------------End LinearArray.m
```

22/01/11 9:45 PM C:\Documents and Settings\Administrator\My Documents\Master's Work\Phased Array Stuff\RandomCircularArray.m 1/1

```
%---------------Start RandomCircularArray.m
r_max= 70; %maximum radius [mm]
m_0=29; %number of microphone
m=horzcat(rand(m_0,1)*r_max.*cos(rand(m_0,1)*2*pi),rand(m_0,1)*r_max.*sin(rand(m_0,1)*2*pi),zeros(m_0,1));
%---------------End RandomCircularArray.m
```

22/01/11 9:45 PM C:\Documents and Settings\Administrator\My Documents\Master's Work\Phased Array Stuff\ConcentricCircleArray.m 1/1

```
%----------------Start ConcentricCircleArray.m
r_max=70; % Maximum array radius [mm]
N_ring=2;  % Number of concentric microphone rings
N_mic=31;  % Number of microphones per ring
m_0=N_ring*N_mic;  % Total number of microphones
theta_circ=(0:2*pi/N_mic:2*pi*(1-1/N_mic))';

m=zeros(N_ring*N_mic,3);  % Initialize microphone coordinate matrix
r_circ=r_max./(2.^((1:N_ring)-1));  % Radius of each circular ring.  Each radius is half the radius of the next largest circle.

for c=1:N_ring
    m((c-1)*N_mic+1:c*N_mic,:)=horzcat(r_circ(c)*cos(theta_circ),r_circ(c)*sin(theta_circ),zeros(N_mic,1));
end

m=vertcat(m,[0,0,0]);  % Add microphone at center of the array [0,0,0]
m_0=size(m,1);  % Total number of microphones
%----------------End ConcentricCircleArray.m
```

22/01/11 9:46 PM C:\Documents and Settings\Administrator\My Documents\Master's Work\Phased Array Stuff\DoughertySpiralArray.m 1/1

```
%-------------------Start DoughertySpiralArray.m
%-------------------Dougherty Spiral Microphone Coordinates from Dougherty, "Aeroacoustic Measurements"
N_spiral=9;  % Number of spirals or number of microphones per ring
N_ring=3;  % Number of microphones per spiral or number or rings of microphones
r_0 = 15; %Radius of array at theta=0 [mm]
r_max = 70; %Maximum array radius [mm]
v = 75*pi/180; %Spiral angle [rad]

h=cot(v);
theta_max=log(r_max/r_0)/h;
l_max = (r_0*(1+h^2)^0.5)/h*(exp(h*theta_max)-1);
d_l=l_max/(N_ring-1);

l_m=d_l*(0:N_ring-1);
m_polar=zeros(N_ring*N_spiral,3);
for c=1:N_spiral
    theta_m=log(1+h*l_m./(r_0*(1+h^2)^0.5))/h;
    radius_m = r_0*exp(h*theta_m);
    m_polar((c-1)*N_ring+1:c*N_ring,:)=horzcat(radius_m',theta_m'+(c-1)*2*pi/N_spiral,zeros(N_ring,1));
end
m=horzcat(m_polar(:,1).*cos(m_polar(:,2)),m_polar(:,1).*sin(m_polar(:,2)),m_polar(:,3));
m=vertcat(m,[0,0,0]);  % Add microphone at center of the array [0,0,0]
m_0=size(m,1); % Total number of microphones
%-----------------End DoughertySpiralArray.m
```

22/01/11 9:46 PM C:\Documents and Settings\Administrator\My Documents\Master's Work\Phased Array Stuff\UnderbrinkSpiralArray.m 1/1

```
%-------------------UnderbrinkSpiralArray.m
%-------------------Underbrink Equal Aperture Spiral Microphone Coordinates from "Aeroacoustic Measurements"
N_spiral=5;  % Number of spirals or number of microphones per ring
N_ring=6;  % Number of microphones per spiral or number or rings of microphones
r_0 = 35; %Radius of array at theta=0 [mm]
r_mNt = 470; %Maximum array radius [mm]
v = 68*pi/180; %Spiral angle [rad]

Nt=N_ring-1;
r_Nt=max(roots([-1/Nt -4*r_mNt*sqrt(1-1/Nt) 4*r_mNt^2]));
r_N(1:Nt)=(r_Nt^2*(1:Nt)./Nt).^0.5;
r_N=horzcat(0,r_N,0);
r_m(1)=r_0;
r_m(2:N_ring)=(r_N(2:Nt+1)+r_N(1:Nt))/2;
theta_ring=tan(v)*log(r_m/r_0);
delta_theta=2*pi/N_spiral;

theta_mic=zeros(N_spiral*N_ring,1);
r_mic=zeros(N_spiral*N_ring,1);
for c=1:N_ring
    theta_mic((c-1)*N_spiral+1:c*N_spiral)=((1:N_spiral)'-1)*delta_theta+theta_ring(c);
    r_mic((c-1)*N_spiral+1:c*N_spiral)=ones(N_spiral,1)*r_m(c);
end
m=horzcat(r_mic.*cos(theta_mic),r_mic.*sin(theta_mic),zeros(N_spiral*N_ring,1));

%m=vertcat(m,[0,0,0]);  % Add microphone at center of the array [0,0,0]
m_0=size(m,1); % Total number of microphones
%-----------------End Underbrink Equal Aperture Spiral Microphone Coordinates
%-------------------End UnderbrinkSpiralArray.m
```

22/01/11 9:47 PM C:\Documents and Settings\Administrator\My Documents\Master's Work\Phased Array Stuff\PredefinedArray.m 1/1

```
%------------------Start PredefinedArray.m
mic_coord_data=csvread('MicDataBoard4.csv');  %Get array data [mic number, x, y, z, sensitivity]
m=mic_coord_data(:,2:4);  %Get array coordinates [x,y,z]
m_0=size(m,1); % Total number of microphones
%------------------End PredefinedArray.m
```

22/01/11 9:47 PM C:\Documents and Settings\Administrator\My Documents\Master's Work\Phased Array Stuff\StretchMicrophoneCoordinates.m 1/1

```
%------------------StretchMicrophoneCoordinates.m
Ax=1.5;  % X-coordinate stretch factor
Ay=1;    % Y-coordinate stretch factor
Az=1;    % Z-coordinate stretch factor (should never be used)
m=m*[Ax,0,0;0,Ay,0;0,0,Az];
%------------------End StretchMicrophoneCoordinates.m
```

22/01/11 9:48 PM C:\Documents and Settings\Administrator\My Documents\Master's Work\Phased Array Stuff\GenerateSignals.m 1/1

```
%----------------------GenerateSignals.m
s_m=zeros(length(t),size(xs_source_locs,1));  % Initialize microphone signal source matrix
s=zeros(length(t),m_0);  % Initialize complete microphone signal matrix
rm_s=zeros(m_0,size(xs_source_locs,1)); % Initialize distance from source location to microphone matrix
phi=zeros(m_0,size(xs_source_locs,1)); % Initialize time delay matrix

A_rms=1;  %Pascal amplitude, rms value
for c=1:m_0
    for d=1:size(xs_source_locs,1)
        rm_s(:,d)=((m(:,1)-xs_source_locs(d,1)).^2+(m(:,2)-xs_source_locs(d,2)).^2+(m(:,3)-xs_source_locs(d,3)).^2).^0.5;  %Distance from source "d" ↙
location to microphone
        phi(:,d)=(rm_s(:,d))/c_0; % Time delays for source "d".  All sources are in phase.

        s_m(:,d)=A_rms*sqrt(2)*sin(2*pi*s_f*(t-phi(c,d)));  %multiply by sqrt(2) to convert rms amplitude to peak amplitude
    end
    s(:,c)=sum(s_m,2);%+2*randn(size(t)); % Modelled microphone signals with channel noise randn(size(t))
end

%Five signals at about 5kHz superimposed
%s(:,c)=2*sin(2*pi*s_f*(t-phi_s1(c)))+0.2*sin(2*pi*(s_f-10)*(t-phi_s1(c)))+1.6*sin(2*pi*(source_f-5)*(t-phi_s1(c)))+0.2*sin(2*pi*(source_f+10)*(t-phi_s1 ↙
(c)))+1.6*sin(2*pi*(source_f+5)*(t-phi_s1(c)))+broadband+randn(size(t)); % Modelled microphone signals

clear s_m   % Clear s_m to free memory
%----------------------End GenerateSignals.m
```

```
%-------------------Start ReadSignals.m
%-------------------Start of Read TDMS file from National Instruments
clear chanvals;  %Added by Stephen Orlando, use to be located after plot(chanvals)

clc;
%Check if the paths to 'nilibddc.dll' and 'nilibddc_m.h' have been
%selected.  If not, prompt the user to browse to each of the files.
if exist('NI_TDM_DLL_Path','var')==0
    %[dllfile,dllfolder]=uigetfile('*dll','Select nilibddc.dll'); %remove prompt
    dllfolder=['TDMS to MATlab\MATLAB TDM Example\dev\bin'];
    dllfile=['nilibddc.dll'];
    NI_TDM_DLL_Path=fullfile(dllfolder,dllfile);
end
if exist('NI_TDM_H_Path','var')==0
    %[hfile,hfolder]=uigetfile('*h','Select nilibddc_m.h');  %remove prompt
    hfolder=['TDMS to MATlab\MATLAB TDM Example\dev\include'];
    hfile=['nilibddc_m.h'];
    NI_TDM_H_Path=fullfile(hfolder,hfile);
end

%Prompt the user to browse to the path of the TDM or TDMS file to read.
[filepath,filefolder]=uigetfile({'*.tdm';'*.tdms'},'Select TDM or TDMS File');
Data_Path=fullfile(filefolder,filepath);
[pathstr, name, ext, versn] = fileparts(Data_Path);

%Apply the appropriate file type to 'ftype', depending on whether a TDM or
%TDMS file was selected.  Here, 'ftype' is used in the 'DDC_OpenFileEx' function.
if strcmp(ext,'.tdms')
    ftype='TDMS';
else
    ftype='TDM';
end

%Load nilibddc.dll (Always call 'unloadlibrary('nilibddc')' after finished using
%the library.)
loadlibrary(NI_TDM_DLL_Path,NI_TDM_H_Path);

%Open the TDM or TDMS file (Read Only) (Always call 'DDC_CloseFile' after finished creating or
%reading a file.)
pfile = libpointer('int32Ptr', 0);
calllib('nilibddc','DDC_OpenFileEx',Data_Path,ftype,1,pfile);

%Read and Display File Name
DDC_FILE_NAME=libpointer('stringPtr','name');
pfilenamelen=libpointer('uint32Ptr',0);
%Get the length of the 'DDC_FILE_NAME' string property
err=calllib('nilibddc','DDC_GetFileStringPropertyLength',pfile.Value,DDC_FILE_NAME,pfilenamelen);
if err==0 %Only proceed if File Name is found
    %Initialize a string of the length of the file name
    pfilename=libpointer('stringPtr',blanks(pfilenamelen.Value));
    calllib('nilibddc','DDC_GetFileProperty',pfile.Value,DDC_FILE_NAME,pfilename,pfilenamelen.Value+1);
    disp(['File Name: ' pfilename.Value]);
end

%Read and Display File Description
DDC_FILE_DESCRIPTION=libpointer('stringPtr','description');
pfiledesclen=libpointer('uint32Ptr',0);
%Get the length of the 'DDC_FILE_DESCRIPTION' string property
err=calllib('nilibddc','DDC_GetFileStringPropertyLength',pfile.Value,DDC_FILE_DESCRIPTION,pfiledesclen);
if err==0 %Only proceed if File Description is found
    %Initialize a string of the length of the file description
    pfiledesc=libpointer('stringPtr',blanks(pfiledesclen.Value));
    calllib('nilibddc','DDC_GetFileProperty',pfile.Value,DDC_FILE_DESCRIPTION,pfiledesc,pfiledesclen.Value+1);
    disp(['File Description: ' pfiledesc.Value]);
end

%Read and Display File Title
DDC_FILE_TITLE=libpointer('stringPtr','title');
pfiletitlelen=libpointer('uint32Ptr',0);
%Get the length of the 'DDC_FILE_TITLE' string property
err=calllib('nilibddc','DDC_GetFileStringPropertyLength',pfile.Value,DDC_FILE_TITLE,pfiletitlelen);
if err==0 %Only proceed if File Title is found
    %Initialize a string of the length of the file title
    pfiletitle=libpointer('stringPtr',blanks(pfiletitlelen.Value));
    calllib('nilibddc','DDC_GetFileProperty',pfile.Value,DDC_FILE_TITLE,pfiletitle,pfiletitlelen.Value+1);
    disp(['File Title: ' pfiletitle.Value]);
```

```
end

%Read and Display File Author
DDC_FILE_AUTHOR=libpointer('stringPtr','author');
pfileauthlen=libpointer('uint32Ptr',0);
%Get the length of the 'DDC_FILE_AUTHOR' string property
err=calllib('nilibddc','DDC_GetFileStringPropertyLength',pfile.Value,DDC_FILE_AUTHOR,pfileauthlen);
if err==0 %Only proceed if File Author is found
    %Initialize a string of the length of the file author
    pfileauth=libpointer('stringPtr',blanks(pfileauthlen.Value));
    calllib('nilibddc','DDC_GetFileProperty',pfile.Value,DDC_FILE_AUTHOR,pfileauth,pfileauthlen.Value+1);
    disp(['File Author: ' pfileauth.Value]);
end

%Read and Display File Timestamp
DDC_FILE_DATETIME=libpointer('stringPtr','datetime');
pyear=libpointer('uint32Ptr',0);
pmonth=libpointer('uint32Ptr',0);
pday=libpointer('uint32Ptr',0);
phour=libpointer('uint32Ptr',0);
pminute=libpointer('uint32Ptr',0);
psecond=libpointer('uint32Ptr',0);
pmsecond=libpointer('doublePtr',0);
pwkday=libpointer('uint32Ptr',0);
err=calllib('nilibddc','DDC_GetFilePropertyTimestampComponents',pfile.Value,DDC_FILE_DATETIME,pyear,pmonth,pday,phour,pminute,psecond,pmsecond, ↙
pwkday);
if err==0 %Only proceed if File Timestamp is found
    disp(['File Timestamp: ' num2str(pmonth.Value) '/' num2str(pday.Value) '/' num2str(pyear.Value) ', ' num2str(phour.Value) ':' num2str(pminute.Value) ':' ↙
num2str(psecond.Value) ':' num2str(pmsecond.Value)]);
end


%Get Channel Groups
DDC_CHANNELGROUP_NAME=libpointer('stringPtr','name');
DDC_CHANNELGROUP_DESCRIPTION=libpointer('stringPtr','description');
DDC_CHANNEL_NAME=libpointer('stringPtr','name');
%Get the number of Channel Groups
pnumgrps=libpointer('uint32Ptr',0);
calllib('nilibddc','DDC_GetNumChannelGroups',pfile.Value,pnumgrps);
%Get Channel Groups only if the number of Channel Groups is greater than
%zero
if pnumgrps.Value>0
    pgrps=libpointer('int32Ptr',zeros(1,pnumgrps.Value));
    calllib('nilibddc','DDC_GetChannelGroups',pfile.Value,pgrps,pnumgrps.Value);
end
for i=1:pnumgrps.Value %For each Channel Group
    %Get Channel Group Name
    pgrpnamelen=libpointer('uint32Ptr',0);
    err=calllib('nilibddc','DDC_GetChannelGroupStringPropertyLength',pgrps.Value(i),DDC_CHANNELGROUP_NAME,pgrpnamelen);
    if err==0 %Only proceed if Channel Group Name is found
        pgrpname=libpointer('stringPtr',blanks(pgrpnamelen.Value));
        calllib('nilibddc','DDC_GetChannelGroupProperty',pgrps.Value(i),DDC_CHANNELGROUP_NAME,pgrpname,pgrpnamelen.Value+1);
    else
        pgrpname=libpointer('stringPtr','');
    end

    %Get Channel Group Description
    pgrpdesclen=libpointer('uint32Ptr',0);
    err=calllib('nilibddc','DDC_GetChannelGroupStringPropertyLength',pgrps.Value(i),DDC_CHANNELGROUP_DESCRIPTION,pgrpdesclen);
    if err==0 %Only proceed if Channel Group Description is found
        pgrpdesc=libpointer('stringPtr',blanks(pgrpdesclen.Value));
        calllib('nilibddc','DDC_GetChannelGroupProperty',pgrps.Value(i),DDC_CHANNELGROUP_DESCRIPTION,pgrpdesc,pgrpdesclen.Value+1);
    end

    figure('Name',pgrpname.Value);
    hold on;

    %Get Channels
    pnumchans=libpointer('uint32Ptr',0);
    %Get the number of Channels in this Channel Group
    calllib('nilibddc','DDC_GetNumChannels',pgrps.Value(i),pnumchans);
    %Get Channels only if the number of Channels is greater than zero
    if pnumchans.Value>0
        pchans=libpointer('int32Ptr',zeros(1,pnumchans.Value));
        calllib('nilibddc','DDC_GetChannels',pgrps.Value(i),pchans,pnumchans.Value);
    end
```

```
    channames=cell(1,pnumchans.Value);

    for j=1:pnumchans.Value %For each Channel in group
        %Get Channel Name
        pchannamelen=libpointer('uint32Ptr',0);
        err=calllib('nilibddc','DDC_GetChannelStringPropertyLength',pchans.Value(j),DDC_CHANNEL_NAME,pchannamelen);
        if err==0 %Only proceed if Channel Name is found
            pchanname=libpointer('stringPtr',blanks(pchannamelen.Value));
            calllib('nilibddc','DDC_GetChannelProperty',pchans.Value(j),DDC_CHANNEL_NAME,pchanname,pchannamelen.Value+1);
            channames{j}=pchanname.Value;
        else
            channames{j}='';
        end

        %Get Channel Data Type
        ptype=libpointer('voidPtr',uint8(0));
        calllib('nilibddc','DDC_GetDataType',pchans.Value(j),ptype);

        %Get Channel Value if Data Type is 'Double'(10)
        if ptype.Value==10
            pnumvals=libpointer('uint64Ptr',0);
            calllib('nilibddc','DDC_GetNumDataValues',pchans.Value(j),pnumvals);
            pvals=libpointer('doublePtr',zeros(1,pnumvals.Value));
            calllib('nilibddc','DDC_GetDataValues',pchans.Value(j),0,pnumvals.Value,pvals);
            chanvals(:,j)=(pvals.Value)'; %#ok<AGROW>
        end

    end

    %Plot Data from channels in this group
    plot(chanvals); %clear chanvals;

    legend(channames);
end

%Close TDM or TDMS file
calllib('nilibddc','DDC_CloseFile',pfile.Value);

%Unload nilibddc.dll
unloadlibrary('nilibddc');
%-------------------End of Read TDMS file from National Instruments

%-------------------Start Section added by Stephen Orlando
chan_nums=str2num(char(channames(2:size(channames,2))));
pre_s=vertcat(chan_nums',chanvals(:,2:size(chanvals,2)));  %Add mic numbers to first row
[first_row, mic_order] = sort(pre_s(1,:));
sorted_s=pre_s(:,mic_order);          %Sort columns into increasing mic number
clear pre_s
s=sorted_s(2:size(sorted_s,1),:);  %Remove mic numbers from first row
clear s_sorted

mic_coord_data=csvread('MicDataBoard2.csv');  %Get array data [mic number, x, y, z, sensitivity]
mic_sensitivity=mic_coord_data(:,5);  %Read mic sensitivities in V/Pa
for i= 1:size(mic_sensitivity)
    s(:,i)=s(:,i)/mic_sensitivity(i);%Divide by sensitivity to convert volts to Pascals
end
s=s/2; %Divide by 2 to account for pressure doubling since mics are on a hard surface
%-------------------End Section added by Stephen Orlando
%-------------------End ReadSignals.m
```